THE UNIVERSITY OF CHICAGO


C-TYPE INACTIVATION AND VOLTAGE SENSOR TO INTRACELLULAR GATE COUPLING

IN EUKARYOTIC POTASSIUM CHANNELS


A DISSERTATION SUBMITTED TO

THE FACULTY OF THE DIVISION OF THE PHYSICAL SCIENCES

AND

THE FACULTY OF THE DIVISION OF THE BIOLOGICAL SCIENCES

AND THE PRITZKER SCHOOL OF MEDICINE

IN CANDIDACY FOR THE DEGREE OF

DOCTOR OF PHILOSOPHY


GRADUATE PROGRAM IN BIOPHYSICAL SCIENCES


BY

YOUNG HOON KOH


CHICAGO, ILLINOIS

AUGUST 2022

**Table of Contents**

LIST OF FIGURES

LIST OF TABLES

# ABBREVIATIONS

2D- 2-dimensional (and so on, 3D, etc)

BMG – buffered minimal glycerol media

BMM – buffered minimal methanol media

C-type inactivation – inactivation occurring at the C-terminal end of the channel

cDNA – complementary DNA

CHARMM - Chemistry at Harvard Macromolecular Mechanics

CHS – cholesterol hemisuccinate

$Cl^-$ - chloride ion

$CO_2$ – carbon dioxide

COVG – cut-open oocyte vaseline-gap

Cryo-EM – cryogenic electron microscopy

crYOLO – cryo-EM particle picking software

DDM – n-dodecyl- β-D-maltoside

DNA – deoxyribonucleic acid

DTT – dithiothreitol

E3D1 – membrane scaffold belt protein for nanodisc formation

EGTA - ethylene glycol-bis(β-aminoethyl ether

FL – full-length

FSC – Fourier shell coefficient

FSEC – fluorescence size exclusion chromatography

GV – conductance vs voltage

$H_2O$ – water

HEPES - 4-(2-hydroxyethyl)-1-piperazineethanesulfonic acid

hERG – human Ether-a-go-go-Related (ion channel)

ILT – isoleucine, leucine, threonine triple mutant construct

IV – current vs voltage

$K^+$ - potassium ion

KCNE1 – potassium voltage-gated channel subfamily E member 1

KCNQ1 – potassium voltage-gated channel subfamily Q member 1

KcsA – $K^+$ channel from *Streptomyces lividans*

Kv – voltage-gated $K^+$ channel

Kv1.2 – potassium voltage-gated channel subfamily A member 2

Kv1.2-2.1 – Kv1.2 with S3b-S4 domain of Kv2.1 swapped in

KvChim – Kv1.2-2.1

MD – Molecular Dynamics

MDFF – Molecular Dynamics Flexible Fitting

MES - 2-(*N*-morpholino)ethanesulfonic acid

mRNA – messenger RNA

MSP – membrane scaffold protein

N-type inactivation – inactivation occurring at the N-terminal end of the channel

$N_2$ – nitrogen

$Na^+$ - sodium ion

NAMD – nanoscale molecular dynamics

ND – nanodisc

$NH_4^+$ - ammonium

NMDG - N-methyl-D-glucamine

O/N – overnight

$O_2$ – oxygen

OD – optical density

$P_0$ – open probability (normalized 0 to 1)

PDB – protein data bank

pH – potential of hydrogen

PM – planetary mill

PM – plasma membrane

PME – particle mesh Ewald

PMSF – phenylmethanesulfonylfluoride

POPC – palmitoyl-oleoyl-phosphatidylcholine

POPE - palmitoyl-oleoyl-phosphatidylethanolamine

POPG – palmitoyl-oleoyl-phosphatidylglycerol

RMS – Root Mean Square

RMSD – Root Mean Square Deviation

RNA – ribonucleic acid

RT – room temperature

$S_1$ – first binding site in the selectivity filter (and so on, $S_2$, etc)

S1 – first transmembrane segment (and so on, S2, etc.)

SDS-PAGE – Sodium Dodecyl Lauryl Sulfate Polyacrylamide Gel Electrophoresis

SEC – Size Exclusion Chromatography

*Shaker*-IR – *Shaker* protein with N-terminal inactivating ball-and-chain removed

ShB – *Shaker* B potassium channel

SLAC – Stanford Linear Accelerator Center

T1 – tetramerization domain 1

TCEP - Tris(2-carboxyethyl) phosphine

TEA – tetraethylammonium

TM – transmembrane

TMD – transmembrane domain

VGIC – voltage-gated ion channel

VGKC – voltage-gated potassium channel

VMD – visual molecular dynamics

VSD – voltage-sensing domain

WT – wild-type

YPD – yeast extract – peptone – dextrose media

YPDS – yeast extract – peptone – dextrose- sorbitol media

β-ME - β-mercaptoethanol

ACKNOWLEDGEMENTS

This thesis is the culmination of six years of work in the Perozo and the Roux labs. I want to thank my advisors Prof. Eduardo Perozo and Prof. Benoît Roux for their insightful scientific discussions as well as their guidance as invaluable mentors. Most importantly, I appreciate their endless faith and patience for my scientific pursuit throughout my graduate career. Under their tutelage I have grown not only as a scientist but also as a human being and have learned many virtues such as resilience, patience, discipline, and humility. They provided an incredible work environment in which I was free to pursue discoveries and approach science purely for the sake of scientific progress. I hope some of their creativity, passion for science, and kind personalities have rubbed off on me a little bit. I also want to extend my gratitude to other members of my dissertation committee Francisco Bezanilla and Tobin Sosnick. Their insights, advice, questions, flexibility, and discussions have been critical to my thesis work.

I owe so much to my colleagues in the Perozo, Roux, and Bezanilla labs. From bouncing off serious scientific ideas to putting ice down each other's back, every memory with them is a valuable treasure that I will cherish as I move on to the next phase of life. I am truly very lucky to have surrounded myself with wonderful friends and co-workers who have displayed many admirable qualities that influenced my fundamental beliefs on what it means to be truly happy and fulfilled. From the Perozo lab, I admire Tian for her tireless diligence and resilience, Bharat for his expertise with our computational resources and cryo-EM, Gustavo for his great passion and insights on ion channels, Rong for his computational prowess and kind soul, Zhen for her happy disposition and cheerful laughs, Jane for her intellect, Zeeshan for deep philosophical thoughts and outlook on life, Emily for her amazing baking skills and her cheerful optimism. I will miss my bros Alejandro, Michael, Navid, Patrick, and Allen who were not only there to support me scientifically but also emotionally, especially when I was struggling the most. I thank them for providing me with a long-lasting relationship that I am certain will continue long after my

graduate years. I will also miss Ania, who was like a sister to me. And I want to thank Margaret, our beloved lab manager and our lab mom, and Rebecca, our cherished research support assistant. They are two of the strongest and most inspirational women and people that I know.

From the Roux lab, I want to thank Ahmed for teaching me the biochemistry and X-ray crystallography, especially when I first began my graduate school. He is an excellent mentor. I want to thank Jing for his discussions on C-type inactivation and expertise in computation. I also want to thank Lydia for being an excellent lab manager as well. Lastly, I want to thank Richa for taking the torch to continue the projects that are still ongoing after I leave. From the Bezanilla lab, Joao and Carlos have provided tremendous help with the functional results. I would also like to thank them as well as Bernardo, Yichen, Ben, and Fraol for being great friends as well. I also thank my collaborators James and Tera from the EM facility.

Outside of the work, I would like to thank the biophysics program for their love and support. I especially would like to thank Michele Wittels for her help in terms of managing important deadlines and all of the important documents. Every time I interact with her, I can truly feel that she really cares about each of the students and that she is passionate about her job. For me, she is the embodiment of Kant's teachings to treat people as ends and not as means.

Zooming out from the contacts I have made at the University of Chicago, I thank my mom and dad for who I am today. They instilled in me the creativity, diligence, perseverance, strong sense of what is right and wrong, and most importantly, empathy. I dedicate this thesis to them, who have dedicated themselves tirelessly for me and my sister all throughout our lives.

# Chapter 1: Introduction

For a cell to function properly as the basic unit of life, it requires a robust structure that helps maintain its integrity to differentiate itself from the "rest of the world" without being completely isolated. Nature's solution to this problem is the plasma membrane (PM), where bilayers of phospholipids with associated proteins separate the interior of the cell from its environment and create an electrochemical gradient between the intracellular and extracellular environments [6]. This membrane is semipermeable, allowing necessary communication between the interior and the exterior of the cell so that it can receive crucial resources and energy from the outside to perform its myriad of functions. Because of the hydrophobic nature of the phospholipids, critical hydrophobic molecules such as $O_2$, $CO_2$, or $N_2$ and small, uncharged polar molecules such as $H_2O$ or glycerol can pass through in and out of the cell by passive diffusion. The membrane, however, presents an energy barrier that prevents the passage of large uncharged polar molecules such as sugar molecules as well as charged ions such as $K^+$ or $Na^+$ (**Figure 1.1**). To transport these crucial components across the membrane, the cells need specialized proteins embedded in the PM, such as ion channels, transporters, and receptors [5]. The cells utilize these membrane proteins as machinery to exploit the electrochemical gradient across the cell membrane, which is used for cell signaling to exchange information from each other and their environment [9].

Of all types of cell signaling, the transmembrane potential is by far the most convenient, efficient, and fastest mode of signaling as it utilizes the already-existing ionic gradient across the PM [10]. By virtue of the long-range nature of the Coulombic interactions, the electric potential generated by the movements of small ions across the PM ensures the synchronization of specific molecular processes taking place at distances far larger than typical short-range intermolecular forces. The transmembrane potential constitutes a unified communication system for physiological information throughout the cell. For this, cells use

channels to selectively transport charged ions down their electrochemical gradient. Because

of this important role, ion channels are ubiquitous across all forms of life, from the simplest

unicellular bacteria all the way up to humans. Ion channels can open and close in response

to specific stimuli from their environment to allow the passage of specific or nonspecific ions

down their electrochemical gradient. In voltage-gated ion channels (VGIC), for example, the



| Hydrophobic Molecules | $O_2$ $CO_2$ $N_2$ Benzene |
| Small Uncharged Polar Molecules | $H_2O$ Urea Glycerol |
| Large Uncharged Polar Molecules | Glucose Sucrose |
| Ions | $K^+$, $Na^+$, $H^+$, $Ca^{2+}$, $Cl^-$, $Mg^{2+}$, etc |

**Cell Exterior**      **Plasma Membrane**      **Cell Interior**
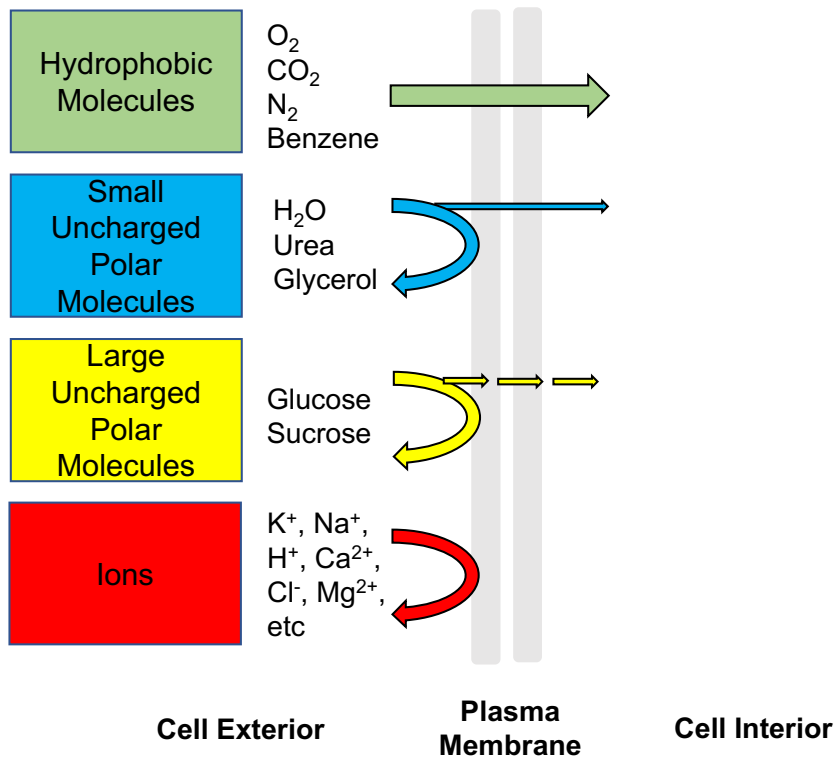
**Figure 1.1:** What can readily pass through the plasma membrane? Adapted from [5]. Hydrophobic and small, uncharged polar molecules pass through the plasma membrane more readily through passive diffusion without any aid. Large uncharged polar molecules and charged ions cannot travel through the hydrophobic membrane on their own. They require additional features called membrane proteins to facilitate the movement across the membrane to the interior of the cell.

ionic conductance of the ions itself is regulated by the membrane potential. In other words,

the opening of the channels allows the passage of ions that affects the membrane potential,

which in turn also affects the rate of opening of other channels. This interaction between

voltage-gating and ion conduction built into the system gives rise to the action potential [11,

12]. Different VGICs conducting different specific ions and opening and closing at different voltages come together to generate cellular excitability and complex electrical behaviors in various organisms, such as the cardiac/neural action potentials that underlie pace-making [13, 14].

One cannot discuss VGIC, action potentials, and intercellular electric communications in general without mentioning the groundbreaking work of Hodgkin and Huxley. Using the squid giant axon as the model system, they documented the first intracellular recording of action potential [15]. Using their voltage and current clamp techniques, Hodgkin and Huxley used their empirical data to formulate a mathematical model for the voltage-dependent ion conductance that result in critical phenotype known as action potential [11, 16].

The action potential is like a well-choreographed dance amongst various VGIC. Before the action potential begins, the membrane potential is resting at around -70mV, and all voltage-gated $K^+$ and $Na^+$ channels are closed. The action potential is triggered by external stimulus, which begins to depolarize the membrane potential slightly. If this stimulus does not allow the membrane potential to reach approximately -55mV, then the initiation for the action potential has failed and the membrane stays at its resting potential. If the initial depolarization does reach around -55mV, however, $Na^+$ channels begin to open, allowing $Na^+$ ions to flow down their electrochemical gradient into the cell, further increasing membrane depolarization. At some point, $K^+$ channels begin to open. However, as the rate of $K^+$ channel opening is about 6 times slower than that of $Na^+$ channels [17], the membrane depolarization continues to increase to well over 0 mV. Once the membrane potential reaches about 30 mV, $Na^+$ channels begin to quickly inactivate, preventing any more influx of $Na^+$ into the cell. By this point, $K^+$ channels are fully conducting, conducting $K^+$ ions out of the cell resulting in a rapid repolarization of the membrane toward its resting potential. Inactivation of some $K^+$ channels during the prolonged depolarization can delay the return to the resting potential. Only once the potential reaches around -50mV do $K^+$ channels begin to

close. When the membrane potential reaches -70mV at resting potential, the cell is ready to

initiate a new action potential (**Figure 1.2**).
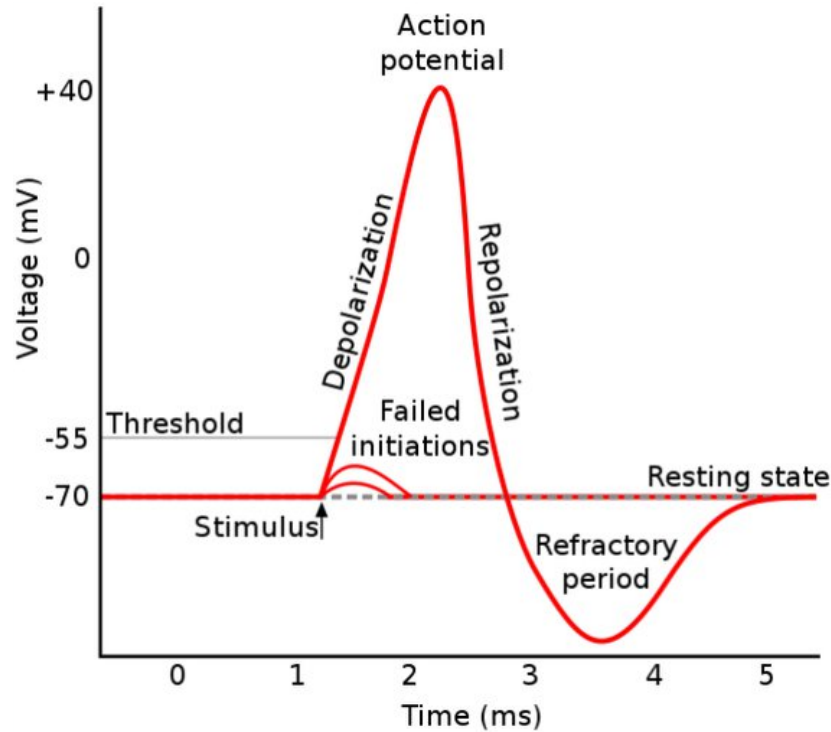


**Figure 1.2:** Schematic of an action potential. Adapted from [4].
At -55mV sodium channels open first, further depolarizing the
membrane potential. Once K⁺ channels open and are
conductive, Na⁺ channels become inactivated. Then K⁺
channels take over, pumping K⁺ ions out of the cell and thus
repolarizing the membrane potential. This continues until K⁺
channels close, returning the membrane potential back to its
resting potential at around -70mV. This entire process occurs in
a few milliseconds.

Before we delve into the subtle functions of these VGICs, it is important to establish

their general architectures. Here we focus on the voltage-gated K⁺ (Kv) channels, as they are

the major players in this thesis. Structurally, Kv channels are tetrameric proteins with six

transmembrane (TM) segments consisting of four voltage-sensing domains (VSDs)

surrounding a central pore domain [18] (**Figure 1.3**). Generally, both the N- and C- termini

are on the intracellular side of the membrane (**Figure 1.3c**). Most Kv channels such as the

*Shaker* or Kv1.2 are homotetramers, but there are also some heterotetrametric channels

including KCNQ1/KCNE1 [19]. Each VSD is formed by four TM helical segments (S1-S4), where S4 contains a string of crucial gating charged arginines and lysines arranged in a highly conserved RxxRxxR motif. Here, the x are the hydrophobic residues and some arginines are sometimes replaced by lysines [20]. The segments S1-S3 of the VSD provide a hydrophobic gasket - essentially an ion-impermeable high-energy barrier through which the gating charges from S4 cross upon a change in the transmembrane electric field. The pore domain of Kv channels is formed by the S5 segment, the p-helix, and the S6 segment of the four subunits coming together in a four-fold symmetric structure (**Figure 1.3c**). The pore domain is responsible for creating the energetically favorable path for $K^+$ ion conduction between the extracellular and intracellular sides of the membrane in response to the conformational changes in the VSD [21]. From structural and functional studies, we know that the pore domain consists of two major gates: the intracellular "activation" gate toward the
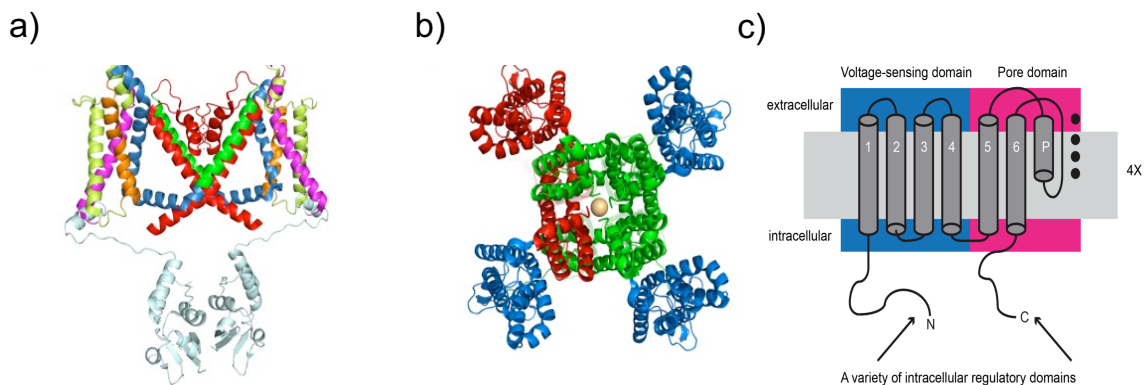


**Figure 1.3:** Voltage-Gated Potassium Channel. Adapted from [7]. a) Side view and b) top view of a Kv channel structure. Voltage sensing domain is located at the periphery, while the pore domain is located at the internal part of the protein. The selectivity filter where the ion conduction occurs is at the axis of symmetry from the top view. c) Kv channels are homotetramers with each monomer composed of the S1-S4 segments that comprise the voltage sensing domain (VSD) and the S5-pore helix-S6 segments that comprise the pore domain (PD).

N-terminus formed from constriction of the S5 and S6 helices [22], and an extracellular "inactivation" gate toward the C-terminus that is modulated by conformational changes in the selectivity filter [23, 24]. We will delve deeper on this topic when we discuss inactivation.

For depolarization-activated voltage channels, which most VGIC including *Shaker* or Kv1.2 are, the depolarizing potential drives the gating charges in S4 across the hydrophobic gasket. This movement creates a capacitive current also known as gating current, which in size is ~100 times smaller in size than ionic current [25]. The conformational changes in the VSD are transmitted through the S4-S5 linker to the S5 segment of the pore domain, causing the intracellular activation gate to open and close.

Unlike Kv channels in eukaryotic cells, prokaryotic counterparts are relatively simpler in their architecture. However, the prokaryotic channels such as the proton-gated $K^+$ channel KcsA from *Streptomyces lividans* still retain most of the pore domain features that Kv channels have, with 38% sequence similarity with the pore domain of *Shaker*. For this reason, KcsA has been an important prototypical model protein to study more complex Kv channels both functionally and structurally [26-28]. KcsA is a homotetramer with two TM alpha helical segments called TM1 and TM2 (**Figure 1.4**). Between these two TM helices is a re-entrant loop, in the simple topology of TM1- "pore helix"- selectivity filter-TM2. The intracellular activation gate is formed by the inner bundle of TM1 and TM2 that creates a physical barrier to ion permeation [29]. The pH sensing residues are located near the intracellular end of TM1 and TM2. As in Kv channels, the selectivity filter of KcsA has the signature sequence TVGYG that is conserved across most $K^+$ channels [30, 31] (**Figure 1.4**). This selectivity filter creates a four-fold symmetric sequence of cages with backbone carbonyls facing toward the central axis of symmetry and four $K^+$ ion binding sites $S_1$ to $S_4$ that constitutes the permeation pathway. The filter coordinates $K^+$ via the backbone carbonyls by substituting for the dehydration energy of water, effectively creating an energetically favorable environment for the passage of $K^+$ ions in a single file along the four binding sites $S_1$ to $S_4$. One model of ion conduction is that the $K^+$ ions move in pairs, occupying alternatively the sites $S_1$-$S_3$ and $S_2$-$S_4$ [8, 21, 32]. In other words, KcsA is an important model system to study conduction and permeation in other more complex $K^+$

channels, as it retains all of the pore domain features of more complex Kv channels.

Therefore, when the structure of KcsA was discovered in 1998 by the Mackinnon lab [21], the

field of ion channel underwent a structural revolution. Since then, KcsA has been used as a

prototypical model channel to study various states of ion occupancy, effects of various

pharmacological channel blockers, and physiologically interesting mutations to infer more
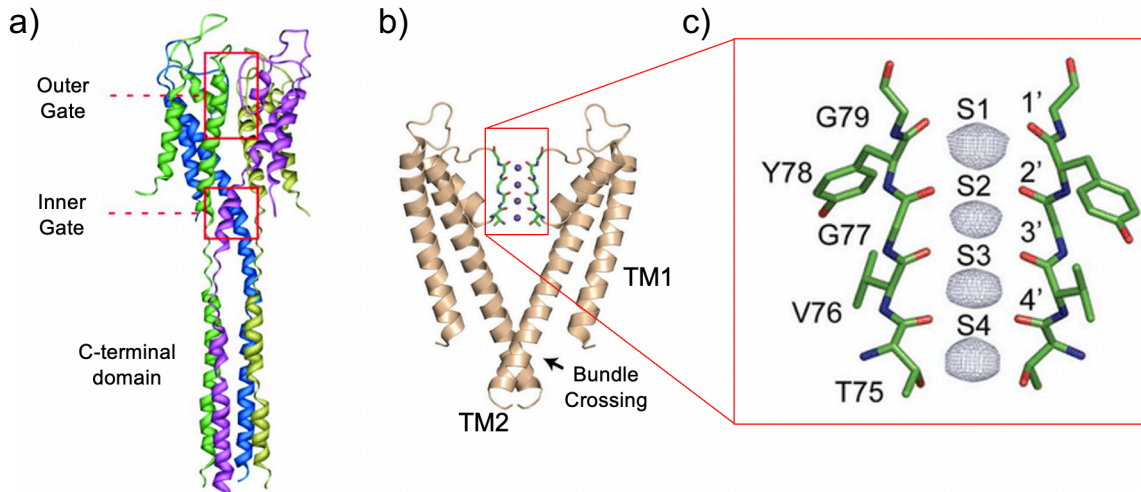


**Figure 1.4:** The architecture of KcsA from *S. lividans* exhibits the quintessential structures of potassium channels. Adapted from [2, 3]. Structure of the wild-type KcsA channel ((a) PDB: 3EFF and (b,c) PDB: 1K4C). a) KcsA is a pH gated, voltage-dependent potassium channel from the prokaryotic *S. lividans*. It is a homotetramer composed of two TM alpha helical segments TM1 and TM2, which has the pH sensing residues. TM2 extends to the C-terminus to form the inner bundle gate. b) Between TM1 and TM2 is the pore helix, which houses the selectivity filter where the ion conduction occurs. c) The selectivity is built from the TVGYG residues that are conserved across most potassium channels. These residues form four binding sites for the potassium ion, called $S_1$ to $S_4$ binding sites, to allow for a smooth conduction pathway.

about the structural nature of $K^+$ channels as a whole. Perhaps one of the most important

applications of KcsA in structural biology, however, is in the study of intracellular and

extracellular gate conformations and the determination of the structure of C-type inactivation

[8, 33, 34].

The opening and closing of the VGICs refer to the conformations of their intracellular

gate in response to the external stimulus, which is the membrane depolarization. For

depolarization-activated voltage channels, which most VGICs are, the depolarizing

membrane potential electrically moves the charged voltage sensing domains in the up state

7

(state in which the gating charges move to the extracellular side), causing the intracellular activation gate to become wider to allow ion conduction through the pore. Once depolarizing potential persists, however, many of these channels undergo a process known as inactivation to prevent ion conduction even as the intracellular gate remains open. Inactivation is an auto-regulatory mechanism developed by these proteins so that they can respond to their environment and govern the occurrence and shape of action potentials in excitable tissues in addition to dynamics of closing and opening of the intracellular gate [35].

Recent advances in the molecular biology and functional analysis of $K^+$ channels have elucidated two distinct classes of inactivation: N-type and C-type. N-type inactivation involves the physical occlusion of the intracellular mouth of the pore with a binding of a short peptide at the N-terminus of the protein [1]. As we can see in **Figure 1.5a**, the "tethered ball" blocks the opened intracellular gate prevent conduction. This was first observed in the voltage-gated *Shaker* channel from *Drosophila melanogaster* (fruit fly) and was also termed "fast inactivation" because this inactivation occurs at the millisecond timescale [36, 37]. As for the location of the inactivation, Yellen lab in 1991 conducted a competitive binding assay using tetraethylammonium (TEA) and discovered that the internal TEA competes with the "tethered ball" to inhibit N-type inactivation [38].

In contrast to this "tethered ball" mechanism of N-type inactivation, C-type inactivation involves subtle conformational change in the selectivity filter, which is in the C-terminus, to prevent ion conduction either physically, energetically, or both (**Figure 1.5b**). The location of C-type inactivation was also determined by TEA competitive binding assay; external rather than internal TEA prevents C-type inactivation in *Shaker* [38]. Although C-type inactivation is as fast as N-type in some $K^+$ channels such as hERG [39], it is often slower developing and recovering in kinetics. For this, it has also been known as "slow inactivation" [1]. C-type inactivation was first described in the squid giant axon and was subsequently functionally characterized extensively in *Shaker*, where the removal of the N-

type inactivating peptide still resulted in slow inactivation of the channel functionally in continuously depolarizing potentials [37, 40]. Unlike the mechanism of N-type inactivation, however, the mechanism of the subtle changes in the selectivity filter conformations in such complex $K^+$ channels is still unclear and heatedly debated [41].

a)                                                          b)
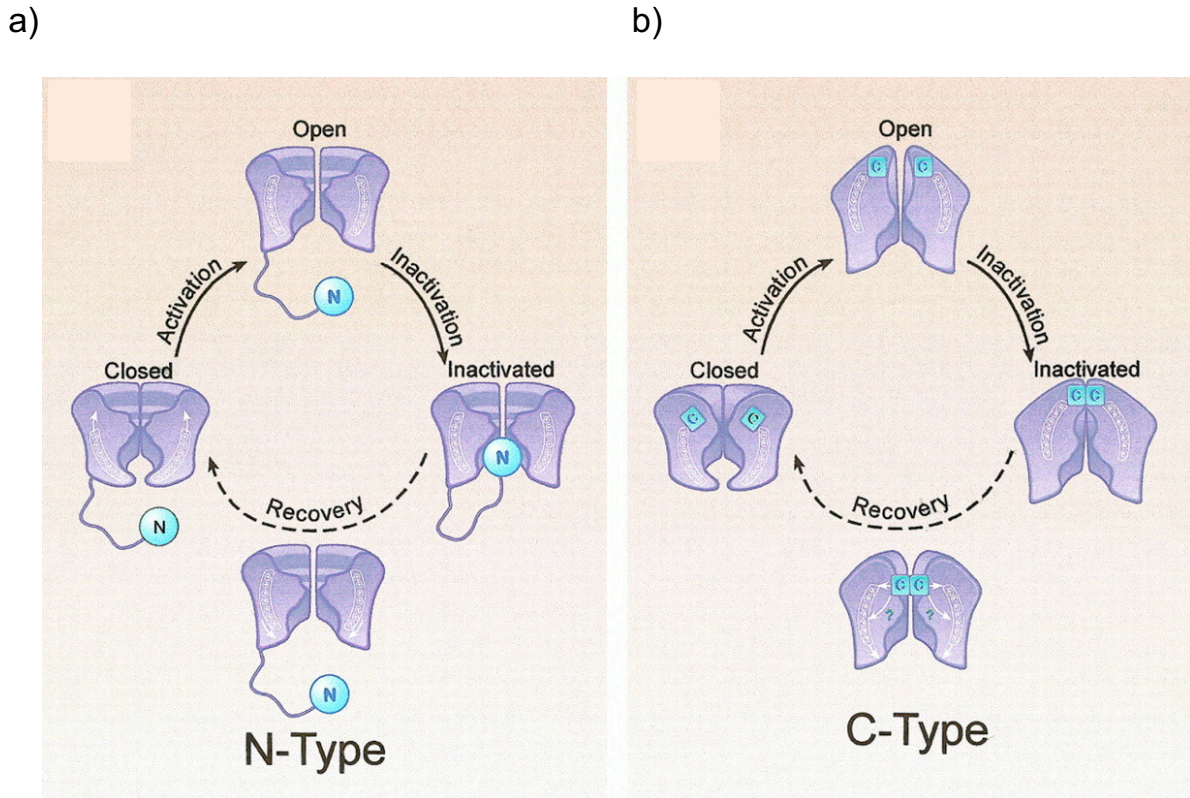


**Figure 1.5:** Two representative types of inactivation in $K^+$ channels: N-type and C-type. Adapted from [1]. a) N-type or fast inactivation prevents conduction via a physical blockage of the intracellular gate while the channel is open. The blockage occurs by the N-terminal "ball" residues tethered to a "chain" that swings into the intracellular gate. Only once this N-terminal "ball" is removed from the gate can the channel properly close and wait for activation to be opened again. b) C-type or slow inactivation prevents conduction via subtle conformational modulations in the selectivity filter, which is located at the C-terminal end of the channel. When the selectivity filter is in its inactivated conformation, the potassium ions cannot properly desolvate from the hydration shell and move through the selectivity filter in a single file. This inactivated selectivity filter is known to recover back to the conductive conformation once the intracellular gate is closed.

Fortunately, the mechanism of C-type inactivation is quite well established in the prokaryotic proton-gated $K^+$ channel KcsA. Ever since its X-ray crystal structure was first discovered in 1998 [21], KcsA has been the model protein to understand the structural basis of many of its functional phenotypes at various conditions. One such phenotype was the C-

type inactivation. In 2001, the Mackinnon lab depleted the $K^+$ ions in the crystal condition of

KcsA to reduce ion occupancy inside the selectivity filter. This hypothetically would drive the

selectivity filter energetically to adopt a nonconducting and C-type inactivated conformation.

Indeed, their crystal structure of KcsA at 2.0 Å resolution with 2mM low $K^+$ reveals precisely
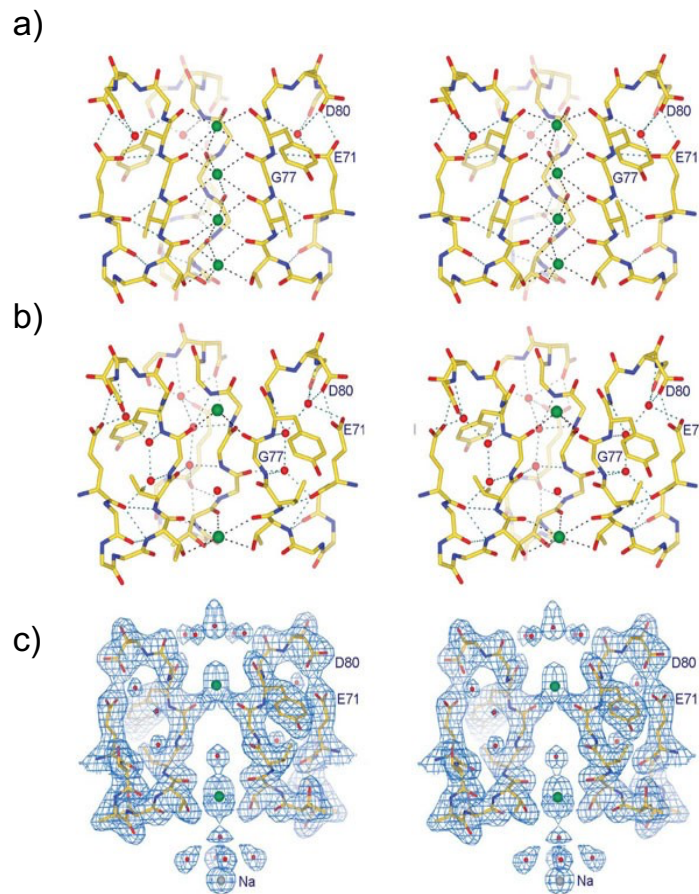


**Figure 1.6:** C-type inactivation in KcsA is driven by low $K^+$. Adapted from [8]. a) High $K^+$ (200 mM KCl) structure of KcsA with $K^+$ ions in S1-S4 binding sites. Each ion is located at the center of eight oxygen atoms from the backbone of the selectivity filter residues. b) Low $K^+$ (3 mM KCl) structure of KcsA with $K^+$ ions in S1 and S4 binding sites only. Each ion is located at the center of eight oxygen atoms from the backbone of the selectivity filter residues. c) A 2.0 Å resolution electron density map ($2F_o - F_c$, 1.5σ) validating the low $K^+$ structure.

what they had predicted. In **Figure 1.6**, directly from their paper, the selectivity filter of KcsA

at high (150mM) (**Figure 1.6a**) and low (2mM) $K^+$ (**Figure 1.6b**) are shown for comparison.

Here, they discovered that the ion occupancy at $S_2$ was completely removed and site at $S_3$

was partially removed in the low $K^+$ condition. Moreover, the carbonyl of the G77 residue in

the middle of the TVGYG selectivity filter pinches inwards, creating a nonconducting conformation of the filter. Lastly, unlike in high $K^+$ conditions, the low $K^+$ structure yielded the density of three water molecules behind the selectivity filter [8]. **Figure 1.6c** shows the high fidelity of these changes with a 2.0 Å resolution structure.

In 2010, Cuello et al. from the Perozo lab discovered of a series of structures of KcsA with various intracellular gate opening conformer states ranging from 12 Å in closed to 32 Å in fully opened KcsA ($C_\alpha$-$C_\alpha$ distances at T112). As we will discuss deeper in Chapter 2, they showed that as the intracellular gate becomes more open, the selectivity filter becomes more constricted and pinched [33]. What was surprising and interesting was that the constricted conformation with a fully opened gate was obtained with high $K^+$ crystallization conditions yet looked very similar to the nonconductive conformation from the low $K^+$ condition discovered by Zhou et al. in 2001. And with this, the pinched or the constricted filter conformation in KcsA was established as the C-type inactivated state.

As we will discuss further in Chapter 2, the pinched model hypothesis wasn't without its opposition [42]. However, the pinched model seems to be well established as the C-type inactivation for at least KcsA today [43]. Furthermore, we know the critical role of the hydrogen-bond network among D80, W67, and E71 in KcsA to stabilize the water molecules buried behind the selectivity filter, which in turn stabilizes the C-type inactivated pinched state [34, 44].

Even though C-type inactivation mechanism is established in KcsA, it is still unclear and heatedly debated in the voltage-gated $K^+$ channels such as *Shaker* or Kv1.2. This is not to imply that there hasn't been much effort on this front, however. In fact, C-type inactivation was first functionally characterized in *Shaker* [37, 40]. Then in 2005 and in 2007, the Mackinnon lab discovered the crystal structure of Kv1.2 and Kv1.2-Kv2.1 chimera, respectively, in lipid-detergent environment. They expected to see a C-type inactivated state at 0 mV from functional analysis [45], but they observed an open gate, conductive selectivity

filter conformation in their structures [46, 47]. As we will discuss in Chapter 4 in more detail, there have been other efforts by Matthies et al. and Pau et al. to capture the inactivated state via nanodisc reconstitution and C-type inactivating mutations, respectively, but the quest to obtain the C-type inactivated state have been still unclear [48, 49].

Then very recently, two papers revealed the cryo-EM and crystal structure of W434F in *Shaker* and W362F (W434F equivalent) in Kv1.2-2.1 chimera, respectively [50, 51]. W434F in *Shaker* had been shown functionally to have an increased rate of inactivation [52]. Because the channels with this mutation become so nonconductive, W434F in *Shaker* has historically been used to study the behavior of gating current in absence of ionic current [53]. Both W434F in *Shaker* and W362F in Kv1.2-2.1 chimera showed substantial changes in the sidechain and backbone conformations in the selectivity filter that energetically removed the binding site at $S_1$ and $S_2$, leaving the filter nonconductive. We will discuss the details of these structures in more detail in later Chapters, but there is no doubt that there is a lot of fervor in structural biology over C-type inactivation of voltage-gated $K^+$ channels currently.

Chapter 2 of this thesis will devote to capturing the C-type inactivated state in Kv1.2-2.1 chimera by immersing the channel in low $K^+$ conditions both functionally and structurally. We had three distinct advantages aiding us in pursuit of this project. Firstly, we already knew that Kv1.2 and Kv1.2-2.1 chimera both express in *Xenopus* oocytes well [45]. Secondly, the structure of Kv1.2-2.1, which is a chimera of Kv1.2 and Kv2.1, had already been solved via X-ray crystallography when we began this project [47]. Having the biochemical profiles for this profile would greatly aid us in facilitating the project. Secondly, the low $K^+$ condition has revealed the C-type inactivated state in KcsA already [8]. Therefore, it was naturally optimistic to see whether this low $K^+$ approach would yield a conformational change in the selectivity filter of Kv1.2-2.1 chimera, which shares high sequence and structural homology to KcsA, especially near the selectivity filter.

We initially approached the low K$^+$ in Kv1.2-2.1 chimera with X-ray crystallography but quickly realized that it was extremely difficult to form and maintain good crystal condition for the protein in the low K$^+$ environment. We switched the approach to cryo-EM, where we encountered some problems but were able to overcome and ultimately obtain the structures needed. Comparing the structures with the functional data, we discovered that the C-type inactivation in eukaryotic channels may be more subtle in the conformational changes than anticipated. The structures of high K$^+$ and low K$^+$ conditions revealed very similar densities. However, further analysis with MDFF revealed that there may be small structural changes associated with the underlying mechanism of inactivation.

Chapter 3 of this thesis will discuss the implication of the ILT mutant in Kv1.2-2.1 chimera, both functionally and structurally. The ILT mutation is well characterized in *Shaker*, but Kv1.2-2.1 chimera has some crucial differences in the voltage sensing domain (VSD) from *Shaker*, especially near the S4 segment where the mutation occurs. In this chapter, we present the functional characteristics of the ILT mutant in Kv1.2-2.1 chimera and compare them with those of the mutant in *Shaker*. Then we will present the structure of ILT mutant in Kv1.2-2.1 chimera. This is a novel mutant structure that has not been discovered yet. The structure exhibits some large changes in the VSD compared to the WT, especially in S2, S3, and S4 segments. We suggest that this structure may represent an intermediate conformation between the opened (already known) and the closed (not yet known or observed) gate conformation where the voltage sensor becomes decoupled from the pore domain.

The final chapter (Chapter 4) will summarize the results from the thesis and discuss my overall contribution. We will also discuss the implication of the thesis.

# References:

1.  Rasmusson, R.L., et al., *Inactivation of voltage-gated cardiac K+ channels.* Circulation Research, 1998. **82**(7): p. 739-750.
2.  Giudici, A.M., et al., *Accessibility of Cations to the Selectivity Filter of KcsA in the Inactivated State: An Equilibrium Binding Study.* Int J Mol Sci, 2019. **20**(3).
3.  Matulef, K., et al., *Individual Ion Binding Sites in the K(+) Channel Play Distinct Roles in C-type Inactivation and in Recovery from Inactivation.* Structure, 2016. **24**(5): p. 750-761.
4.  *Action Potential.* 2022; Available from: https://en.wikipedia.org/wiki/Action_potential.
5.  Alberts, B.J., A., Lewis, J. et al., *Molecular Biology of the Cell.* 4th Edition ed. 2002, New York: Garland Science.
6.  HM, C., *The Cell: A Molecular Approach. 2nd Edition.* 2000, Sunderland (MA): Sinauer Associates.
7.  Blunck, R. and Z. Batulan, *Mechanism of electromechanical coupling in voltage-gated potassium channels.* Front Pharmacol, 2012. **3**: p. 166.
8.  Zhou, Y., et al., *Chemistry of ion coordination and hydration revealed by a K+ channel-Fab complex at 2.0 A resolution.* Nature, 2001. **414**(6859): p. 43-8.
9.  Gouaux, E. and R. Mackinnon, *Principles of selective ion transport in channels and pumps.* Science, 2005. **310**(5753): p. 1461-5.
10. Hille, B., *Ionic Channels in Excitable Membranes - Current Problems and Biophysical Approaches.* Biophysical Journal, 1978. **22**(2): p. 283-294.
11. Hodgkin, A.L. and A.F. Huxley, *A Quantitative Description of Membrane Current and Its Application to Conduction and Excitation in Nerve.* Journal of Physiology-London, 1952. **117**(4): p. 500-544.
12. Catterall, W.A., *Structure and Function of Voltage-Gated Ion Channels.* Annual Review of Biochemistry, 1995. **64**: p. 493-531.
13. Brown, H.F., D. Difrancesco, and S.J. Noble, *How Does Adrenaline Accelerate the Heart.* Nature, 1979. **280**(5719): p. 235-236.
14. Santoro, B., et al., *Identification of a gene encoding a hyperpolarization-activated pacemaker channel of brain.* Cell, 1998. **93**(5): p. 717-729.
15. Hodgkin, A.L. and A.F. Huxley, *Action potentials recorded from inside a nerve fibre.* Nature, 1939. **144**: p. 710-711.
16. Hodgkin, A.L., A.F. Huxley, and B. Katz, *Measurement of Current-Voltage Relations in the Membrane of the Giant Axon of Loligo.* Journal of Physiology-London, 1952. **116**(4): p. 424-448.
17. Lacroix, J.J., et al., *Molecular bases for the asynchronous activation of sodium and potassium channels required for nerve impulse generation.* Neuron, 2013. **79**(4): p. 651-7.
18. Bezanilla, F., *How membrane proteins sense voltage.* Nat Rev Mol Cell Biol, 2008. **9**(4): p. 323-32.
19. Alesutan, I., et al., *Inhibition of the heterotetrameric K+ channel KCNQ1/KCNE1 by the AMP-activated protein kinase.* Mol Membr Biol, 2011. **28**(2): p. 79-89.
20. Swartz, K.J., *Sensing voltage across lipid membranes.* Nature, 2008. **456**(7224): p. 891-897.
21. Doyle, D.A., et al., *The structure of the potassium channel: molecular basis of K+ conduction and selectivity.* Science, 1998. **280**(5360): p. 69-77.
22. Webster, S.M., et al., *Intracellular gate opening in Shaker K+ channels defined by high-affinity metal bridges.* Nature, 2004. **428**(6985): p. 864-8.
23. Lopezbarneo, J., et al., *Effects of External Cations and Mutations in the Pore Region on C-Type Inactivation of Shaker Potassium Channels.* Receptors & Channels, 1993. **1**(1): p. 61-71.
24. Cordero-Morales, J.F., L.G. Cuello, and E. Perozo, *Voltage-dependent gating at the KcsA selectivity filter.* Nat Struct Mol Biol, 2006. **13**(4): p. 319-22.
25. Armstrong, C.M. and F. Bezanilla, *Currents related to movement of the gating particles of the sodium channels.* Nature, 1973. **242**(5398): p. 459-61.
26. Raja, M., *The potassium channel KcsA: a model protein in studying membrane protein oligomerization and stability of oligomeric assembly?* Arch Biochem Biophys, 2011. **510**(1): p. 1-10.

27.	Lipkind, G.M. and H.A. Fozzard, *KcsA crystal structure as framework for a molecular model of the Na(+) channel pore.* Biochemistry, 2000. **39**(28): p. 8161-70.

28.	LeMasurier, M., L. Heginbotham, and C. Miller, *KcsA: it's a potassium channel.* J Gen Physiol, 2001. **118**(3): p. 303-14.

29.	Thompson, A.N., et al., *Molecular mechanism of pH sensing in KcsA potassium channels.* Proc Natl Acad Sci U S A, 2008. **105**(19): p. 6900-5.

30.	Heginbotham, L., T. Abramson, and R. MacKinnon, *A functional connection between the pores of distantly related ion channels as revealed by mutant K+ channels.* Science, 1992. **258**(5085): p. 1152-5.

31.	Heginbotham, L., et al., *Mutations in the K+ channel signature sequence.* Biophys J, 1994. **66**(4): p. 1061-7.

32.	Berneche, S. and B. Roux, *Energetics of ion conduction through the K+ channel.* Nature, 2001. **414**(6859): p. 73-7.

33.	Cuello, L.G., et al., *Structural mechanism of C-type inactivation in K(+) channels.* Nature, 2010. **466**(7303): p. 203-8.

34.	Ostmeyer, J., et al., *Recovery from slow inactivation in K+ channels is controlled by water molecules.* Nature, 2013. **501**(7465): p. 121-4.

35.	Bahring, R. and M. Covarrubias, *Mechanisms of closed-state inactivation in voltage-gated ion channels.* J Physiol, 2011. **589**(Pt 3): p. 461-79.

36.	Hoshi, T., W.N. Zagotta, and R.W. Aldrich, *Biophysical and molecular mechanisms of Shaker potassium channel inactivation.* Science, 1990. **250**(4980): p. 533-8.

37.	Hoshi, T., W.N. Zagotta, and R.W. Aldrich, *Two types of inactivation in Shaker K+ channels: effects of alterations in the carboxy-terminal region.* Neuron, 1991. **7**(4): p. 547-56.

38.	Choi, K.L., R.W. Aldrich, and G. Yellen, *Tetraethylammonium blockade distinguishes two inactivation mechanisms in voltage-activated K+ channels.* Proc Natl Acad Sci U S A, 1991. **88**(12): p. 5092-5.

39.	Smith, P.L., T. Baukrowitz, and G. Yellen, *The inward rectification mechanism of the HERG cardiac potassium channel.* Nature, 1996. **379**(6568): p. 833-6.

40.	Kurata, H.T. and D. Fedida, *A structural interpretation of voltage-gated potassium channel inactivation.* Prog Biophys Mol Biol, 2006. **92**(2): p. 185-208.

41.	Hoshi, T. and C.M. Armstrong, *C-type inactivation of voltage-gated K+ channels: Pore constriction or dilation?* Journal of General Physiology, 2013. **141**(2): p. 151-160.

42.	Devaraneni, P.K., et al., *Semisynthetic K+ channels show that the constricted conformation of the selectivity filter is not the C-type inactivated state.* Proceedings of the National Academy of Sciences of the United States of America, 2013. **110**(39): p. 15698-15703.

43.	Xu, Y.Y. and A.E. McDermott, *Inactivation in the potassium channel KcsA.* Journal of Structural Biology-X, 2019. **3**.

44.	Cordero-Morales, J.F., et al., *A multipoint hydrogen-bond network underlying KcsA C-type inactivation.* Biophys J, 2011. **100**(10): p. 2387-93.

45.	Tao, X. and R. MacKinnon, *Functional analysis of Kv1.2 and paddle chimera Kv channels in planar lipid bilayers.* J Mol Biol, 2008. **382**(1): p. 24-33.

46.	Long, S.B., E.B. Campbell, and R. Mackinnon, *Crystal structure of a mammalian voltage-dependent Shaker family K+ channel.* Science, 2005. **309**(5736): p. 897-903.

47.	Long, S.B., et al., *Atomic structure of a voltage-dependent K+ channel in a lipid membrane-like environment.* Nature, 2007. **450**(7168): p. 376-82.

48.	Matthies, D., et al., *Single-particle cryo-EM structure of a voltage-activated potassium channel in lipid nanodiscs.* Elife, 2018. **7**.

49.	Pau, V., et al., *Crystal structure of an inactivated mutant mammalian voltage-gated K(+) channel.* Nat Struct Mol Biol, 2017. **24**(10): p. 857-865.

50.	Reddi, R., et al., *Structural basis for C-type inactivation in a Shaker family voltage-gated K+ channel.* Science Advances, 2022. **8**(16).

51.	Tan, X.F., et al., *Structure of the Shaker Kv channel and mechanism of slow C-type inactivation.* Sci Adv, 2022. **8**(11): p. eabm7814.

52.	Perozo, E., et al., *Gating Currents from a Nonconducting Mutant Reveal Open-Closed Conformations in Shaker K+ Channels.* Neuron, 1993. **11**(2): p. 353-358.

53.    Sigg, D., E. Stefani, and F. Bezanilla, *Gating Current Noise Produced by Elementary Transitions in Shaker Potassium Channels.* Science, 1994. **264**(5158): p. 578-582.

# Chapter 2: Cryo-EM structure and COVG functional analysis of Kv1.2-2.1 in low K⁺: towards the C-type inactivated conformation

## Abstract:

The structural basis for C-type inactivation in eukaryotic voltage-gated channels is still unknown and unclear at best. This is partially because the kinetics and depth of C-type inactivation in eukaryotic channels tend to be slower and shallower than in prokaryotic channels such as KcsA. In other words, each channel at 0 mV is more likely to be in a conductive conformation, and thus, trapping the protein in the inactivated state is quite difficult. Despite much effort from the field over the past decade or so, capturing this elusive C-type inactivated state structurally has been a great challenge.

To obtain the C-type inactivated state in Kv1.2-2.1, then, we decided to look back towards KcsA. In KcsA, the C-type inactivation is characterized by a constricted or pinched conformation in the selectivity filter, which prevents ion conduction. The Mackinnon lab captured this state by depleting the potassium ion from the protein and thus introducing a microenvironment near the selectivity filter that would favor the constricted inactivated state (1k4d) [3]. Applying the same idea to Kv1.2-2.1 to capture its inactivated state is a natural extension of this strategy. Not only is this an already proven way to induce conformational changes in the filter, but also it may be a more natural way to induce inactivation compared to introducing a highly disruptive mutation. After all, the C-type inactivated or non-conducting filter is by its very definition one that is depleted of K⁺ ions. Therefore, creating the environment around the channel to naturally induce its conformational change may give us the best chance to observe a conformational change that is associated with the native C-type inactivated state.

In this chapter, I will discuss the arduous challenges I faced trying to stabilize the Kv chimera protein in various low K⁺ environments with various counterions to K⁺. I will also discuss

how I solved this issue and ultimately obtained the structures and function of Kv1.2-2.1 in low K$^+$.


## Introduction:

As part of the Kv1 family, *Shaker* and Kv1.2 have served as model proteins to study the function and structural mechanism of C-type inactivation in voltage-gated K$^+$ channels for a few decades. C-type inactivation was first discovered in *Shaker*, when the removal of the ball-and-chain peptide segment at the N-terminus responsible for fast N-type inactivation revealed a slow inactivation process of the channel [2, 4] (**Figure 2.1**). Since then, the field naturally sought to elucidate the mechanism of slow or C-type inactivation with a structure of *Shaker*. Despite the arduous efforts, however, obtaining the crystal structure of *Shaker* has been a great challenge. Only in 2022 has the *Shaker* be resolved structurally with the advent of single particle cryo-EM technique [5]. Although we did not have the structure of *Shaker* for the past three decades, the structural quest to understand C-type inactivation in voltage-gated K$^+$ channels has been ongoing with Kv1.2, also known as *Shaker*-like channel subfamily A member 2. As the prominent VGKC in the central nervous system, Kv1.2 influences cellular excitability and action potential propagation [6-8] and is conserved in many animals from zebrafish and chicken to rats, chimps and humans. More importantly, it is the first eukaryotic voltage-gated channel with a reported atomic resolution structure.

The crystal structure of Kv1.2 was determined at 2.9 Å resolution in 2005 by the Mackinnon lab [9]. In 2007, they also determined the crystal structure of the Kv1.2-2.1 channel at 2.4 Å resolution [1]. Kv1.2-2.1 is a chimeric construct of Kv1.2 with a voltage-sensor paddle (helix-turn-helix comprising the S3b and S4 helices) from Kv2.1 (**Figure 2.2**). In both structures, lipid-detergent mixtures were used in the hanging drop conditions to provide a lipid bilayer-like environment for the channels as they form crystals. Both structures were resolved in the space

group P42$_1$2 and exhibited an open intracellular gate with a conductive selectivity filter (**Figure 2.3**). All in all, Kv1.2 and Kv1.2-2.1 exhibit virtually identical structural characteristics with respect to the pore domain and the VSD. They have also been shown to behave similarly functionally [1].
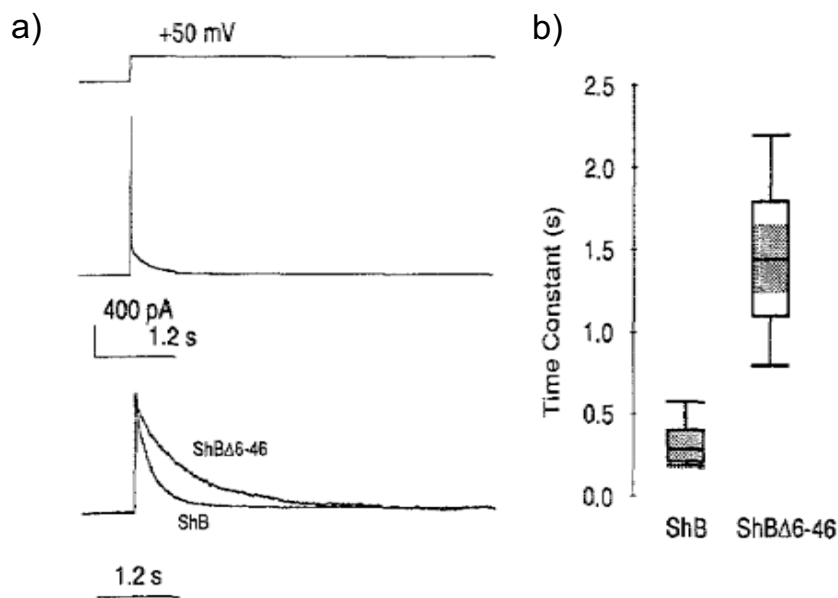


**Figure 2.1**: N-type and C-type Inactivation in Shaker B channel. Adapted from [2]. ShB is the WT *Shaker* channel with the N-type inactivating peptide while ShBΔ6-46 does not exhibit fast or N-type inactivation because it has the N-terminal residues removed. The inactivation dynamic of ShBΔ6-46 is solely determined by the slow or C-type inactivation. a) Macroscopic current of ShB and ShBΔ6-46 recorded from an inside-out patch clamp in response to 9.1 s pulse from -100mv to +50mV. The currents are scaled so that the peak amplitude of the slowly decaying component of the ShB current is approximately equal to the peak amplitude of the ShBΔ6-46 current. b) Box plots of the time constants of the decay of the ShB and ShBΔ6-46 currents at +50 mV. This shows the difference in time constants between the fast or N-type inactivation and the slow or C-type inactivation.

The presence of an open conducting state in the crystal structure of both Kv1.2 and Kv1.2-2.1 was somewhat of a surprise, because both channel constructs are known to slowly C-type inactivate under prolonged conditions at 0 mV when reconstituted into lipid membranes [10], which corresponds to the voltage conditions at which crystal structure was obtained. Matthies et al. suspected that the lipid-detergent conditions for the chimera from Long et al. might not have sufficiently provided a lipid-bilayer environment needed for the channel to be in a

stable C-type inactivated conformation. To this end, they turned to single particle cryo-EM because protein embedded in lipid nanodiscs cannot form crystals for X-ray crystallography. In 2018, they obtained a ~4 Å transmembrane resolution cryo-EM structure of Kv1.2-2.1 reconstituted into lipid nanodiscs. Unfortunately, they obtained a structure virtually identical to the Long et al. structure: the open conductive conformation [11].
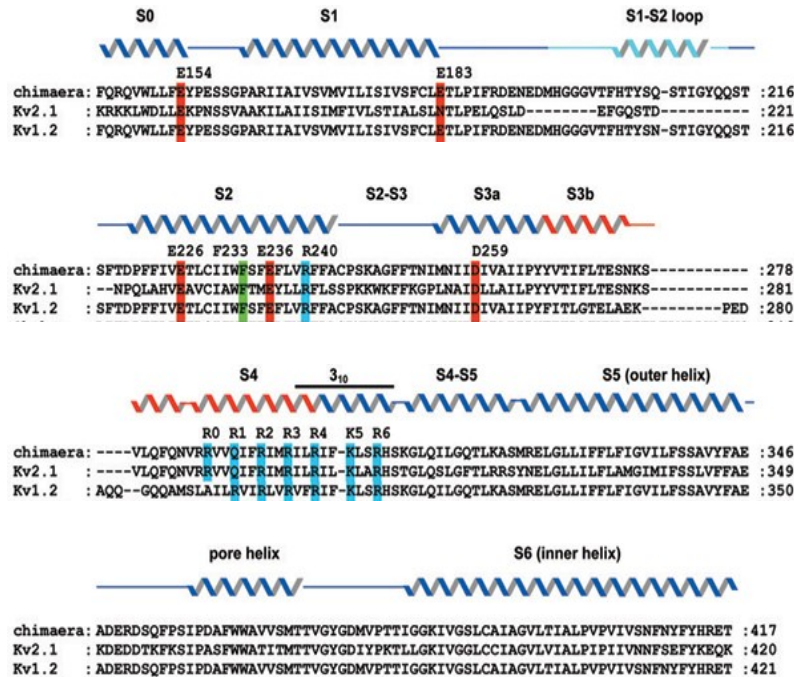


**Figure 2.2:** Sequence alignment displaying differences between Kv1.2 and Kv1.2-2.1 chimera. Adapted from [1]. Sequence alignment of Kv1.2, Kv2.1, and the Kv1.2-2.1 chimera shows that the chimera is Kv1.2 with the region S3b-S4 (shown in red) swapped with Kv2.1 parts.

In 2017, Pau et al. from the Lu lab sought to capture the structure of C-type inactivated Kv1.2-2.1 channel by introducing a mutation V406W in S6 to all four subunits while maintaining Long et al.'s approach to add lipid-detergent mixture in their crystal condition. V406W is the equivalent to V478W in *Shaker-IR* (N-type inactivation removed), which enhances C-type inactivation by functional analysis [12]. Their 3.3 Å resolution crystal structure of V406W Kv1.2-2.1 reveals two molecules in the asymmetric unit. One molecule is indistinguishable from the

WT Kv1.2-2.1 from Long et al., while the other molecule exhibits a slight modulation in the outer mouth of the selectivity filter that prevents ion occupancy at the $S_1$ binding site [12]. However, in the crystal structure of the V406W mutation, the large tryptophan side chains essentially block the permeation pathway at the intracellular entryway and thus question remains whether this conformation can really represent the inactivated structure. In fact, their selectivity filter without the $S_1$ binding site could energetically still be conductive if all other binding sites are intact. Despite the valiant effort, therefore, it is not convincing whether they have the C-type inactivated structure.

a)    b)    c)
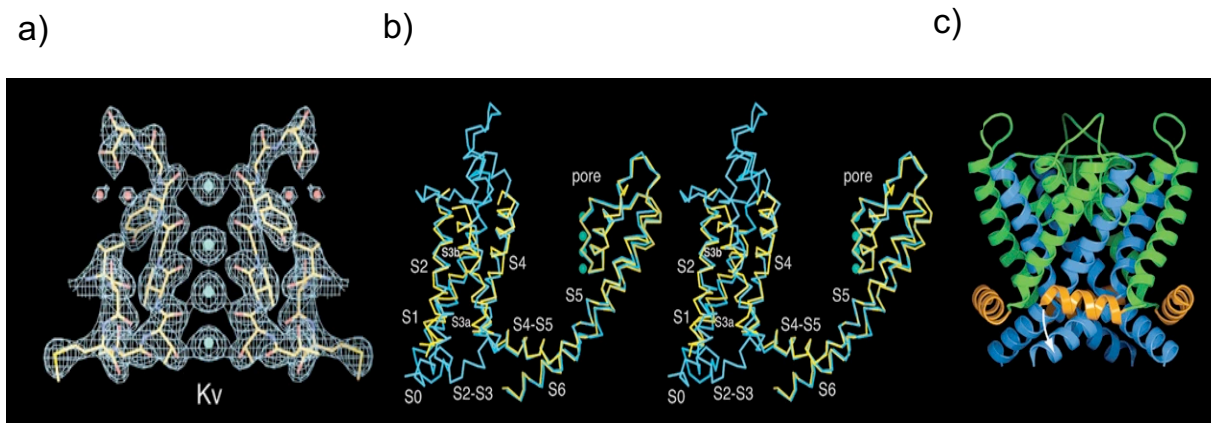


**Figure 2.3:** X-ray crystal structure of Kv1.2 and Kv1.2-2.1 both reveal an open intracellular gate with a conductive selectivity filter. Adapted from [1]. a) The selectivity filter of Kv1.2-2.1 and Kv1.2 are both conductive, with $K^+$ squarely occupying all four ion binding sites. Electron density (wire mesh, $2F_o–F_c$, $2.5\sigma$ contour), $K^+$ ions (green spheres) and water molecules (red spheres) are shown. b) Stereo structure of Kv1.2 and Kv1.2-2.1 transmembrane domain. The α-carbon trace of Kv1.2 (yellow) and Kv1.2-2.1 structures (cyan) are superimposed. c) Both structures exhibit an open intracellular gate with the bent S6 helix.

The quest to capture the C-type inactivated state in eukaryotic voltage-gated $K^+$ channel has been a great challenge for our field. In this Chapter, I will discuss my attempt and approach to tackle this problem by depleting $K^+$ ions in the Kv1.2-2.1 and thus inducing the selectivity filter to favor the inactivated state. In fact, it is not an entirely novel idea that the depletion of conducting ion (in this case $K^+$) replaced by another cation could drive the selectivity filter into another conformation. The idea of permeant ion effects on gating has been seen previously already and has been characterized functionally [13, 14]. Structurally, this method also has

already been proven to yield the C-type inactivated filter in KcsA [3] (**Figure 1.6**). Most importantly, we believe that the low $K^+$ approach will be a better approach to obtain the native C-type inactivated selectivity filter over introducing mutations, as we are maintaining the WT integrity of the channel.

## Results and Discussion:

### Functional characteristic of Kv1.2-2.1 in high $K^+$ and low $K^+$ in *Xenopus* oocytes

*Xenopus laevis* oocytes have been widely used as an *in vivo* system to study various eukaryotic ion channels upon injection with mRNA since its use in 1971 by Gurdon et al. [15-18]. The electrophysiological functions of *Shaker*, Kv1.2, and Kv1.2-2.1 have all already been recorded [10, 19], so we also used this as the model system for our low $K^+$ characterization in Kv1.2-2.1. Unlike *Shaker*, where the N-terminal "ball and chain" needs to be removed to observe C-type inactivation dynamics, Kv1.2 and Kv1.2-2.1 naturally does not have N-type inactivation. Thus, we used the alpha subunit of the Kv1.2-2.1 without any alterations for the recording. The gene coding for the alpha subunit of Kv1.2-2.1 in pMAX vector was transcribed into mRNA. 50 ng of mRNA was injected into each *Xenopus* oocytes. The cells were incubated at $18\,^{\circ}C$ for 24-48 hrs before experimentation to allow for proper expression of Kv1.2-2.1 and for trafficking onto the cell surface of the oocyte.

To properly exchange high $K^+$ condition with low $K^+$ concentration with $NH_4^+$ or $Na^+$, we used COVG (Cut-Open Vaseline Gap) voltage-clamp with a perfusion cannula (**Figure 2.4d**). This technique has three main advantages. It allows for high-frequency response and low noise recording, high clamp fidelity for measurements up to 20-30 μA, and stable recording condition that can last for hours [20]. Most importantly, this technique allows us to properly access the cell interior and exchange the intracellular medium from high potassium to low potassium environment by replacing with ammonium or sodium. Macroscopic ionic currents were recorded

22

for Kv1.2-2.1 with holding potential at -80 mV, a prepulse at -80 mV for 100 ms, and a variable

pulse from -80 mV to +60 mV for 1 second at 10 mV increments before returning to -80 mV for

250 ms. We compare the three conditions: high $K^+$, low $K^+$ with high $NH_4^+$, low $K^+$ with high $Na^+$.

For each case, the ion concentration in the internal solution was 10x larger than that of external

to allow for proper external current upon depolarizing potentials. The same oocyte was used to

measure all three conditions. The high $K^+$ condition conducts by far the most current, followed

by the high $NH_4^+$ case, which on average conducts ~60% of the high $K^+$ current, and the high

$Na^+$ yields little to no current, showing the progression of C-type inactivation from $K^+$ to $NH_4^+$ to

$Na^+$ (**Figure 2.4 a, b, c**). The difference is more clearly shown in the I-V curve comparing the

three ionic conditions in **Figure 2.4e**.
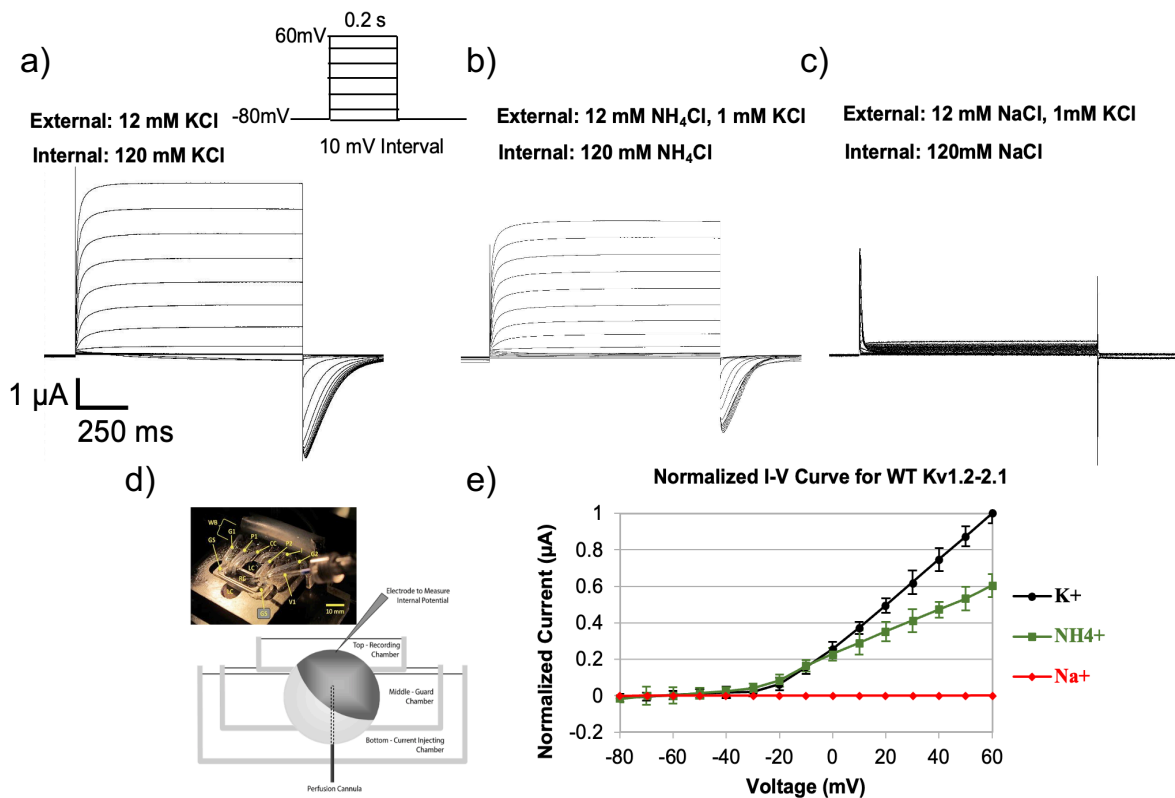


**Figure 2.4:** Ionic current recording of WT Kv1.2-2.1 with COVG to characterize C-type inactivation in low $K^+$ conditions**.** a, b, c) Ionic current recording for high $K^+$ (a), high $NH_4^+$ (b), and high $Na^+$ (c) with variable voltage from -80 mV to +60 mV at 10 mV increments. After each ion exchange in the interior of the oocyte, there was a wait time of ~20 min to allow proper settling of ion inside**.** (n=4 for each condition)**.** d) Schematic diagram of the layout of the COVG voltage clamp technique. e) I-V curve comparing the current for each ionic conditions at each voltage.

**Expression and purification of Kv1.2-2.1 in high K⁺ and low K⁺ in *Pichia pastoris***

Once we observed the functional characterizations for each ionic conditions, we sought to express and purify the WT Kv1.2-2.1 in high K⁺, high NH₄⁺, and high Na⁺ for structural biology. We received the cDNA of the rat Kv1.2-2.1 α subunit co-expressible with rat Kv β2 subunit in the pPICZ-C plasmid as a gift from R. Mackinnon (Rockefeller University). The amplified plasmid was linearized and phenol-chloroform extracted before being transformed via electroporation into *Pichia pastoris* SMD1168 *his4* strain. The transformed cells were plated on YPDS plates at various zeocin concentrations for selection. Because the pPICZ-C has a zeocin resistance gene, the cells with higher copy number of the plasmid transformed would survive in
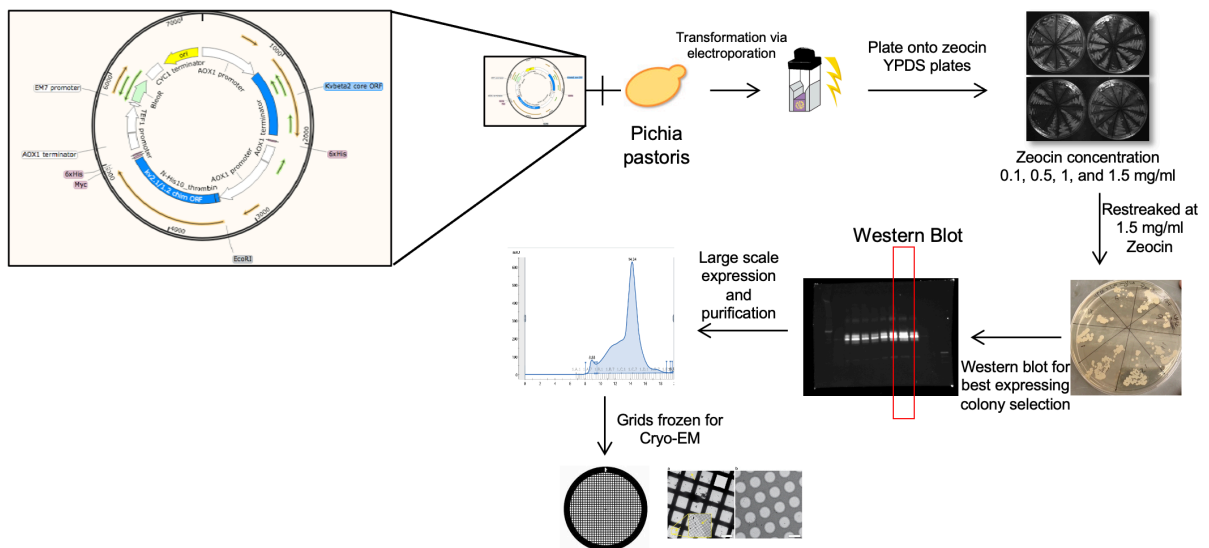


**Figure 2.5:** Schematic of the workflow for transformation/selection/expression/purification of Kv1.2-2.1 WT in *Pichia pastoris*. pPICZ-C plasmid with Kv1.22.1 is transformed into *Pichia pastoris* strain via electroporation. The transformed cells recovered O/N on YPD media and then plated onto YPDS plates with zeocin concentrations 0.1, 0.5, 1.0, and 1.5 mg/mL for selection. The colonies growing in highest concentration of zeocin were restreaked onto 1.5 mg/mL zeocin plate and were tested for expression via small scale expression and western blot. Glycerol stock of the best expressing colony was used for large scale expression and purification for structural biology.

the higher concentration of zeocin. The cells with the highest copy number of the pPICZ-C plasmid are also the most likely to express the most protein. Thus, the cells that survived in the highest concentration of zeocin were restreaked on 1.5 mg/ml zeocin plates and were compared for expression levels using western blot. The Kv1.2-2.1 construct has a His-tag, so we used

anti-His antibodies for the western blot. The colony with the most expression was saved as a

glycerol stock for large scale expression and purification. The purified proteins were then frozen

on grids for cryo-EM data collection. The summary of this workflow is shown in **Figure 2.5**, and

for details of the procedure, we refer to **Materials and Methods** section of this chapter.

a)



b)

c)
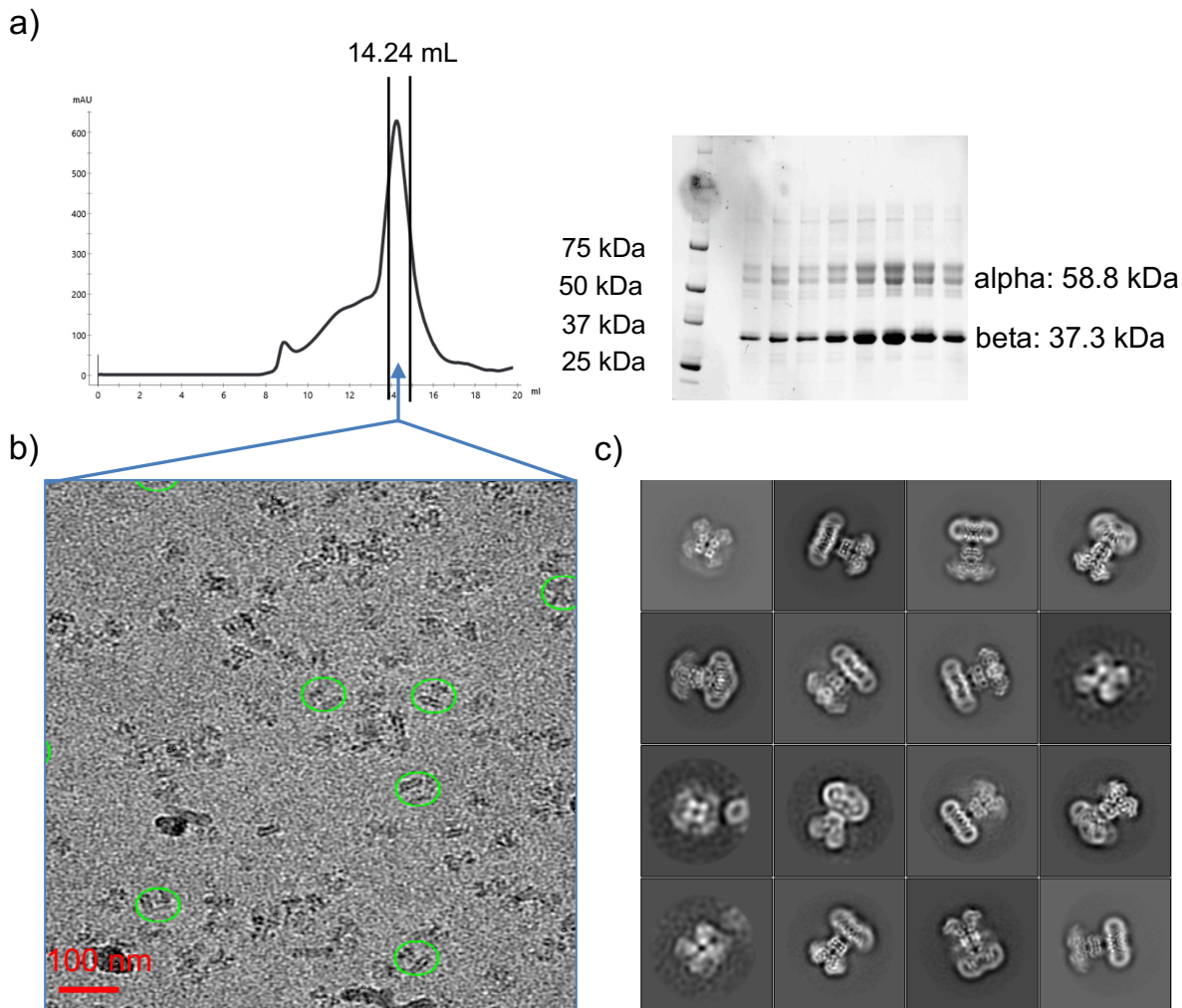
**Figure 2.6:** Purification and cryo-EM of WT Kv1.2-2.1 in high K$^+$ in DDM/CHS with lipids. a) Size exclusion chromatography (SEC) profile of Kv1.2-2.1 in high K$^+$ in DDM/CHS with lipids shows a narrow, gaussian peak at ~14.2 mL in Superose 6 Increase 10/300 column. SDS-PAGE of the peak fractions corresponding to the region indicated by the solid black lines shows the correct sizes indicating the presence of alpha and beta subunits. b) cryo-EM micrograph of high K$^+$ WT Kv1.2-2.1 sample in DDM/CHS with lipids concentrated from the peak fraction in the region indicated by the solid black lines. c) 2D classes of high K$^+$ WT Kv1.2-2.1 in DDM/CHS with lipids from ~384k particles shows a balanced mixture of top, side, and oblique views.

The WT Kv1.2-2.1 in high K$^+$ condition (150 mM KCl) is well-behaved during large-scale

purification in DDM/CHS. There is a single sharp, gaussian peak at ~14.2 mL that corresponds

to the WT Kv1.2-2.1 from the size exclusion chromatography (SEC) profile, as verified by the SDS-PAGE (**Figure 2.6a**). The cryo-EM micrograph collected from the Titan Krios shows a nice distribution of single particles. The 2D classes from ~330k particles shows a balanced mixture of top, side, and oblique views (**Figure 2.6b, c**).

When this purification process was repeated with low $K^+$ conditions where we replaced the 150 mM KCl with 150 mM $NH_4Cl$ or 150 mM NaCl in the final SEC buffer, we encountered a problem. Firstly, the overall protein yield in the SEC profile was much lower in the low $K^+$ conditions compared to the high $K^+$ condition. Given that the purification steps were kept the same among the three conditions except for the SEC buffer, the loss of protein yield most likely occurred at the SEC stage. Furthermore, unlike in the high $K^+$ condition where the SEC profile yielded one sharp peak at ~14.2 mL, the SEC profiles for both low $K^+$ conditions showed two peaks at ~13 mL and ~16 mL (**Figure 2.7a**). The SDS-PAGE showed that the ~13 mL peak corresponded to the full Kv1.2-2.1 protein (with alpha and beta subunits intact as a tetramer) while the ~16 mL peak corresponded to beta subunit only (**Figure 2.7b**), which meant that there is a dissociation of alpha subunit from the beta subunit due to the low $K^+$ conditions. Based on the left-shifted and broader peak for the full Kv1.2-2.1 peak in the low $K^+$ conditions, we also suspected that there may be an aggregation of proteins in the DDM/CHS. This suspicion was proven true when we screened the grids frozen with the sample from those peaks with the Talos. Although the quality of the micrographs is worse in the low $K^+$ conditions compared to those in the high $K^+$ condition where images were taken from the Krios microscope, we can clearly see the presence of aggregation in the low $K^+$ micrographs (**Figure 2.7c**).

To resolve this aggregation/dissociation issue, we sought to stabilize the low $K^+$ conditions by reconstituting the Kv1.2-2.1 into nanodiscs. We ran the initial SEC in DDM/CHS with 150 mM KCl and reconstituted the proteins in nanodiscs overnight with MSPE3D1 and a lipid mixture of POPC: E: G at 3:1:1 (refer to **Materials and Methods** for details). Once the protein was fully reconstituted, we replaced the 150 mM KCl with either 150 mM $NH_4Cl$ or NaCl

with no KCl in the nanodisc SEC buffer. The presence of the nanodisc stabilized the protein and

prevented the aggregation/dissociation of Kv1.2-2.1 even in the presence of low $K^+$ (**Figure**

**2.8a, c**).
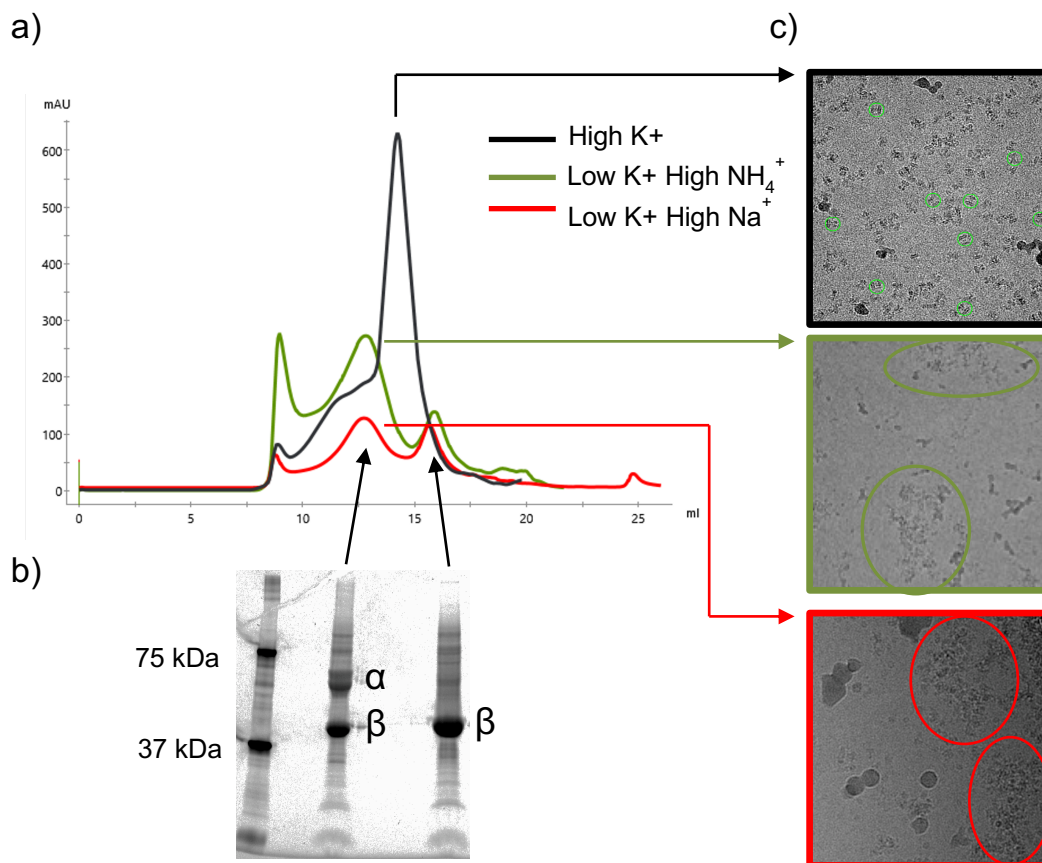


**Figure 2.7:** Low $K^+$ conditions are not stable in DDM/CHS with lipids. a) Both low $K^+$ conditions ($NH_4^+$ or $Na^+$) exhibit a significantly lower yield from size exclusion chromatography compared to high $K^+$ condition. Furthermore, central peak at ~14.2 mL is shift to the left to ~13 mL, indicating the presence of aggregation of proteins. (c) This aggregation can be clearly seen in the cryo-EM micrographs. The second peak at ~16 mL in low $K^+$ condition corresponds to beta subunit of Kv1.2-2.1 alone from SDS-PAGE (b), signifying that the low $K^+$ condition induces the dissociation between the alpha and beta subunits during purification.

The fractions corresponding to the first peak (~14.16 mL) showed intact Kv1.2-2.1 WT

properly reconstituted in nanodisc (**Figure 2.8b**). The sample was concentrated and frozen on a

Quantifoil grid and was imaged with the Krios microscope. The samples imaged on the Krios

microscope revealed nice distribution of single particles with a good balance of top, side, and

oblique views (**Figure 2.8c, d**). The nanodisc stabilized the low $K^+$ condition that had created

aggregation and dissociation between alpha and beta subunits in detergent DDM/CHS with

lipids.
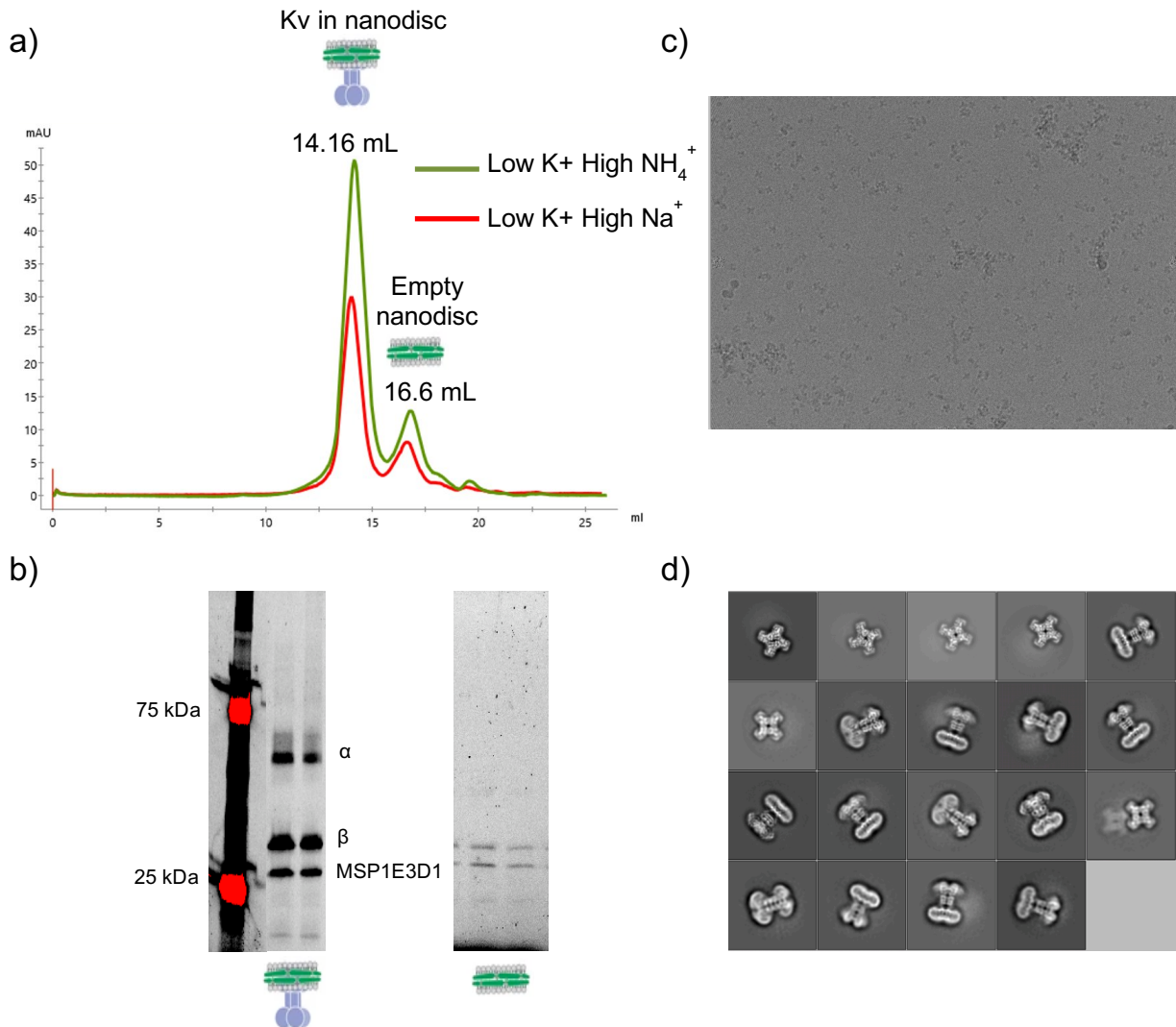


**Figure 2.8:** WT Kv1.2-2.1 in low K$^+$ is stable without aggregation or dissociation when reconstituted in nanodisc**.** a) SEC profile of WT Kv1.2-2.1 in low K$^+$ conditions reconstituted in nanodisc exhibits a stable protein complex peak at ~14.16 mL followed by a smaller empty nanodisc peak at ~16.6 mL. b) SDS-PAGE gel of samples collected from each fraction. The first peak shows the presence of full Kv1.2-2.1 successfully incorporated into a nanodisc, while the second peak shows empty nanodisc. c) Micrograph of the WT Kv1.2-2.1 low K$^+$ (high NH$_4^+$) in nanodisc sample collected with the Krios. We can observe clear single particles of both top and side views. High Na$^+$ condition exhibited similar results. d) 2D classes of WT Kv1.2-2.1 in low K$^+$ (high NH$_4^+$) and in nanodiscs show a balanced mixture of top, side, and oblique views of the particles. High Na$^+$ exhibited similar results.

Kv1.2-2.1 WT samples in high $K^+$ in DDM/CHS with lipids, low $K^+$ and high $NH_4^+$ in ND, and low $K^+$ and high $Na^+$ in ND were concentrated and plunge-frozen in liquid ethane on either Quantifoil Cu 200 or 300 1.2/1.3 grids. The datasets for each sample were collected from the Titan Krios from either the University of Chicago or Stanford-SLAC cryo-EM facilities. The data was processed in RELION 3, and the workflow of the processing is described in **Figure 2.9-11**.
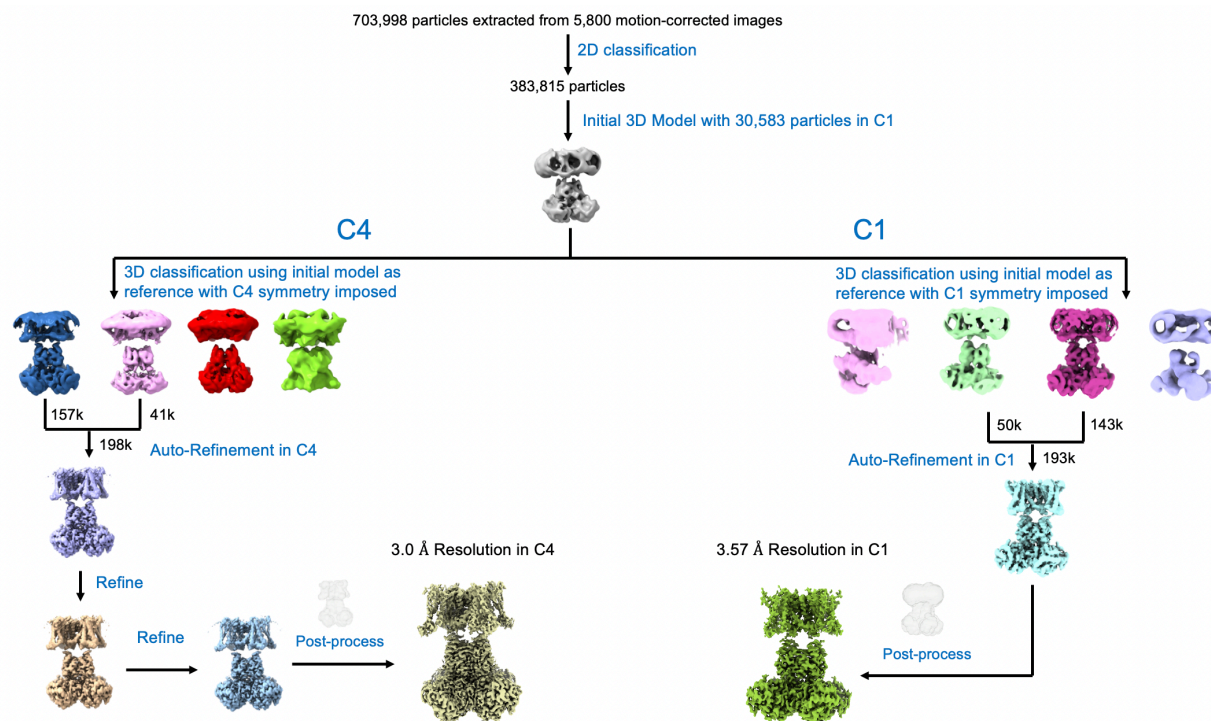


**Figure 2.9:** Cryo-EM Data Processing Workflow for Kv1.2-2.1 WT in high $K^+$ DDM/CHS with lipids 703,998 particles were extracted from 5,800 motion-corrected images using crYOLO. After three rounds of 2D classifications, 383,815 particles were picked for initial 3D model construction and 3D classification. Initial 3D model was created with ~30k particles and was used for 3D classification. At the 3D classification stage either C4 or C1 symmetry was imposed, which was carried throughout the processing for each condition separately to yield either C4 or C1 post-processed structure. For the C4 3D classes, a total of ~198k particles were picked from classes 1 (157k particles) and 2 (41k particles) for auto-refinement. For the C1 3D classes, a total of ~193k particles were picked from classes 2 (50k particles) and 3 (143k particles) for auto-refinement. For C4, refined structure was further refined after Bayesian polishing before being post-processed using a tight mask, yielding a 3.0 Å resolution structure. For C1, post-processed structure of 3.57 Å resolution was obtained.

For the high $K^+$ condition, of the ~704k particles picked from trained crYOLO program [21], ~384k particles were selected for further processing with 3D classification. ~30k particles were used to build the initial 3D model, which was used as a reference for the 3D classification with

either C4 or C1 symmetry imposed. With C4 classification, ~198k particles from classes 1 and 2 were pooled for auto-refinement in C4 to yield a final post-processed structure of 3.0 Å resolution. With C1 classification, ~193 particles from classes 2 and 3 were pooled for auto-refinement in C1 to yield a final post-processed structure of 3.57 Å resolution (**Figure 2.9**). The resolutions of these structures can be verified by the FSC curves using the 0.143 FSC criteria (**Figure 2.12a**).
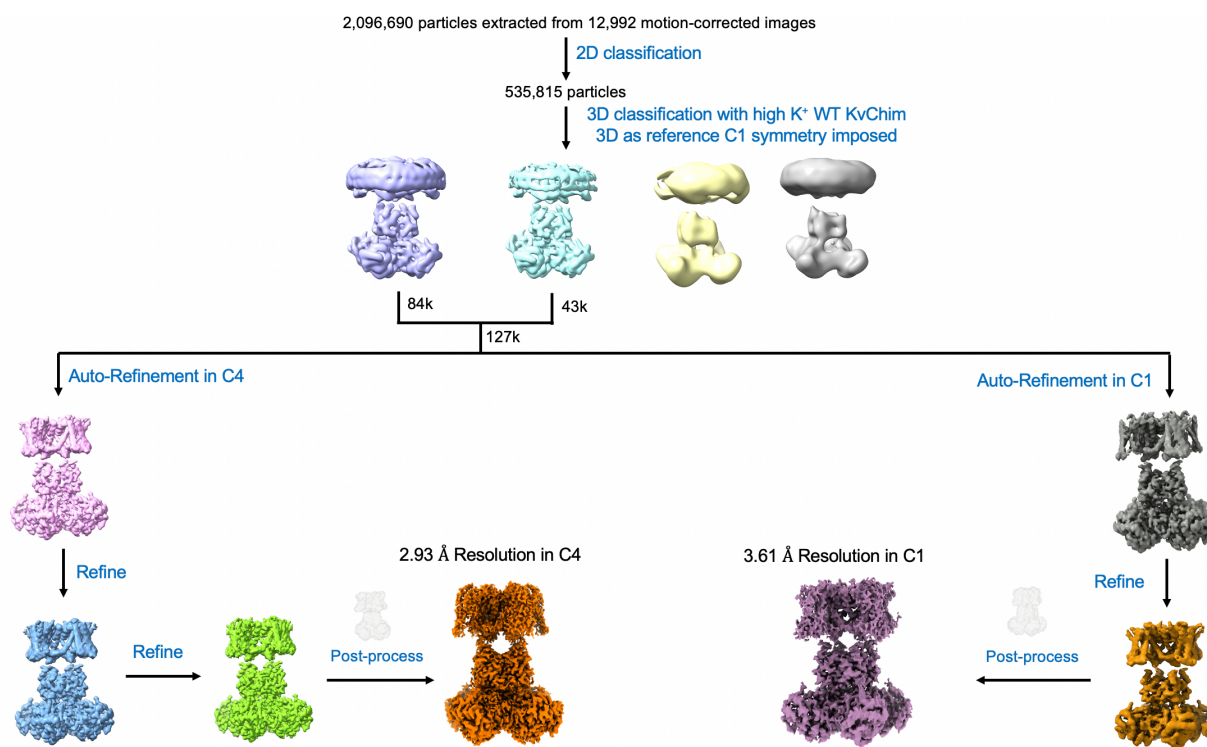


**Figure 2.10:** Cryo-EM Data Processing Workflow for Kv1.2-2.1 WT in low K$^+$ high NH$_4^+$ ND 2,096,690 particles were extracted from 12,992 motion-corrected images using crYOLO. After three rounds of 2D classifications, 535,815 particles were picked for 3D classification with C1 symmetry imposed. The 3D classification was done using the 3D structure of WT Kv1.2-2.1 in high K$^+$ condition as a reference. From here, a total of ~127k particles were picked from classes 1 (84k particles) and 2 (43k particles) for auto-refinement with either C4 or C1 symmetry imposed. After further refinement after Bayesian polishing, both C4 and C1 structures were post-processed in a tight mask to yield 2.93 Å and a 3.61 Å resolution structures, respectively.

For the low K$^+$ high NH$_4^+$ condition in ND, of the ~2.1M particles picked from trained crYOLO program [21], ~536k particles were selected for 3D classification. Here, the WT Kv1.2-2.1 structure in high K$^+$ condition was used as a reference for the 3D reconstruction in C1 symmetry. From here, a total of ~127k particles were picked for auto-refinement with either C4

or C1 symmetry imposed. After further refinement, C4 and C1 structures were post-processed to yield a 2.93 Å and a 3.61 Å resolution structures, respectively (**Figure 2.10**). The resolutions of the structures can be verified by the FSC curves using the 0.143 FSC criteria (**Figure 2.12a**).



3,284,683 particles extracted from 13,356 motion-corrected images

2D classification

464,808 particles

3D classification with high K⁺ WT KvChim 3D as reference C1 symmetry imposed

107k      79k

186k

Auto-Refinement in C4

Auto-Refinement in C1

Refine

3.11 Å Resolution in C4

3.65 Å Resolution in C1

Post-process

Post-process
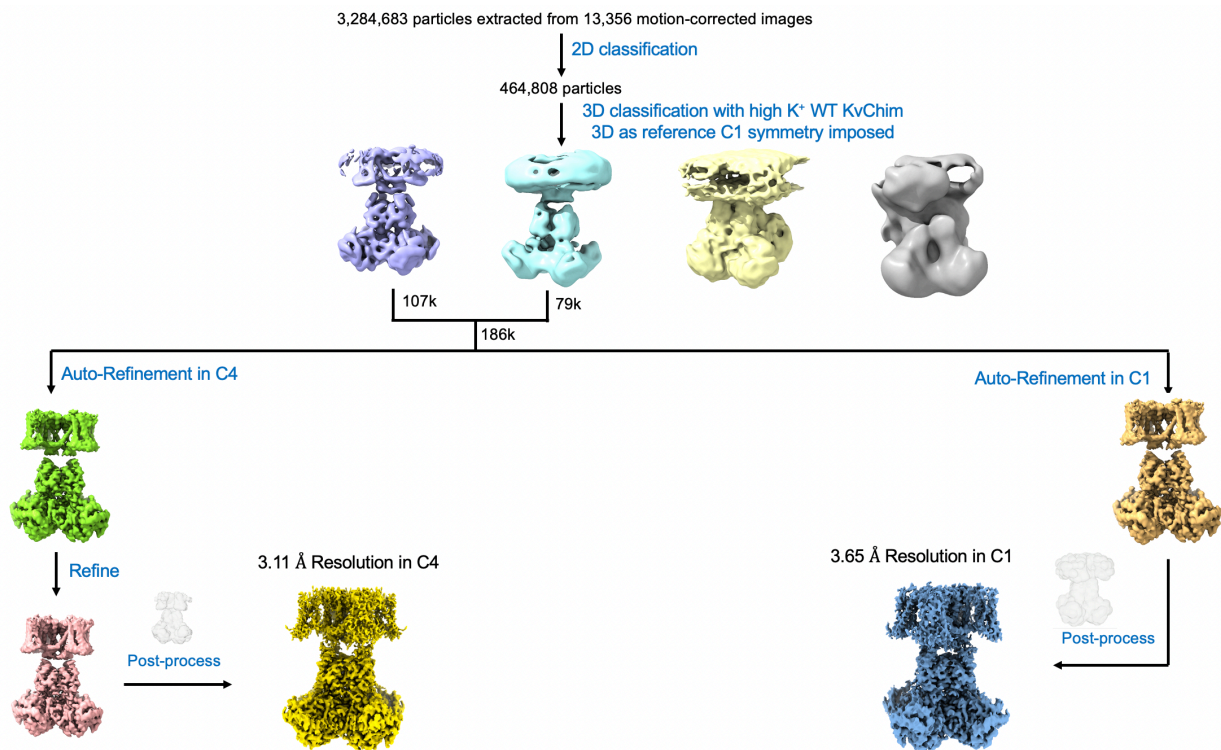
**Figure 2.11:** Cryo-EM Data Processing Workflow for Kv1.2-2.1 WT in low K⁺ high Na⁺ ND 3,284,683 particles were extracted from 13,356 motion-corrected images using crYOLO. After three rounds of 2D classifications, 464,808 particles were picked for 3D classification with C1 symmetry imposed. The 3D classification was done using the 3D structure of WT Kv1.2-2.1 in high K⁺ condition as a reference. From here, a total of ~186k particles were picked from classes 1 (107k particles) and 2 (79k particles) for auto-refinement with either C4 or C1 symmetry imposed. After further refinement after Bayesian polishing, both C4 and C1 structures were post-processed in a tight mask to yield 3.11 Å and a 3.65 Å resolution structures, respectively.

For the low K⁺ high Na⁺ condition in ND, of the ~3.3M particles picked from trained crYOLO program [21], ~465k particles were selected for 3D classification. Here, the WT Kv1.2-2.1 structure in high K⁺ condition was used as a reference for the 3D reconstruction in C1 symmetry. From here, a total of ~186k particles were picked for auto-refinement with either C4 or C1 symmetry imposed. After further refinement, C4 and C1 structures were post-processed to yield a 3.11 Å and a 3.65 Å resolution structures, respectively (**Figure 2.11**). The resolutions of the structures can be verified by the FSC curves using the 0.143 FSC criteria (**Figure 2.12a**).
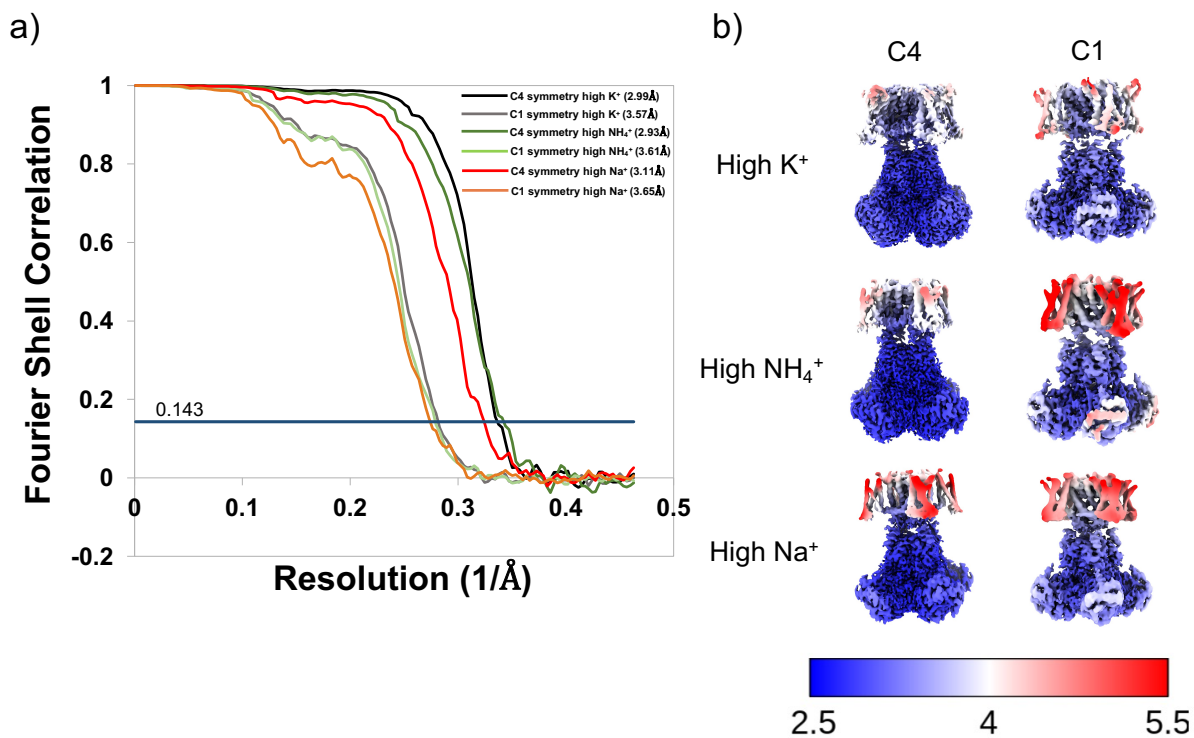
**Figure 2.12:** FSC curves and local resolution for WT Kv1.2-2.1 in high $K^+$, $NH_4^+$, and $Na^+$ with C4 and C1 symmetry imposed. a) FSC curve indicates the resolution of each structure according to the 0.143 FSC criteria. b) cryo-EM density maps of high $K^+$, $NH_4^+$, and $Na^+$ in either C4 or C1 symmetry are filtered and colored according to their local resolutions.

The local resolution estimation from RELION 3 was used to calculate the local resolution of each density map. The cytosolic domain is overall higher in resolution, with the transmembrane by itself being ~4.0-5.0 Å in resolution. The resolution in the TM is higher near the pore domain and specifically in the selectivity filter (3-3.5 Å) and becomes lower in the voltage-sensing domains (4-5.5 Å). The cryo-EM and model building statistics are shown in **Table 2.1**.

**Table 2.1:** Cryo-EM and model building statistics for Kv1.2-2.1 high and low K$^+$

| **Data Collection** | |
|---|---|
| Protein concentration | 6.02 mg/mL (high K$^+$ in DDM/CHS), 1.7 mg/mL (high NH$_4^+$ in ND), 1.2 mg/mL (high Na$^+$ in ND) |
| Sample volume for EM grid | 3.5 µL (for all conditions) |
| Grid type | Quantifoil Cu 1.2/1.3 (for all conditions) |
| Plunge freezer | Mark IV ThermoFisher (for all conditions) |
| Blotting time | 3.5 s (for all conditions) |
| Blotting temperature | 22 ℃ (for all conditions) |
| Blotting chamber humidity | 100%/100% (for all conditions) |
| Microscope | FEI Titan Krios (for all conditions) |
| Voltage | 300 kV (for all conditions) |
| Camera | Gatan K3 (for all conditions) |
| Energy Filter | Yes (for all conditions) |
| Cs corrector | No (for all conditions) |
| Nominal defocus range | -1.5 to -2.1 µm (high K$^+$), -1.0 to -2.5 µm (high NH$_4^+$), -1.5 to -2.3 µm (high Na$^+$) |
| Physical pixel size | 1.08 Å/px (for all conditions) |
| Super-resolution pixel size | 0.54 Å/px (for all conditions) |
| Total dose | 50 e-/Å2 (for all conditions) |
| Number of frames | 40 frames (for all conditions) |
| Exposure time | 12 s (for all conditions) |
| Number of images collected | 5,800 images (high K+), 12,992 images (high NH$_4^+$), 13,356 images (high Na$^+$) |
| | |
| **Reconstruction (Relion 3)** | |
| Number of motion-corrected images used for processing | 5,800 images (high K$^+$), 12,992 images (high NH$_4^+$), 13,356 images (high Na$^+$) |
| Picked particle number | 703,998 (high K$^+$), 2,096,690 (high NH$_4^+$), 3,284,683 (high Na$^+$) |
| Particle number after 2D classification | 383,815 (high K$^+$), 535,815 (high NH$_4^+$), 464,808 (high Na$^+$) |
| Final particle number in C4 | 236,385 (high K$^+$), 126,668 (high NH$_4^+$), 225,593 (high Na$^+$) |
| Final particle number in C1 | 193,582 (high K$^+$), 105,032 (high NH$_4^+$), 78,910 (high Na$^+$) |
| Full molecule resolution in C4 FSC = 0.143 | 3.0 Å (high K$^+$), 2.93 Å (high NH$_4^+$), 3.11 Å (high Na$^+$) |
| Full molecule resolution in C1 FSC = 0.143 | 3.57 Å (high K$^+$) , 3.61 Å (high NH$_4^+$), 3.65 Å (high Na$^+$) |
| Map sharpening B-factor in C4 | -111.858 (high K$^+$), -96.6 (high NH$_4^+$), -102.823 (high Na$^+$) |
| Map sharpening B-factor in C1 | -128.698 (high K$^+$), -105.353 (high NH$_4^+$), -101.279 (high Na$^+$) |
| | |
| **RMS deviations** | |
| Bond length | 0.0073 Å (high K$^+$ C4), 0.0079 Å (high K$^+$ C1), 0.005 Å (high NH$_4^+$ C4), 0.0046 Å (high NH$_4^+$ C1), 0.0049 Å (high Na$^+$ C4), 0.0028 Å (high Na$^+$ C1) |
| Bond angle | 0.88° (high K$^+$ C4), 0.84° (high K$^+$ C1), 0.83° (high NH$_4^+$ C4), 0.72° (high NH$_4^+$ C1), 0.79° (high Na$^+$ C4), 0.63° (high Na$^+$ C1) |
| | |
| **Ramachandran plot** | |
| Favored (%) | 92.34% (high K$^+$ C4), 92.97% (high K$^+$ C1), 88.32% (high NH$_4^+$ C4), 95.99% (high NH$_4^+$ C1), 89.05% (high Na$^+$ C4), 95.26% (high Na$^+$ C1) |
| Allowed (%) | 7.66% (high K$^+$ C4), 7.03% (high K$^+$ C1), 11.32% (high NH$_4^+$ C4), 4.01% (high NH$_4^+$ C1), 10.95% (high Na$^+$ C4), 4.74% (high Na$^+$ C1) |
| Outlier (%) | 0.00% (high K$^+$ C4), 0.00% (high K$^+$ C1), 0.36% (high NH$_4^+$ C4), 0.00% (high NH$_4^+$ C1), 0.00% (high Na$^+$ C4), 0.00% (high Na$^+$ C1) |
| | |
| **Validation** | |
| MolProbity Score | 2.13 (high K$^+$ C4), 2.08 (high K$^+$ C1), 2.36 (high NH$_4^+$ C4), 1.99 (high NH$_4^+$ C1), 2.27 (high Na$^+$ C4), 1.89 (high Na$^+$ C1) |
| Clash Score | 13.96 (high K$^+$ C4), 13.17 (high K$^+$ C1), 18.52 (high NH$_4^+$ C4), 16.24 (high NH$_4^+$ C1), 15.73 (high Na$^+$ C4), 11.17 (high Na$^+$ C1) |
| EM Ringer Score | 1.89 (high K$^+$ C4), 1.06 (high K$^+$ C1), 1.1 (high NH$_4^+$ C4), 1.21 (high NH$_4^+$ C1), 2.01 (high Na$^+$ C4), 1.17 (high Na$^+$ C1) |

When we initially tried to fit the WT Kv1.2-2.1 X-ray crystal structure (PDB ID: 2r9r) [1] into our cryo-EM density for all of the constructs, we realized that there is a slight shift/rotation of the cytosolic domain (composed of β subunit and the T1 domain of the α subunit) relative to the TM domain in the density (some with more shift/rotations than others). This rotation is unsurprising since the TM and the cytosolic domains are linked by a long, flexible linker [1, 9, 11]. We noticed no trend between the degree of rotation of TM to cytosolic domain relative to the 2r9r crystal structure and the low $K^+$ conditions. To address this issue of rotation, we built two separate models for the TM and the cytosolic domains to allow each domain to align better with the density maps before fitting and performing real-space refinement (**Figure 2.13**). In the cytosolic region, we noticed very little difference across all of the structures, whether in C4 or C1 symmetry, compared to the 2r9r crystal structure. Also, because this region is high resolution in all of the density maps (2.4-3.3 Å), cryo-EM densities for most of the side chains were clearly visible.



**Figure 2.13:** Comparison of the structures of Kv1.2-2.1 in high $K^+$ in DDM/CHS with lipids, high $NH_4^+$ in ND, and high $Na^+$ in ND with PDB ID: 2r9r in DDM. Each of the high $K^+$ (black), high $NH_4^+$ (green), and high $Na^+$ (red) conditions are overlapped with 2r9r structure (yellow). Generally, there seems to be little structural differences between high $K^+$, high $NH_4^+$, and high $Na^+$ in both TM and cytosolic domains compared to PDB 2r9r.

In the TM domain, we also observe very small global structural differences between 2r9r, high K$^+$, and the low K$^+$ structures (**Figure 2.13**). The VSD domains, especially in the low K$^+$ conditions, were relatively low in resolution (4-5.5 Å) (**Figure 2.12b**). However, any conformational changes due to C-type inactivation of Kv1.2-2.1 from the low K$^+$ conditions would occur in the pore domain, where the TM resolution is the highest (2.7-3.5 Å). Specifically, the changes will be predominantly in the selectivity filter and perhaps the intracellular gate. Furthermore, we expect C-type inactivated state to undergo subtle conformational changes that prevent conduction through the pore. Therefore, we focused our attention on the pore domain.

Since the original Kv1.2-2.1 structure (PDB ID: 2r9r) was solved in high K$^+$ environment in detergent, we expect our high K$^+$ condition in DDM/CHS with lipids to most resemble the 2r9r. Taking a closer look at the selectivity filter, we observe that the high K$^+$ condition matches precisely with 2r9r, from side chain conformation to carbonyl oxygen conformations. The low K$^+$ conditions also adopt a conductive-like conformation and matches quite well to 2r9r. However, the low K$^+$ structures show slight deviations in carbonyl oxygen conformations and a slight bulge near the G372 residue (**Figure 2.14b**). Next, we looked at the critical D375-W362 hydrogen bond interaction. First discovered in *Shaker* and later also shown in Kv1.2, mutants that destroy this hydrogen bond interaction prevents ion conductance completely  [22, 23]. The W434F mutant in *Shaker*, for example, is known for its nonconducting properties and is used for gating current measurements. Given the standard hydrogen bond length of 2.5-3.2 Å [24], 2r9r and high K$^+$ structures maintain the hydrogen bond between D375 and W362. In both low K$^+$ structures, however, the D375-W362 hydrogen bond is either weakened or disrupted (**Figure 2.14c**) as the two residues become too far apart. These slight deviations in the selectivity filter and the D375-W362 distance could indicate a selectivity filter that undergoes slight conformational change necessary to prevent conduction in the low K$^+$ structures.
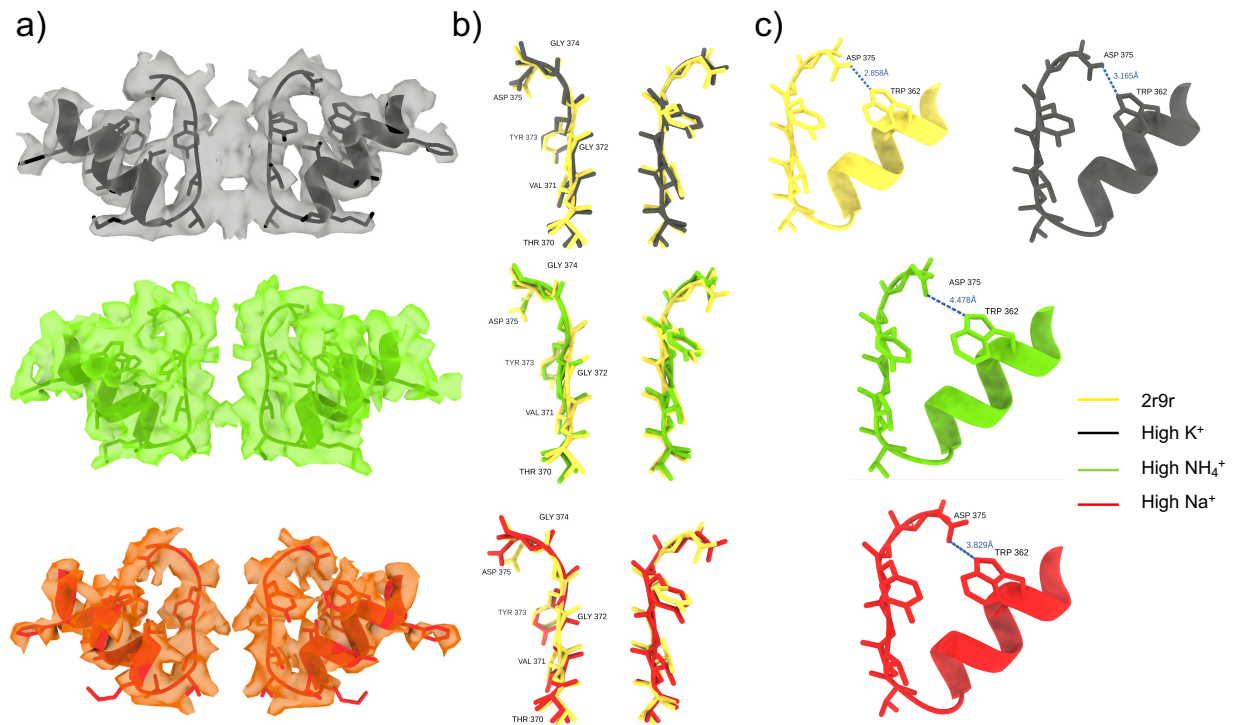
**Figure 2.14:** Comparison of selectivity filter conformation and ion occupancy among 2r9r, high K⁺, and low K⁺ structures**.** The selectivity filter of 2r9r X-ray crystal structure (yellow) is compared with high K⁺ (black), high $NH_4^+$ (green), and high Na⁺ (red) cryo-EM structures. a) Selectivity filters of Kv1.2-2.1 for the three ionic conditions are shown with corresponding cryo-EM map with C1 symmetry imposed. While high K⁺ condition displays ions occupying $S_1$-$S_4$ binding sites in the filter, both low K⁺ conditions display a lack of ions occupying the filter. In high $NH_4^+$, ion only occupies S3 binding site, while there is no ion occupying the filter in the high Na⁺ condition. b) Selectivity filter of 2r9r is overlapped with selectivity filter of high K⁺, high $NH_4^+$, and high Na⁺. The high K⁺ structure is very similar to 2r9r. Both low K⁺ structures display a slight bulge near the G372 residue compared to 2r9r. c) D375-W362 hydrogen bond is shown for each structure.

This hypothesis is further strengthened when we look at the cryo-EM density in C1 symmetry (**Figure 2.14a**). While high K⁺ condition displays ions occupying $S_1$-$S_4$ binding sites in the selectivity filter, both low K⁺ conditions lack ions in the filter. In the high $NH_4^+$ condition, only $S_3$ site is occupied, while there is no ion occupying the filter in the high Na⁺ condition.
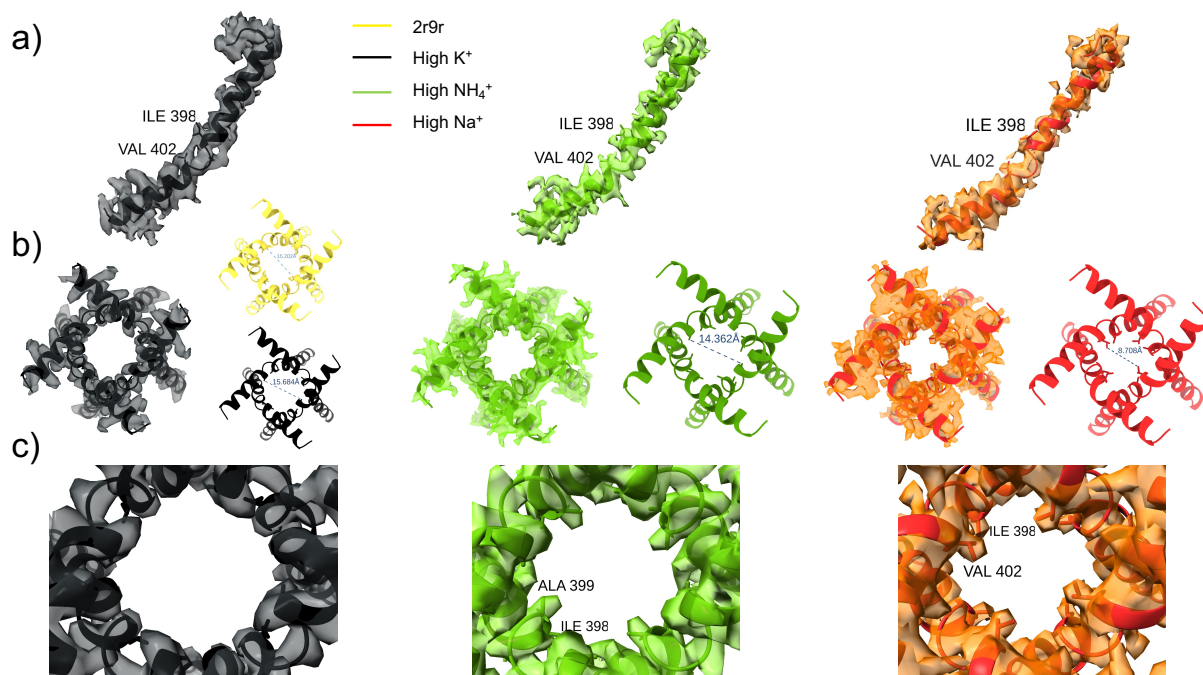
**Figure 2.15:** The intracellular gate is narrower in high $Na^+$ and high $NH_4^+$ conditions due to side chain conformational change in I398 and V402 despite being in opened conformation**.** High $K^+$ (black), $NH_4^+$ (green), and $Na^+$ (red) structures overlapped with density maps in C4 symmetry. a) The S6 helix for all three conditions adopts the opened conformation as seen from PDB 2r9r. b) View of the intracellular gate from the bottom. The width of the gate is estimated by measuring the distance between V402 from opposite subunits. While all three conditions adopt an opened S6 conformation, the gate is significantly narrower in low $K^+$ conditions, especially high $Na^+$. c) Closer view of the intracellular gate shows that the conformational changes in I398 and V402 in low $K^+$ structures narrow the intracellular gate in these conditions compared to the high $K^+$ condition.

Next, we examined the intracellular gate to see if ion conduction may be affected in this region of the pore domain. Looking at the S6 helix by itself, high $K^+$ and low $K^+$ (both high $NH_4^+$ and $Na^+$) conditions all exhibit an open gate conformation (**Figure 2.15a**). The bent S6 helix is reminiscent of the classic opened-gate conformation. Looking at the intracellular gate from the bottom, however, we notice that there is a significant difference in the width of the gate. Here we estimate the width of the intracellular gate by measuring the distance between V402 from opposite subunits (**Figure 2.15b**). Both 2r9r and high $K^+$ structure show an opening of ~15.2 and ~15.7 Å, respectively. High $NH_4^+$ structure displays an opening of ~14.3 Å, while the high $Na^+$ structure shows an opening of ~8.7 Å. As shown in **Figure 2.15c**, this is due to the conformational change in the I398 and V402 in the low $K^+$ structures, especially the high $Na^+$

structure. The V402 in high Na$^+$ narrows the gate width by protruding into the gate (**Figure 2.15c**).

## MDFF simulations on Kv1.2-2.1 high K$^+$ and low K$^+$ structures

Although the resolution of the pore domain is higher than that of the VSDs, it may still be too low across most of the structures to capture the conformation of the selectivity filter accurately (**Figure 2.14a**). In other words, the density map at these resolution could allow slightly varying conformations. To explore any possible conformations of the model that could be consistent with the experimental density map, we used MDFF (Molecular Dynamics Flexible Fitting) simulations [25]. To allow the models to fully explore the density map without leaving it, we used a value of the scaling factor ξ of 0.3 kcal/mol and a harmonic restraint constant of $k_\mu$ of 200 kcal mol$^{-1}$ Å$^{-2}$ throughout the 10 ns simulation. We followed each simulation frame-by-frame by comparing the Cα-Cα distances between two opposing subunits (B-H and D-F subunit distances) for each residue in the selectivity filter (TVGYGD) (**Figures 2.16-2.21a**). The Cα-Cα distance for B-H and D-F subunit during the 10 ns MDFF simulation is shown in **Figures 2.16-2.21c**. Ten thousand frames were generated from the simulation, where each frame corresponds to a time interval of one picosecond. Then the Cα-Cα distances are binned using the bin size of 0.5 Å to generate a histogram of distance (in Å) vs number of frames. Since these are binned histogram depicting how often specific distances are observed during the simulation, there is no information about when in the simulation certain distances occur. However, this analysis reveals any possible stable Cα states for each residue throughout MDFF. In cases where we observe one gaussian peak, the Cα generally explored only one state throughout the simulation. For T370, V371, Y373, and D375, one gaussian peak for all three ionic conditions were observed for both B-H and D-F pairs, suggesting that Cα for these residues did not move very much throughout the simulations (**Figures 2.16b, 2.17b, 2.19b,**

38

**2.21b**). For glycine residues in the selectivity filter (G372 and G374), however, we observed some interesting behaviors. In G372, we observed three distinct states for all three ionic conditions (Cα-Cα distances at 8, 6, and 4 Å) in both pairs of opposing subunits (**Figure 2.18b**). Considering that Cα-Cα distances between opposing subunits is ~8 Å in a conductive selectivity filter, 6 and 4 Å states appears to be constricted states of the G372 that is explored. In G374, we see only one Cα-Cα state at ~8 Å for the high K$^+$ condition in both B-H and D-F pairs. For low K$^+$ structures, however, we observe two Cα-Cα states, at ~8 Å and ~11 Å (**Figure 2.20b**). Interestingly, however, one pair of distances (B-H) only has one state at ~8 Å while the other (D-F) exhibits a dilation behavior. In other words, there appears to be an asymmetric dilation at G374 for the low K$^+$ structures.

To observe the behavior of B-H and D-F at the same time in the simulation, we plotted a 2D histogram of B-H vs D-F Cα-Cα distances (**Figures 2.16-2.21d**). For T370, V371, Y373, and D375, we observe 2D plots with points concentrated near a certain value (9-9.5 Å for T370, 8 Å for V371, 8.5 Å for Y373, and 14-14.5 Å for D375) with small deviations from the y = x line for all three ionic conditions, which suggests that the B-H and D-F distances are quite symmetric throughout the simulation and Cα atoms only occupy one dominant state in all four subunits (**Figures 2.16d, 2.17d, 2.19d, 2.21d**). In other words, these residues are quite stable during the MDFF simulations for both high and low K$^+$ conditions. For G372, we observe a 2D histogram that suggests an asymmetric constriction or pinching for all ionic conditions (given the ⌐ shape in the 2D plot) (**Figure 2.18d**). In other words, when B-H Cα-Cα is constricted, D-F prefers to be conductive and vice-versa. For G374, we observe points concentrated at ~8 Å with small deviations from the y = x line for high K$^+$ suggesting a stable one state for the Cα atoms for this case. This is similar to behaviors seen for T370, V371, Y373, and D375. For low K$^+$ structures, however, we observe an asymmetric dilation (where B-H has one state but D-F has a standard and dilated state) (**Figure 2.20d**).

**Figure 2.16:** T370 Cα-Cα distance analysis between B-H and D-F opposing subunits during 10 ns MDFF trajectories of WT Kv1.2-2.1 structures in high K$^+$ (black), high NH$_4^+$ (green), and high Na$^+$ (red) conditions.
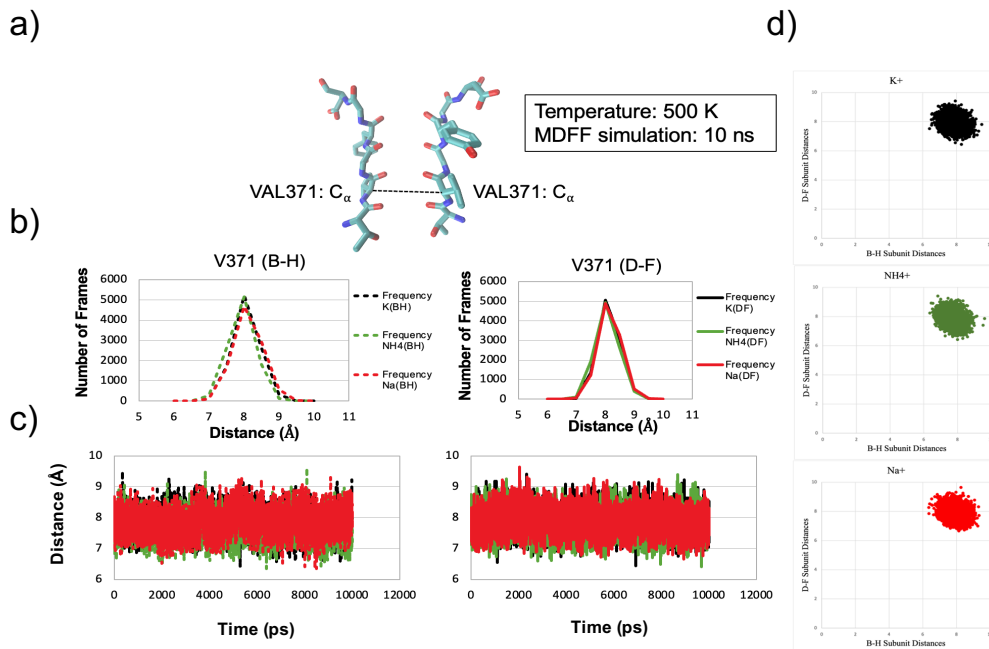


**Figure 2.17:** V371 Cα-Cα distance analysis between B-H and D-F opposing subunits during 10 ns MDFF trajectories of WT Kv1.2-2.1 structures in high K$^+$ (black), high NH$_4^+$ (green), and high Na$^+$ (red) conditions.
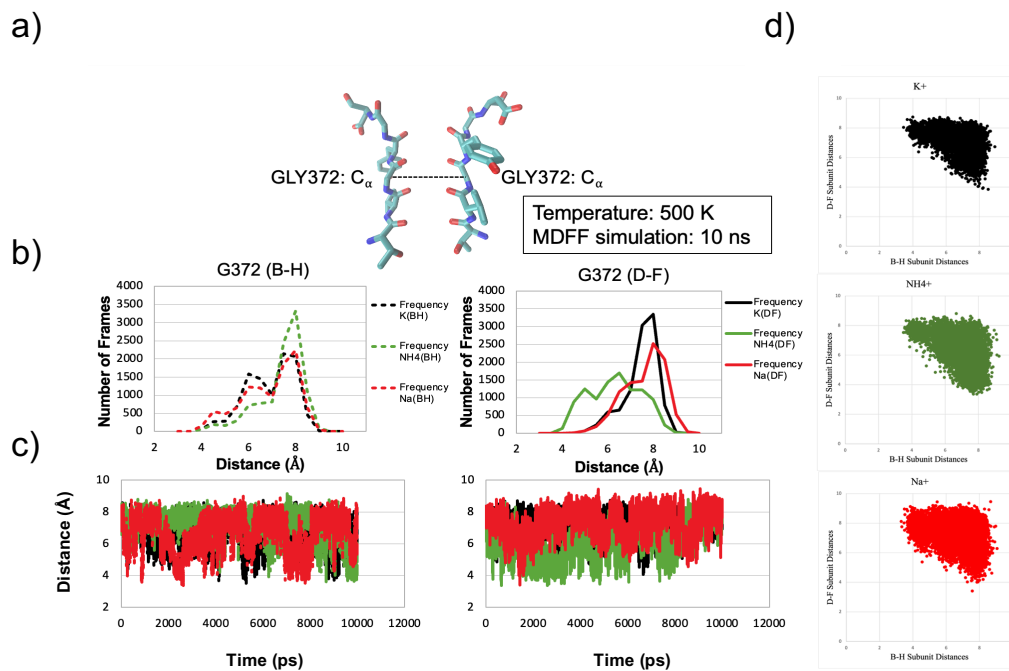
**Figure 2.18:** G372 Cα-Cα distance analysis between B-H and D-F opposing subunits during 10 ns MDFF trajectories of WT Kv1.2-2.1 structures in high K⁺ (black), high NH₄⁺ (green), and high Na⁺ (red) conditions.
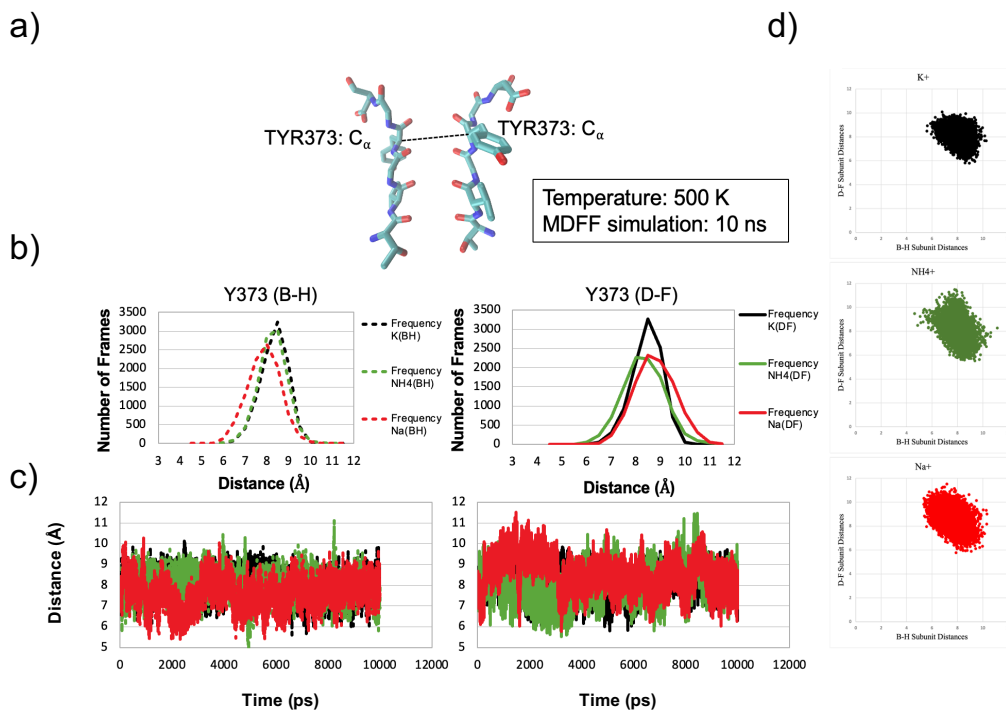


**Figure 2.19:** Y373 Cα-Cα distance analysis between B-H and D-F opposing subunits during the 10 ns MDFF trajectories of WT Kv1.2-2.1 structures in high K⁺ (black), high NH₄⁺ (green), and high Na⁺ (red) conditions.

41

**Figure 2.20:** G374 Cα-Cα distance analysis between B-H and D-F opposing subunits during 10 ns MDFF trajectories of WT Kv1.2-2.1 structures in high K⁺ (black), high NH₄⁺ (green), and high Na⁺ (red) conditions.
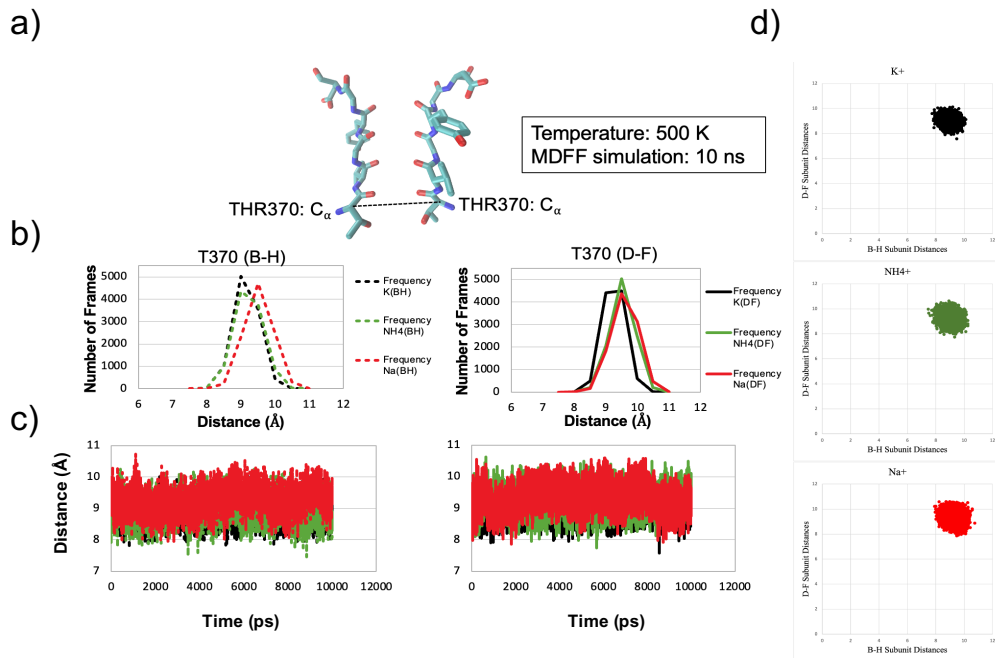


**Figure 2.21:** D375 Cα-Cα distance analysis between B-H and D-F opposing subunits during 10 ns MDFF trajectories of WT Kv1.2-2.1 structures in high K⁺ (black), high NH₄⁺ (green), and high Na⁺ (red) conditions.
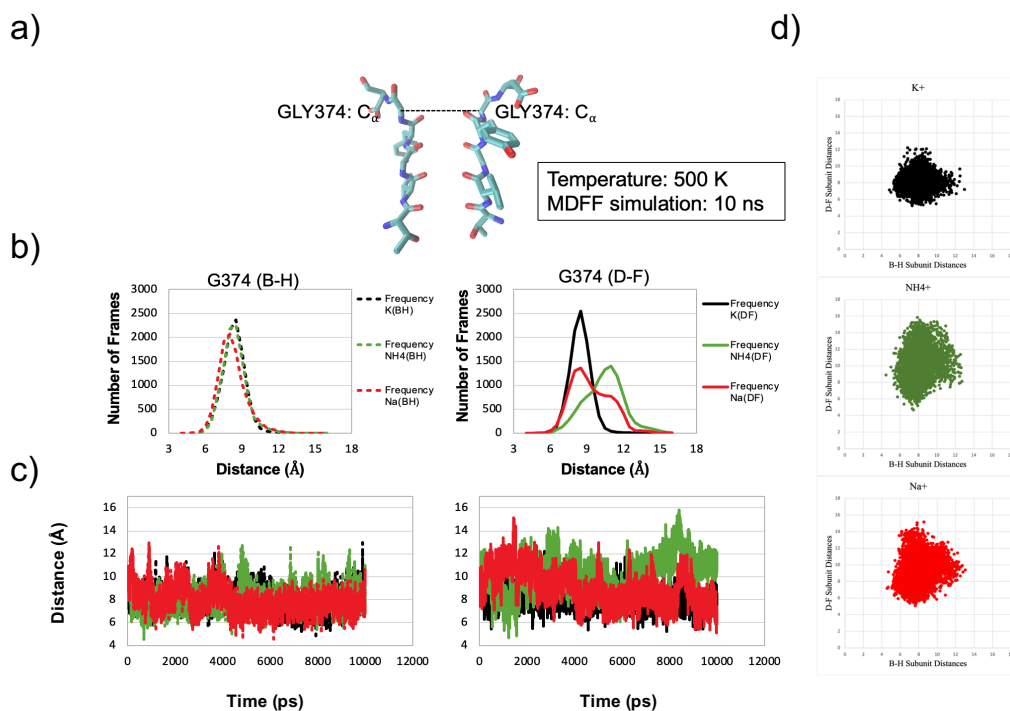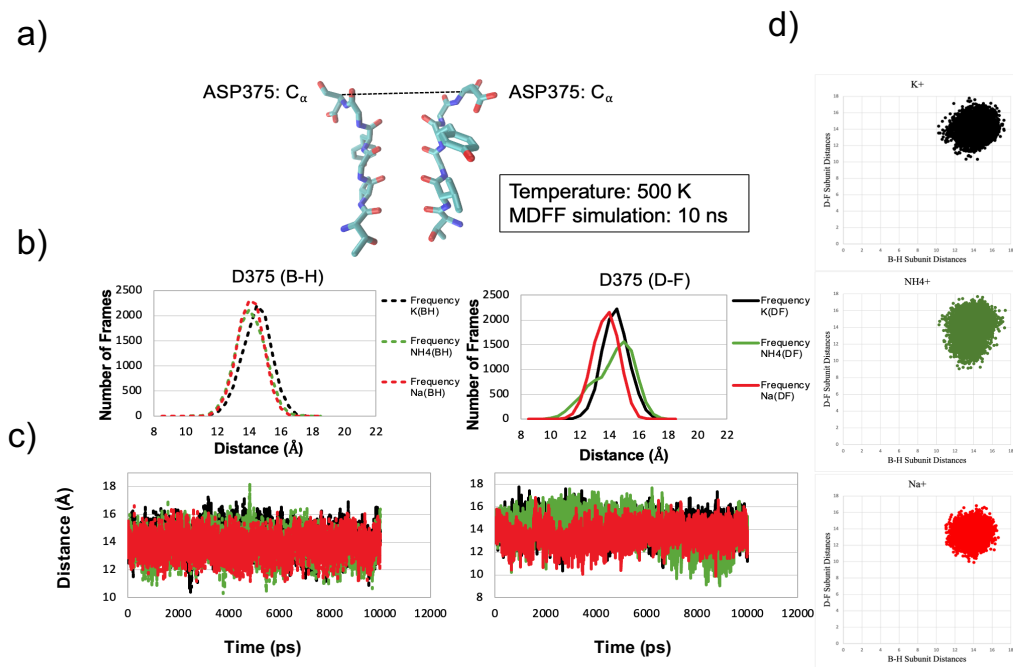
**Figure 2.16-2.21 (continued):** Selectivity filter (TVGYGD) Cα-Cα distance analysis between B-H and D-F opposing subunits throughout the 10 ns MDFF simulation of WT Kv1.2-2.1 in high K+ (black), low K+ high NH₄+ (green), and low K+ high Na+ (red) conditions. Scaling factor ξ = 0.3 kcal/mol and the harmonic restraint constant $k_\mu$ = 200 kcal/mol/A² were used to ensure that the models could explore the density map fully without leaving the map. a) Selectivity filter with the distance between a pair of Cα-Cα (either B-H or D-F) being measured for each residue in the TVGYGD throughout the MDFF simulation. b) Number of frames from the 10 ns MDFF simulation vs distance (in Å) between Cα-Cα for either B-H or D-F subunit using 0.5 Å binning size. c) Raw data Cα-Cα distance for B-H or D-F subunit during the 10 ns MDFF simulation. 10k frames are generated from the simulation, where each frame is a picosecond. d) 2D plot of B-H vs D-F Cα-Cα distance for each frame during the MDFF simulation for each residue.

## Pore domain profile using HOLE program

We used the program HOLE [26] to calculate the profile of the pore radius along the z-axis (axis of the selectivity filter and the intracellular gate) for all three ionic conditions. The high K+ structure, as indicated by the red color in the profile, has a narrow selectivity filter between ~0.6-1 Å. Only potassium ions can occupy the selectivity filter (**Figure 2.22a**). The low K+
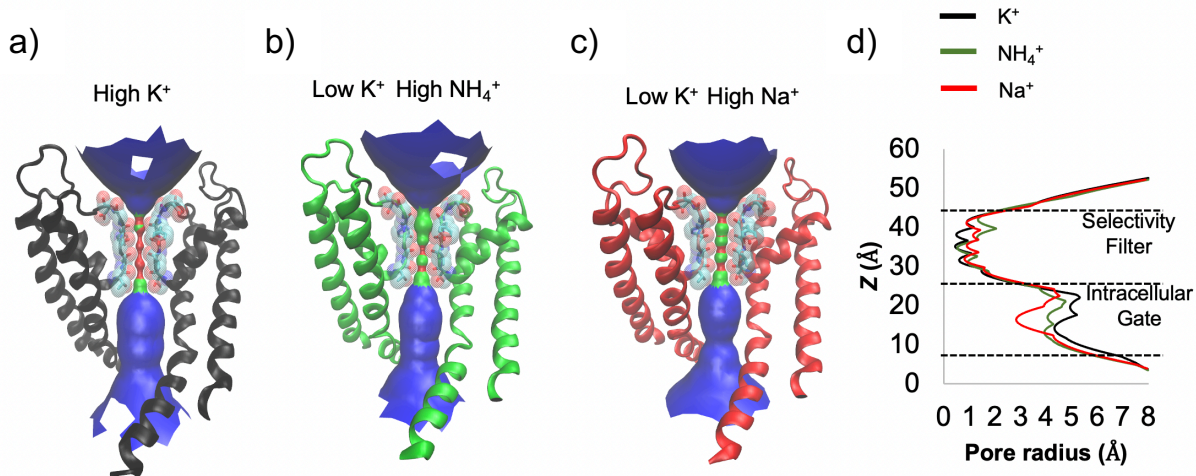


**Figure 2.22:** Pore radius profile of WT Kv1.2-2.1 in high K+ (black), high NH₄+ (green), and high Na+ (red) from C1 symmetry density map using HOLE reveals a wider pore radius in the outer mouth region of the selectivity filter in low K+ conditions compared to the high K+. The subtle differences in the pore radius between high K+ (a) and low K+ (b, c) modeled from C1 symmetry density maps are calculated using HOLE [21]. The red color in the profile represents a pore radius of below 1.15 Å, which is the minimum radius to accommodate a water molecule. The blue color in the profile represents a pore radius of above 2.3 Å, which is the minimum radius to fit two water molecules in side by side the surface. The green color in the profile represents the intermediate zone with a pore radius between 1.15 -2.3 Å to fit just one water molecule. The high K+ structure shows a narrow ion permeation pathway in the selectivity filter at ~1 Å. In the low K+ structures, there is a widening of the outer mouth of the selectivity filter as well as a narrowing of the intracellular gate (especially in high Na+ condition). These differences are quantitatively depicted in the pore radius vs distance graph (d). The regions indicated divides where the selectivity filter and the intracellular gate are. The high NH₄+ and Na+ structures show a ~1 Å and ~0.6 Å widening of the outer mouth in the selectivity filter relative to the high K+ structure, respectively. This is also where the G374 is located. High Na+ structure also exhibits a ~2 Å narrowing in the intracellular gate compared to the high K+ structure.

structures, on the other hand, exhibit an overall wider selectivity filter allowing a water molecule to occupy the filter, as indicated by the green color in the profile (**Figure 2.22b, c**). Furthermore, there is a widening in the outer mouth of the selectivity filter. The high $NH_4^+$ and $Na^+$ structures show a dilation at G374 residue by ~1 Å and ~0.6 Å compared to the high $K^+$ condition, respectively (**Figure 2.22d**). This is consistent with the result observed in the MDFF simulations, where the opposite subunit analysis displayed a dilation in the G374 residue in low $K^+$ conditions through the simulation trajectories. The pore radius profile also shows that the high $Na^+$ structure has a narrower intracellular gate compared to the high $K^+$ condition by ~2 Å (**Figure 2.22d**). This observation is consistent with what we observed from the cryo-EM density where the I398 and V402 conformational change in the low $K^+$ high $Na^+$ conditions narrow the intracellular gate (**Figure 2.15b, c**). These factors could contribute to the subtle conformational changes that is responsible for C-type inactivated state in the WT Kv chimera.

## Discussion

The objective of this chapter was to characterize the function and structure of the Kv1.2-2.1 chimera in a low $K^+$ environment to capture the C-type inactivated state in eukaryotic voltage-gated potassium channel. This basic idea is inspired from previous results on KcsA, where the low $K^+$ environment captured the constricted selectivity filter widely believed to correspond to the C-type inactivated state [3, 27, 28]. Functionally, we saw a clear indication of reduction of current through Kv1.2-2.1 WT from inactivation in low $K^+$ environment using the cut-open oocyte voltage clamp technique (COVG). Structurally, we presented structures of Kv1.2-2.1 in C4 and C1 symmetry in high $K^+$, low $K^+$ high $NH_4^+$, and low $K^+$ high $Na^+$ conditions with resolutions in the range of 2.93 – 3.65 Å. The high $K^+$ structure was determined in DDM/CHS environment with lipids added (POPC: E: G at 3:1:1), while the low $K^+$ structures were determined in nanodisc environments.

In the original X-ray structure of Kv1.2-2.1 at 2.4 Å resolution [1], Long et al. expected to observe the C-type inactivated state at 0 mV in a membrane-like environment with detergent mixed with lipids. Yet, the structure revealed a channel with an opened intracellular gate and a conductive selectivity filter. Matthies et al., also note that there is very little difference in structure between the X-ray structure of Kv1.2-2.1 in detergent with lipids and the cryo-EM structure of Kv1.2-2.1 in nanodisc [11]. In other words, the Kv1.2-2.1 behaves structurally similar in nanodisc and detergent mixed with lipids and is consistently different from functional results which suggests a C-type inactivated state at 0 mV.

In our case, we observed very slight differences in the selectivity filter across high $K^+$ and low $K^+$ environments with possibility of asymmetric pinching at G372 for all conditions and asymmetric dilation at G374 positions for low $K^+$ conditions through MD simulations. This slight difference in structure also revealed a possibility of more water to occupy the selectivity filter in low $K^+$ environments, which could in turn affect the rate of conduction. At present, however, we do not know how much this could affect ion conduction. We also observed, in low $K^+$ conditions, weakening of the hydrogen bond between D375 in the P loop and W362 in the pore helix, which may allow D375 to adopt multiple rotameric conformations. Functionally, this hydrogen bond has been shown to be critical for stabilizing the conducting state [29]. Therefore, this could constitute an additional contribution to a structurally subtle mechanism of inactivation as proposed. At the current resolution, the structure that we obtained could also explain the hydrogen bond being intact. Therefore, we cannot make a strong case for this hydrogen bond being broken in the low $K^+$ conditions. We also observed a narrowing at the intracellular gate due to a conformational change in the I398 and V402 in the low $K^+$ high $Na^+$ condition. This could contribute at least partially to the loss of conduction observed for this condition functionally.

While C-type inactivation has been studied extensively in voltage-gated potassium channels, the structural basis of this crucial mechanism remains quite controversial. Mutations

in and near the external pore and the S6 helix have either been functionally or structurally

proposed to have captured the C-type inactivated state [12, 22, 30-34]. Some propose a much

more subtle C-type inactivated state [11, 12] described by slight modulations in the selectivity

filter, while others propose that the C-type inactivation undergoes a much larger conformational

changes [5, 31] described by a dilation of the selectivity filter due to Y373 side chain movement.

While the recent W434F in *Shaker* and W362F in Kv1.2-2.1 structures provide significant

addition to our structural repertoire of Kv channels [5, 31], whether the structure of this mutant is

representative of the native C-type inactivated state of the selectivity filter in the wild-type

channel is unclear. Firstly, the *Shaker-IR* WT and W434F as well as Kv1.2-2.1 WT and W362F

should all be inactivated at 0 mV [2, 22], yet the WT and the mutant structures are drastically

different [5, 31]. Secondly, whether the dilated filter of W434F *Shaker-IR* and W362F Kv1.2-2.1

structures truly non-conductive or not remain to be seen.

Our model of C-type inactivation supports the idea that the inactivated state is described

by slight modulations in the selectivity filter on the scale of <2 Å. This would require less energy

to move from inactivated to recovered state more readily. As mentioned previously, however,

the resolution of our cryo-EM structure limits the extent to which we could unambiguously

identify the structural changes that occur with C-type inactivation. Nonetheless, we were able to

capture a glimpse of the subtlety using MDFF simulations and model fitting into our density

maps in the low $K^+$ conditions. Given all of the structural and functional evidence for C-type

inactivation, from KcsA, Kv1.2, Kv1.2-2.1 chimera to *Shaker*, there may be multiple structural

mechanisms of C-type inactivation in the Kv1.2-2.1. Therefore, we cannot conclude definitely

about a structural model of the C-type inactivated state. However, our approach for low $K^+$ may

mimic the natural environment for voltage-gated potassium channels for entering the C-type

inactivated state without the need for mutations.

## Materials and Methods:

**Materials**

 *Xenopus laevis* oocytes were provided by the lab of Francisco Bezanilla. The oocytes were harvested from ovaries of the toads in accordance with the experimental protocols approved by the University of Chicago Animal Care and Use Committee. The cut-open voltage clamp rig was set up in the Perozo lab according to Stefani and Bezanilla, 1998 [20]. For high $K^+$ condition, the external solution contained 12 mM KCl, 108 mM N-methyl-D-glucamine (NMDG), 10 mM HEPES, and 2 mM $CaCl_2$ set to pH 7.5 with 2-(*N*-morpholino)ethanesulfonic acid (MES), while the internal solution contained 120 mM KCl, 10 mM HEPES, and 2 mM EGTA set to pH 7.5 with KOH. For high $NH_4^+$ low $K^+$ condition, the external solution contained 12 mM $NH_4Cl$, 1 mM KCl, 108 mM NMDG, 10 mM HEPES, and 2 mM $CaCl_2$ set to pH 7.5 with MES while the internal solution contained 120 mM $NH_4Cl$, 10 mM HEPES, and 2 mM EGTA set to pH 7.5 with $NH_4OH$. Lastly, for high $Na^+$ low $K^+$ condition, the external solution contained 12 mM NaCl, 1 mM KCl, 108 mM NMDG, 10 mM HEPES, and 2 mM $CaCl_2$ set to pH 7.5 with MES while the internal solution contained 120 mM NaCl, 10 mM HEPES, and 2 mM EGTA set to pH 7.5 with NaOH.

 Detergents were purchased from Anatrace, lipids from Avanti Polar Lipids, Superose 6 Increase 10/300 column from GE Healthcare, anti-His-tag antibodies from GenScript, TALON cobalt resin from Clontech, Biobeads SM-2 resin from Bio-Rad Laboratories, and Zeocin from Invitrogen Life Technologies. Other reagents were purchased from Sigma, ThermoFisher Scientific, and GoldBio. Yeast cells were pulverized in Retsch PM 100 planetary ball mill in 125 mL grinding jars. Ultracentrifugation was performed on Beckman Coulter L-90K centrifuge using a Ti-45 rotor. Culture media for *Pichia pastoris* were prepared as described in the '*Pichia* Expression Kit' manual (Invitrogen Life Technologies). cDNA of the rat Kv1.2-2.1 chimera α subunit combined with a rat β2.1 gene (residues 36–367) in the pPICZ-C plasmid was a gift

from R. MacKinnon (Rockefeller University) [1]. Any mutations on the Kv1.2-2.1 were done on this background.

The lysis buffer consisted of 150 mM KCl, 50 mM Tris-HCl titrated to pH 7.5, 2 mM Tris(2-carboxyethyl) phosphine (TCEP) titrated to pH 7.5 with NaOH, 5 mM β-mercaptoethanol (β-ME), 0.1 mg/mL DNAseI, 0.1 mg/mL pepstatin A, 1 µg/mL aprotinin, 1 µg/mL leupeptin, 0.1 mg/mL soybean trypsin inhibitor, 1 mM benzamidine, 2 mM PMSF.

The column wash/elution buffer consisted of 150 mM KCl, 50 mM Tris-HCl titrated to pH 7.5, 2 mM TCEP, 5 mM β-ME, 5 mM dodecyl-maltoside/Cholesteryl Hemisuccinate Tris Salt (DDM/CHS), 0.025 mg/mL lipid mixture (3:1:1 ratio) of 1-palmitoyl-2-oleoyl-*sn*-glycero-3-phosphocholine (POPC), 1-palmitoyl-2-oleoyl-*sn*-glycero-3-phosphoethanolamine (POPE) and 1-palmitoyl-2-oleoyl-*sn*-glycero-3-[phospho-rac-(1-glycerol)] (POPG).

The gel-filtration buffer consisted of 150 mM salt, 20 mM Tris-HCl, 2 mM TCEP, 2 mM DTT, 1 mM DDM/CHS and 0.025 mg/mL of the lipid mixture (3:1:1 POPC/POPE/POPG). Depending on the condition for the purification, the salt used were either KCl, $NH_4Cl$, or NaCl with final pH adjusted to 7.5 using KOH, $NH_4OH$, and NaOH, respectively.

The nanodisc gel-filtration buffer consisted of 150 mM salt, 20 mM Tris-HCl, 2 mM TCEP, and 2 mM DTT. Depending on the conditions for the purification, the salt used were either KCl, $NH_4Cl$, or NaCl with final pH adjusted to 7.5 using KOH, $NH_4OH$, and NaOH, respectively.

To prepare a 10% stock solution of DDM/CHS (~200 mM), 5g of dry DDM was added to a 50 mL falcon tube containing 40 mL of 200 mM Tris pH 8.0 and was rotated until the detergent goes into the solution. Then 1g of CHS was added to the detergent solution and the resulting mixture in the falcon tube was sonicated continuously until solution became hot to the touch and translucent. Volume was brought up to 50 mL with water and the tube was rotated at RT until solution became transparent. The stock solution was stored in 4 °C.

To prepare the lipid mixture of POPC/E/G for buffer preparation, the lipids in chloroform were first mixed at the 3:1:1 ratio in a round-bottom glass flask, and then rotary evaporator or stream of nitrogen gas was used to remove chloroform. The dried lipid mixture was stored in a desiccator for at least 24 hr protected from light. Dry lipids were resuspended in 1% DDM/CHS solution and sonicated until the mixture was transparent. Then the detergent-lipid mixture was added to the buffers according to the protocol.

For nanodisc reconstitution of the Kv1.2-2.1 from detergent, four ingredients are necessary: fresh protein sample in detergent in correct concentration, lipid mixture, MSP, and Biobeads. MSP1E3D1 was purified as previously described [35, 36] at 225 mM concentration. Lipid mixture of 3:1:1 POPC/E/G was dried in the same way as described above and then resuspended in water thoroughly at a concentration of 20 mg/mL. The formed vesicles were sonicated until the solution became transparent. DDM was added to a concentration of 33 mM and lipid mixture concentration of 11.5 mM. This was divided into small aliquots and was kept frozen at -80 °C until further use. Biobeads SM-2 resin was washed with methanol and thoroughly rinsed with water. They were stored in water at 0.5 g/mL concentration.

**Oocyte preparation for COVG**

*Xenopus laevis* oocytes were harvested via incision from the ovary of the toad anesthetized with a tricaine solution, in accordance with the experimental protocols approved by the University of Chicago Animal Care and Use Committee. Following the collagenase digestion of the follicular membrane, oocytes were stored at 18°C in standard oocyte solution (SOS) containing 96 mM NaCl, 2 mM KCl, 1.8 mM $CaCl_2$, 1 mM $MgCl_2$, and 10 mM HEPES, pH 7.4, with 10 µg/mL gentamicin. Oocytes were typically injected a day after digestion.

**mRNA preparation of Kv1.2-2.1 for COVG recording**

To express Kv1.2-2.1 in *X. laevis*, we used the pMAX vector with a T7 promoter containing Kv1.2, which was a gift from Anthony Lewis (University of Portsmouth). We first created the empty pMAX vector by removing the Kv1.2 gene and then inserted the Kv1.2-2.1 alpha subunit as the coding sequence into the empty pMAX vector. The DNA was prepared using the NucleoSpin Plasmid kit (Macherey-Nagel) and was linearized with PmeI (New England Biolabs). Linearized cDNA was transcribed into mRNA with mMESSAGE mMACHINE T7 kit (Life Technologies). Oocytes were injected with 50 ng of mRNA using a Drummond nanoinjector and were incubated at 18 $^{\circ}$C in the standard oocyte solution (SOS) with 10 µg/mL gentamicin. COVG recordings were made 24-48 hours after injection to allow for proper expression and trafficking of Kv1.2-2.1 into the oocyte membrane.


**Cut-open Vaseline-Gap (COVG) Voltage Clamp**

The cut-open oocyte voltage clamp technique was used to allow for fast exchange of internal ionic solutions for low K$^+$ conditions while maintaining high clamp fidelity and low noise. All recordings were performed at ~20 °C. The SB6711 digital signal processor-based board with an A4D4 board was controlled by Gpatch, the in-house software and GUI. Oocytes were held under voltage clamp using the Dagan CA-1B amplifier. Current was filtered at 5 kHz.

The microelectrodes were pulled from a Flaming-Brown micropipette puller (Model P-87; Sutter Instruments) and were filled with 3M CsCl$_2$ with a resistance of ~0.4-0.6 MΩ. Low resistance access to the oocyte interior was obtained by permeabilizing the oocyte with 0.1% saponin carried by the internal solution. Recordings were taken with holding potential at -80 mV, a prepulse of -80 mV for 100 ms, variable voltages from -80 mV to +60 mV at 10 mV increments for 1 sec, and a return to -80 mV for 250 ms.

**Transformation, Expression, and Purification**

The pPICZ-C plasmid with both rKv1.2-2.1 and rβ2.1 was amplified, linearized with PmeI, and purified by phenol-chloroform extraction. For the extraction, we followed the protocol from Pacific Biosciences: https://www.pacb.com/wp-content/uploads/2015/09/SharedProtocol-Extracting-DNA-usinig-Phenol-Chloroform.pdf. About 25-40 μg of the linearized-purified DNA was transformed into yeast *Pichia* pastoris SMD1168 *his4* strain via electroporation. The parameters used were 2500 V, 25 μF, and 400 Ω, with time constant ranging from 6-9 msec. After electroporation, the transformed cells were allowed to recover O/N in YPD media with shaking. Then *P. pastoris* clones with successful cDNA integration into the yeast genome were selected on agar plates containing yeast extract, peptone, dextrose, sorbitol (YPDS) in four different Zeocin concentrations: 0.1, 0.5, 1 and 1.5 mg/mL. Selected colonies were grown in small-scale liquid culture containing 0.1 mg/mL zeocin and were screened for protein expression with anti-His-tag western blotting.

The clone of *P.* pastoris with the most expression in the small-scale was stored as a glycerol stock to be used for large-scale growth and expression. All yeast cells were grown in baffled flasks with a 1:3 medium/air ratio in a 30 °C shaker (250 r.p.m) incubator. The selected clone for large-scale expression was inoculated into 30 mL of buffered minimal glycerol (BMG) media containing 0.1 mg/mL zeocin and was grown for 36 hr. The culture was diluted with 4 L of BMG media to an optical density (OD) of ~0.2, then grown for 24 hr until OD reached 3-5. The yeast cells were then collected by centrifugation at ~5000g for 10 min at RT, resuspended (OD of ~1.5-2) and grown in 4 L of buffered minimal methanol (BMM) media. After 24 hr, an additional dose of 0.5% methanol was added to the media to sustain protein induction. After another 24 hr (for a total of 48 hr induction period), the culture was harvested by centrifugation at 5000g for 10 min at 4 °C. Pellet was made into a thin noodle via running it through a 60 mL syringe as it was being immediately frozen in liquid nitrogen. Then the frozen noodles were crushed and stored at -80 °C.

For purification, frozen yeast cell noodles were further pulverized with a Retsch PM100 planetary ball mill in 125 mL grinding jar via 2 min of milling at 400 r.p.m. followed by 1 min of reverse rotation repeated eight times with a 3 min of liquid-nitrogen cooling in between. The resulting pulverized cell powder could be stored in -80 °C until further use. To further purification, the cell powder was thawed at RT in lysis buffer (6 mL/g) for 3 hr. The pH of the solution was checked every hour and KOH solution was added to keep the pH at ~7.5. All subsequent steps were carried out at 4 °C for protein stability. To isolate the cell membranes from the rest of the pulverized cell matter, the thawed cell lysate was centrifuged at 2000g for 5 min. The supernatant was carefully collected and was ultracentrifuged at 100,000g for 75 min (Beckman, Ti 45 rotor). The pellet containing cell membranes was resuspended in lysis buffer (4 mL/g) and homogenized on ice with a Dounce tissue homogenizer. 40% of filter sterilized glycerol was added to the membrane lysate and flash frozen in liquid nitrogen and stored in -80°C for further use.

The homogenized membrane lysate was thawed in additional lysis buffer at 1:1 volume. The sample was extracted in the detergent 1% DDM/CHS via stirring for 3 hr in a cold room (4 °C) and then centrifuged at 80,000 for 60 min. The supernatant was mixed with TALON cobalt resin pre-equilibrated with lysis buffer with 0.25% DDM/CHS. The mixture was allowed to rotate for 2 hr in 4 °C. The mixture was then loaded onto a column until only resin bound with protein remained. The column was washed with wash/elution buffer with 30mM imidazole (20x bed volume) and eluted with wash/elution buffer with 300mM imidazole (5x bed volume). The elution was concentrated to 0.5 mL with a Millipore Amicon Ultra 100K centrifugal filter unit and further purified on a Superose 6 Increase (10/300) size-exclusion column (SEC) pre-equilibrated with gel-filtration buffer. Gel-filtration fractions at ~10-11 mL identified to contain the tetrameric Kv1.2-2.1 complexed with the rβ2.1 were pooled and concentrated to ~5-6 mg/mL with a Millipore Amicon Ultra 100K filter unit. The concentrated sample was diluted with a buffer that had the composition of the gel-filtration buffer without the detergent or lipid and was

reconcentrated to 5-6 mg/mL. The process was repeated until DDM/CHS concentration reached ~10mM while protein concentration was at 5-6mg/mL.

For detergent-lipid conditions, the 5-6 mg/mL sample was immediately loaded onto cryo-EM grids for freezing via vitreous ice formation. We will describe this process in more detail later below. For samples reconstituted into nanodiscs (ND), the sample was further concentrated to ~9 mg/mL (0.023mM). Fresh sample (within 1-2 hr of purification) was mixed with the lipid mixture with DDM and incubated to 20 min on ice. Then MSP1E3D1 was added to the mixture and was incubated for 10 min on ice. The reconstitution concentration of the Kv1.2-2.1, MSP, and lipid mixture was 3 μM, 30 μM, and 1.2 mM, respectively, for a ratio of 1:10:400. Precise protein concentrations needed for the proper reconstitution were calculated by measuring the absorbance at 20 nm using molar extinction coefficients of 454,720 $M^{-1}cm^{-1}$ and 26,930 $M^{-1}cm^{-1}$ for the Kv1.2-2.1 and MSP1E3D1, respectively. Reconstitution mixture was then moved to a new tube containing dried, activated Biobeads and was rotated overnight at 4 °C. Then the sample was mixed with fresh Biobeads while nanodisc gel-filtration buffer was added to the old Biobeads at equal volume to the sample. After 1.5 hr of additional rotation in 4 °C, the two samples were pooled together. Biobeads were separated by filter through a 0.22 μm membrane and the filtrate was injected into Superose 6 Increase (10/300) SEC pre-equilibrated with the nanodisc gel-filtration buffer. Gel-filtration fractions at ~11-12 mL identified to contain the tetrameric channel reconstituted in nanodisc were pooled and concentrated to ~1-2 mg/mL with a Millipore Amicon Ultra 100K filter unit. The resulting sample was used to freezing cryo-EM grids via vitreous ice formation. The summary of the transformation, selection, expression. and purification workflow is summarized in **Figure 2.5**.

**Cryo-EM Sample Preparation**

Quantifoil Cu 200 and 300 R1.2/1.3 holey carbon grids (Quantifoil Micro Tools GmbH, Großlöbichau, Germany) were used for screening and data collection. The grids were plasma

cleaned for 30 seconds in a Solarus Plasma Cleaner (Gatan) and were frozen in liquid ethane that was cooled with liquid nitrogen using the Vitrobot Mark IV (ThermoFisher) with the following parameters: sample volume of 3.5 µl, blot time of 3.5 sec, blot force of 3, temperature of 22°C, and humidity of 100%. Around 5-6 mg/mL for detergent and 1-1.5 mg/mL for nanodisc samples were optimal to see enough particles on micrographs without aggregation.

## Screening and Data Collection

Grids were screened on a 200 kV Talos side-entry microscope (FEI) equipped with the K2 summit direct detector (Gatan) using a Gatan 626 single-tilt holder at the University of Chicago. Replicate grids from the same preparation were either shipped to Stanford-SLAC (Stanford Linear Accelerator Center) Cryo-EM Center ($S^2C^2$) for data collection (for low $K^+$ samples) or were used for data collection directly at the University of Chicago Advanced Electron Microscopy Facility (for high $K^+$ sample).

For data collection, the grids were imaged on a Titan Krios microscope (FEI) from either the University of Chicago Advanced Electron Microscopy Facility or Stanford-SLAC (Stanford Linear Accelerator Center) Cryo-EM Center ($S^2C^2$). The data collection was operated at 300 kV, aligned for parallel illumination. Data collection images were acquired with a Gatan K3 Camera and a BioQuantum Energy Filter operated in super-resolution mode. Calibrated physical pixel size of 1.08 Å and a super-resolution pixel size of 0.54 Å with a defocus range between -1.5 and -2.5 µm were used to collect images with the Latitude S software (Gatan Inc., Pleasanton, CA). A dose of 1.25 $e^-/A^2$/frame per frame for 40 frames for a total of 50 $e^-/A^2$ was used. One image per hole was collected for all samples. Total exposure time was 4.0 sec, with frame duration of 0.1 sec/frame. The following number of images were collected for each sample: 5,800 images for high $K^+$ Kv1.2-2.1 in DDM/CHS, 12,992 images for low $K^+$ high $NH_4^+$ Kv1.2-2.1 in ND, and 13,356 images for low $K^+$ high $Na^+$ Kv1.2-2.1 in ND.

## Data Processing

The images from each dataset were motion-corrected using MotionCor2, dose-weighted and CTF-estimated using CTFFIND4, and further processed using RELION 3 [37-41]. Automated particle picking was performed using crYOLO [21]. The particle-picked images were imported into RELION 3 to extract the particles and to generate 2D classifications. For all three structures, three rounds of 2D classification were performed to remove obvious artefacts before proceeding to 3D construction of the density map.

For high $K^+$ structure, ~704k particles were picked using crYOLO, which were subjected to 2D classification. ~384k particles were selected from good classes, and ~30k of these particles were used to generate an initial model with C1 symmetry imposed. After 3D classification, ~198k particles in C4 and ~193k particles in C1 were subjected to auto-refinement, yielding a 3.27 Å and a 4.09 Å nominal resolution map in C4 and C1 symmetry, respectively. Focused refinement on the entire Kv1.2-2.1 protein and subsequently only the transmembrane (TM) region gave a reconstruction with improved map quality supporting confident building of the TM regions. Post-processing of the focused TM map was performed in RELION 3 using the 300 kV K3 detector star file and was calculated a masked nominal resolution of 3.0 Å for C4 and 3.57 Å for C1 symmetry by the 0.143 FSC criterion [42-44].

For low $K^+$ high $NH_4^+$ structure, ~2.1M particles were picked using crYOLO which were subjected to 2D classification. ~535k particles were selected from good classes, and 3D construction in C1 symmetry was made using the post-processed map from the high $K^+$ condition as a reference. ~127k particles were subjected to auto-refinement in C4 and C1 symmetry, yielding a 3.2 Å and a 4.3 Å nominal resolution map in C4 and C1 symmetry, respectively. Post-processing of the focused TM map was performed in RELION 3 using the 300 kV K3 detector star file and was calculated a masked nominal resolution of 2.9 Å for C4 and 3.61 Å for C1 symmetry by the 0.143 FSC criterion [42-44].

For low $K^+$ high $Na^+$ structure, ~3.2M particles were picked using crYOLO which were subjected to 2D classification. ~464k particles were selected from good classes, and 3D construction in C1 symmetry was made using the post-processed map from the high $K^+$ condition as a reference. ~186k particles were subjected to auto-refinement, yielding a 3.53 Å and 3.61 Å nominal resolution map in C4 and C1 symmetry, respectively. Post-processing of the focused TM map was performed in RELION 3 using the 300 kV K3 detector star file and was calculated a masked nominal resolution of 3.11 Å for C4 and 3.65 Å for C1 symmetry by the 0.143 FSC criterion [42-44].

C1 symmetry was imposed for all three ionic conditions to observe each tetrameric subunit in their native conformation as that could elucidate the overall conformation in the selectivity filter. Local resolution was calculated by RELION's local-resolution, and particle orientation distribution calculated by RELION 3 [37, 41].


**Model Fitting**

A tetrameric model for the Kv chimera in each ionic condition in either C4 or C1 symmetry was produced from an X-ray structure (PDB ID: 2r9r) and used for rigid body fitting in UCSF Chimera [45]. Because of the slight shift/rotation in each density between the TM and cytosolic domains relative to the 2r9r structure, however, we first created two separate PDB files for TM and cytosolic domains. Then we fit each PDB file into each density map before performing initial flexible fitting in COOT [46] by manually surveying the entire peptide chain of a single chain of the α and β subunit before applying the changes to other subunits. After a rough fit using COOT, we used cryo-fit2 [47] from Phenix [48] to fit the model into the density even better. Finally, we performed real space refinement using Phenix. Models were subjected to an all-atom structure validation using MolProbity (Table 1-1) [49].

## Molecular Dynamics Simulations

The MDFF (Molecular Dynamics Flexible Fitting) simulations were performed using NAMD

version 2.14 [50], with the CHARMM27 force field [51, 52] in vacuo using a dielectric constant of

80 [25]. A multiple time-stepping integration scheme is used, calculating bonded interactions

every 1 fs and nonbonded interactions every 2 fs; a cutoff distance of 10 Å is used for the

nonbonded interactions. Temperature was kept at 500 K through the simulation using a

Langevin thermostat [53] coupled to all heavy atoms with a damping coefficient of 5 ps$^{-1}$.

$\xi$, the scaling factor for map weight, of 0.3 kcal/mol and $k_\mu$ = 200 kcal mol$^{-1}$ Å$^{-2}$ for the harmonic

restraints were used in a 10 ns simulation to allow the protein models to fully explore the density

map while still being fully contained within the map. Throughout the simulation, the VSD and the

intracellular gate were restrained. Only residues 360-376 (pore helix and selectivity filter) were

allowed to move during the simulation. VMD program [54] was used to analyze and render the

MDFF data. Profiles of pore radius were calculated with HOLE [26].


## Figure preparation

Structural figures were prepared with Chimera [45] and VMD [54].

# References:

1.	Long, S.B., et al., *Atomic structure of a voltage-dependent K+ channel in a lipid membrane-like environment.* Nature, 2007. **450**(7168): p. 376-82.
2.	Hoshi, T., W.N. Zagotta, and R.W. Aldrich, *Two types of inactivation in Shaker K+ channels: effects of alterations in the carboxy-terminal region.* Neuron, 1991. **7**(4): p. 547-56.
3.	Zhou, Y., et al., *Chemistry of ion coordination and hydration revealed by a K+ channel-Fab complex at 2.0 A resolution.* Nature, 2001. **414**(6859): p. 43-8.
4.	Kurata, H.T. and D. Fedida, *A structural interpretation of voltage-gated potassium channel inactivation.* Prog Biophys Mol Biol, 2006. **92**(2): p. 185-208.
5.	Tan, X.F., et al., *Structure of the Shaker Kv channel and mechanism of slow C-type inactivation.* Sci Adv, 2022. **8**(11): p. eabm7814.
6.	Bean, B.P., *The action potential in mammalian central neurons.* Nat Rev Neurosci, 2007. **8**(6): p. 451-65.
7.	Bekkers, J.M. and A.J. Delaney, *Modulation of excitability by alpha-dendrotoxin-sensitive potassium channels in neocortical pyramidal neurons.* J Neurosci, 2001. **21**(17): p. 6553-60.
8.	Guan, D., et al., *Functional roles of Kv1 channels in neocortical pyramidal neurons.* J Neurophysiol, 2007. **97**(3): p. 1931-40.
9.	Long, S.B., E.B. Campbell, and R. Mackinnon, *Crystal structure of a mammalian voltage-dependent Shaker family K+ channel.* Science, 2005. **309**(5736): p. 897-903.
10.	Tao, X. and R. MacKinnon, *Functional analysis of Kv1.2 and paddle chimera Kv channels in planar lipid bilayers.* J Mol Biol, 2008. **382**(1): p. 24-33.
11.	Matthies, D., et al., *Single-particle cryo-EM structure of a voltage-activated potassium channel in lipid nanodiscs.* Elife, 2018. **7**.
12.	Pau, V., et al., *Crystal structure of an inactivated mutant mammalian voltage-gated K(+) channel.* Nat Struct Mol Biol, 2017. **24**(10): p. 857-865.
13.	Miller, C., R. Latorre, and I. Reisin, *Coupling of voltage-dependent gating and Ba++ block in the high-conductance, Ca++-activated K+ channel.* J Gen Physiol, 1987. **90**(3): p. 427-49.
14.	Swenson, R.P., Jr. and C.M. Armstrong, *K+ channels close more slowly in the presence of external K+ and Rb+.* Nature, 1981. **291**(5814): p. 427-9.
15.	Barnard, E.A., R. Miledi, and K. Sumikawa, *Translation of exogenous messenger RNA coding for nicotinic acetylcholine receptors produces functional receptors in Xenopus oocytes.* Proc R Soc Lond B Biol Sci, 1982. **215**(1199): p. 241-6.
16.	Gundersen, C.B., R. Miledi, and I. Parker, *Voltage-operated channels induced by foreign messenger RNA in Xenopus oocytes.* Proc R Soc Lond B Biol Sci, 1983. **220**(1218): p. 131-40.
17.	Gurdon, J.B., et al., *Use of frog eggs and oocytes for the study of messenger RNA and its translation in living cells.* Nature, 1971. **233**(5316): p. 177-82.
18.	Miledi, R., I. Parker, and K. Sumikawa, *Recording of single gamma-aminobutyrate- and acetylcholine-activated receptor channels translated by exogenous mRNA in Xenopus oocytes.* Proc R Soc Lond B Biol Sci, 1983. **218**(1213): p. 481-4.
19.	Timpe, L.C., et al., *Expression of functional potassium channels from Shaker cDNA in Xenopus oocytes.* Nature, 1988. **331**(6152): p. 143-5.
20.	Stefani, E. and F. Bezanilla, *Cut-open oocyte voltage-clamp technique.* Methods Enzymol, 1998. **293**: p. 300-18.
21.	Wagner, T., et al., *SPHIRE-crYOLO is a fast and accurate fully automated particle picker for cryo-EM.* Commun Biol, 2019. **2**: p. 218.
22.	Perozo, E., et al., *Gating currents from a nonconducting mutant reveal open-closed conformations in Shaker K+ channels.* Neuron, 1993. **11**(2): p. 353-8.
23.	Suarez-Delgado, E., et al., *KV1.2 channels inactivate through a mechanism similar to C-type inactivation.* J Gen Physiol, 2020. **152**(6).
24.	Jeffrey, G.A., *An introduction to hydrogen bonding.* Topics in physical chemistry. 1997, New York: Oxford University Press. vii, 303 p.
25.	Trabuco, L.G., et al., *Molecular dynamics flexible fitting: A practical guide to combine cryo-electron microscopy and X-ray crystallography.* Methods, 2009. **49**(2): p. 174-180.
26.	Smart, O.S., et al., *HOLE: a program for the analysis of the pore dimensions of ion channel structural models.* J Mol Graph, 1996. **14**(6): p. 354-60, 376.

27.    Cuello, L.G., et al., *Structural mechanism of C-type inactivation in K(+) channels.* Nature, 2010. **466**(7303): p. 203-8.

28.    Doyle, D.A., et al., *The structure of the potassium channel: Molecular basis of K+ conduction and selectivity.* Science, 1998. **280**(5360): p. 69-77.

29.    Pless, S.A., et al., *Hydrogen bonds as molecular timers for slow inactivation in voltage-gated potassium channels.* Elife, 2013. **2**: p. e01289.

30.    Lopez-Barneo, J., et al., *Effects of external cations and mutations in the pore region on C-type inactivation of Shaker potassium channels.* Recept Channels, 1993. **1**(1): p. 61-71.

31.    Reddi, R., et al., *Structural basis for C-type inactivation in a Shaker family voltage-gated K+ channel.* Science Advances, 2022. **8**(16).

32.    Tan, X.F., et al., *Structure of the shaker Kv channel and mechanism of slow C-type inactivation.* Biophysical Journal, 2022. **121**(3): p. 294a-295a.

33.    Yang, Y.S., Y.Y. Yan, and F.J. Sigworth, *How does the W434F mutation block current in Shaker potassium channels?* Journal of General Physiology, 1997. **109**(6): p. 779-789.

34.    Yellen, G., et al., *An Engineered Cysteine in the External Mouth of a K+ Channel Allows Inactivation to Be Modulated by Metal-Binding.* Biophysical Journal, 1994. **66**(4): p. 1068-1075.

35.    Grinkova, Y.V., I.G. Denisov, and S.G. Sligar, *Engineering extended membrane scaffold proteins for self-assembly of soluble nanoscale lipid bilayers.* Protein Eng Des Sel, 2010. **23**(11): p. 843-8.

36.    Inagaki, S., R. Ghirlando, and R. Grisshammer, *Biophysical characterization of membrane proteins in nanodiscs.* Methods, 2013. **59**(3): p. 287-300.

37.    Kimanius, D., et al., *Accelerated cryo-EM structure determination with parallelisation using GPUs in RELION-2.* Elife, 2016. **5**.

38.    Rohou, A. and N. Grigorieff, *CTFFIND4: Fast and accurate defocus estimation from electron micrographs.* J Struct Biol, 2015. **192**(2): p. 216-21.

39.    Scheres, S.H., *RELION: implementation of a Bayesian approach to cryo-EM structure determination.* J Struct Biol, 2012. **180**(3): p. 519-30.

40.    Zheng, S.Q., et al., *MotionCor2: anisotropic correction of beam-induced motion for improved cryo-electron microscopy.* Nat Methods, 2017. **14**(4): p. 331-332.

41.    Zivanov, J., et al., *New tools for automated high-resolution cryo-EM structure determination in RELION-3.* Elife, 2018. **7**.

42.    Chen, S., et al., *High-resolution noise substitution to measure overfitting and validate resolution in 3D structure determination by single particle electron cryomicroscopy.* Ultramicroscopy, 2013. **135**: p. 24-35.

43.    Rosenthal, P.B. and R. Henderson, *Optimal determination of particle orientation, absolute hand, and contrast loss in single-particle electron cryomicroscopy.* J Mol Biol, 2003. **333**(4): p. 721-45.

44.    Scheres, S.H. and S. Chen, *Prevention of overfitting in cryo-EM structure determination.* Nat Methods, 2012. **9**(9): p. 853-4.

45.    Pettersen, E.F., et al., *UCSF chimera - A visualization system for exploratory research and analysis.* Journal of Computational Chemistry, 2004. **25**(13): p. 1605-1612.

46.    Emsley, P., et al., *Features and development of Coot.* Acta Crystallogr D Biol Crystallogr, 2010. **66**(Pt 4): p. 486-501.

47.    Kim, D.N., et al., *Cryo_fit: Democratization of flexible fitting for cryo-EM.* J Struct Biol, 2019. **208**(1): p. 1-6.

48.    Adams, P.D., et al., *PHENIX: a comprehensive Python-based system for macromolecular structure solution.* Acta Crystallographica Section D-Structural Biology, 2010. **66**: p. 213-221.

49.    Chen, V.B., et al., *MolProbity: all-atom structure validation for macromolecular crystallography.* Acta Crystallogr D Biol Crystallogr, 2010. **66**(Pt 1): p. 12-21.

50.    Phillips, J.C., et al., *Scalable molecular dynamics with NAMD.* J Comput Chem, 2005. **26**(16): p. 1781-802.

51.    MacKerell, A.D., et al., *All-atom empirical potential for molecular modeling and dynamics studies of proteins.* Journal of Physical Chemistry B, 1998. **102**(18): p. 3586-3616.

52.    Foloppe, N. and A.D. MacKerell, *All-atom empirical force field for nucleic acids: I. Parameter optimization based on small molecule and condensed phase macromolecular target data.* Journal of Computational Chemistry, 2000. **21**(2): p. 86-104.

53.    Brunger, A., C.L. Brooks, and M. Karplus, *Stochastic Boundary-Conditions for Molecular-Dynamics Simulations of St2 Water.* Chemical Physics Letters, 1984. **105**(5): p. 495-500.

54.     Humphrey, W., A. Dalke, and K. Schulten, *VMD: Visual molecular dynamics.* Journal of Molecular Graphics & Modelling, 1996. **14**(1): p. 33-38.

## Chapter 3: Implications of the Cryo-EM structure of Kv1.2-2.1 ILT mutant in the coupling between voltage sensor and the pore domain in *Shaker*-like potassium channels

## Abstract:

Voltage-activated potassium (Kv) channels play a critical role in propagating action potentials within cells by opening in response to membrane depolarization and closing in response to hyperpolarization. The proper and timely manner that these channels open and close is essential for the health of the entire organism. Therefore, it is worthwhile studying how these channels transition from the open to closed state and vice-versa. On a deeper level, understanding how the movement of the voltage sensing domain triggered by the membrane electric field affects the opening and closing of the intracellular gate in domain-swapped, depolarization-activated channels such as *Shaker* and Kv.1.2 is of particular interest. Since the determination of its crystal structure in 2005, Kv1.2 (or Kv1.2-2.1) has been the model channel for understanding the mechanistic questions of Kv channels at the atomic level. Over the past two decades, several structures of Kv1.2 WT and mutants in various detergent or lipid environments have been determined. One significant common factor among all of the experimental structures of Kv1.2 (or Kv1.2-2.1) is that they display an open intracellular gate. In other words, we have yet to obtain the experimental structure of a voltage-activated potassium channel in its closed state. Here, in this Chapter, we present a 3.4 Å cryo-EM structure of Kv1.2-2.1 in detergent DDM/CHS with the mutation ILT in the S4 helix. This mutant has been shown functionally to right-shift the conductance-voltage (G-V) curve and decrease the opening probability ($P_0$). Although we did not capture a channel with a closed gate as we anticipated, the experimental structure displays some significant conformational changes in the voltage sensor that seems to indicate that the voltage sensor has become decoupled from the pore as a result of the ILT mutations. In the structure, the voltage sensor splays outward and some critical electrostatic interactions between gating charges and their countercharges are lost while new

ones are formed. We believe the conformation captured by our experimental structure corresponds to a transitional state from the closed to the opened gate, as the voltage sensor moves in accordance to changes in voltage in its native state.

## Introduction:

Voltage-activated potassium channels respond to changes in the electric field across the cell membrane by undergoing conformational changes that either opens or closes the ion-permeating pore. The rates of these changes are voltage-dependent due to the rearrangement of the charges in the S4 segment of the voltage sensor in direct response to the electric field. The displacement of these charged residues (four arginine residues) [3-6] in the voltage sensor through the membrane electric field creates a small current, also known as gating current [7-9]. This gating current precedes the large ionic current of potassium ions through the pore of the channel. The movement of the gating charges at S4 through the electric field not only affects the conformation of the S4 segment itself but also of the rest of the voltage sensing domain (comprised of S1 through S4 segments) as their interactions with S4 are altered [3, 5, 10]. After the movement of the voltage sensing domains, the conformational changes propagate to the inner bundle crossing helices in the S6 (which forms the intracellular gate) in order to allow ion permeation [11-14]. While we know that the S4-S5 linker plays a large role in this communication between the voltage sensor and the intracellular gate [15-17], the exact mechanism of the coupling between the voltage sensor movement to the opening/closing of the gate is largely unclear in eukaryotic systems. To add to the complexity, there are additional variables (e.g. domain-swapped vs nondomain swapped or depolarization-activated vs hyperpolarization-activated channels) that affect the coupling mechanistically and electrically. This complexity makes it difficult to pinpoint a general guide for a sensor-to-gate coupling mechanism in eukaryotic systems.

As quintessential members of the Kv1 to Kv9 families (*Shaker*-like), Kv1.2 (or Kv1.2-2.1) and *Shaker* are domain-swapped, depolarization-activated channels [18-22]. In *Shaker*, concurrent conservative mutations in the S4 known as the ILT mutations (V369I, I372L, S376T) **(Figure 3.1a)** have been shown to modify the voltage-dependent reactions of the channel, which induces a large separation of the charge distribution as well as lowering the open probability of the channel [1, 23]. This uncoupling behavior between voltage sensor and the

a)

| | 1 | 2 | 3 | 4 | 5 | 6 | 7 | charge |
|---|---|---|---|---|---|---|---|---|
| Shaker | ILRVI | RLVRVF | RIFKLSRHSK | | | | | +7 |
| ILT | --------- | I--L---T---- | | | | | | +7 |

b)

Shaker



ILT
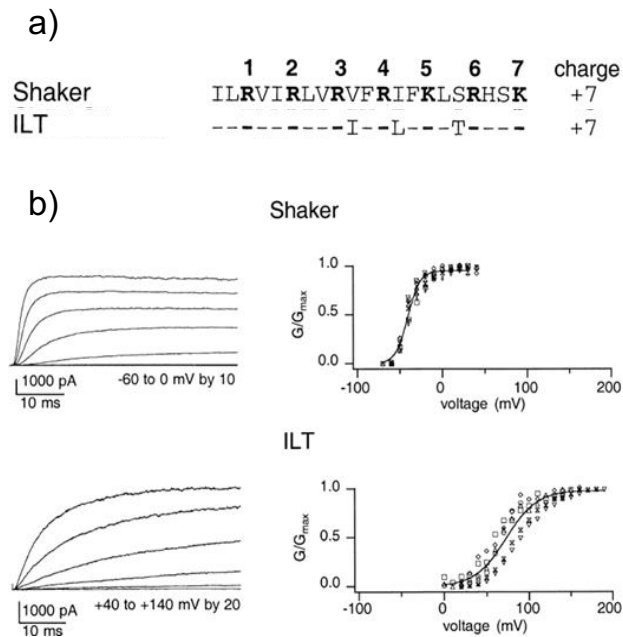


**Figure 3.1:** Functional Characterization of *Shaker* ILT mutation. Adapted from [1]. a) Sequence alignment of WT vs ILT *Shaker* with concurrent conserved mutation in S4. b) The ILT mutant right-shifts the G-V curve drastically. $V_{1/2}$ = -40.6 mV for WT *Shaker* while $V_{1/2}$ = +73.0 mV for ILT.

intracellular gate may represent an effect on the last concerted step that opens the gate once all four of the voltage sensors move independently [1, 24, 25]. Functionally, the ILT mutant interferes with the concerted movement of the four subunits that comes after the independent activation of the four voltage sensors. The conductance in the voltage axis is drastically right shifted from $V_{1/2.}$= -40.6 mV in WT *Shaker* to $V_{1/2}$ = +73.0 mV in ILT (**Figure 3.1b) [1]**, with each

ILT-mutant subunits providing equal contribution [26]. Although this mutant is well-characterized in *Shaker* functionally, the structural implication of this mutant is not yet well known.

In this Chapter, we sought to characterize the structural mechanism that may explain the behavior of ILT using Kv1.2-2.1. The cryo-EM structure of Kv1.2-2.1 with ILT mutation was obtained at ~3.4Å resolution. While our results did not capture a closed-gate structure, we did observe large conformational changes in the voltage-sensor. The rotation of the S4 helix in turn splays out the rest of the voltage sensor, altering the charge-charge interactions between S4 and the S2, S3 segments in the process. The cryo-EM structure with C1 symmetry (no symmetry imposed) reveals four voltage sensors with independently various degrees of movement. We propose that the resulting structure may be a transitional state of the voltage-sensing domain as the channel undergoes from the open to the closed gate.

## Results and Discussion:

### Functional characteristic of Kv1.2-2.1 ILT in *Xenopus* oocytes

Even though the ILT mutant is well-characterized in *Shaker*, its function is not yet known in Kv1.2-2.1 chimaera where the S3b-S4 region of Kv1.2 is replaced by that of Kv2.1 (**Figure 2.2**). Since the mutation is in the S4 segment, the chimeric region could potentially alter the functional phenotype of the ILT. Therefore, it was important to functionally characterize the mutant in Kv1.2-2.1. We expressed both the WT and ILT Kv1.2-2.1 in *Xenopus laevis* oocytes and recorded their macroscopic ion currents using the COVG (Cut-Open Vaseline Gap) voltage-clamp technique (**Figure 3.2c**) [27]. With the holding potential at -80 mV, the recording consisted of a short prepulse at -100 mV followed by a variable pulse from -100 mV to +160 mV and a recovery pulse to -40 mV. G-V curves were collected from the tail current at -40 mV for analysis (**Figure 3.2a, b**). The WT Kv1.2-2.1 exhibited a $V_{1/2}$ = 15.84 mV while the ILT Kv1.2-2.1 exhibited a $V_{1/2}$ = 108.83 mV, for a right-shift in the G-V curve of ~93 mV (**Figure 3.2d**). This

result is comparable to the right-shift in the G-V of ~113 mV observed in *Shaker* ILT. Given that the WT Kv1.2-2.1 is already more right-shift than WT *Shaker* ($V_{1/2}$ = 15.84 mV in WT Kv1.2-2.1 compared to $V_{1/2}$ = -40.6 mV in *Shaker*), however, the ILT mutant in Kv1.2-2.1 is also more right-shifted than the ILT in *Shaker*.
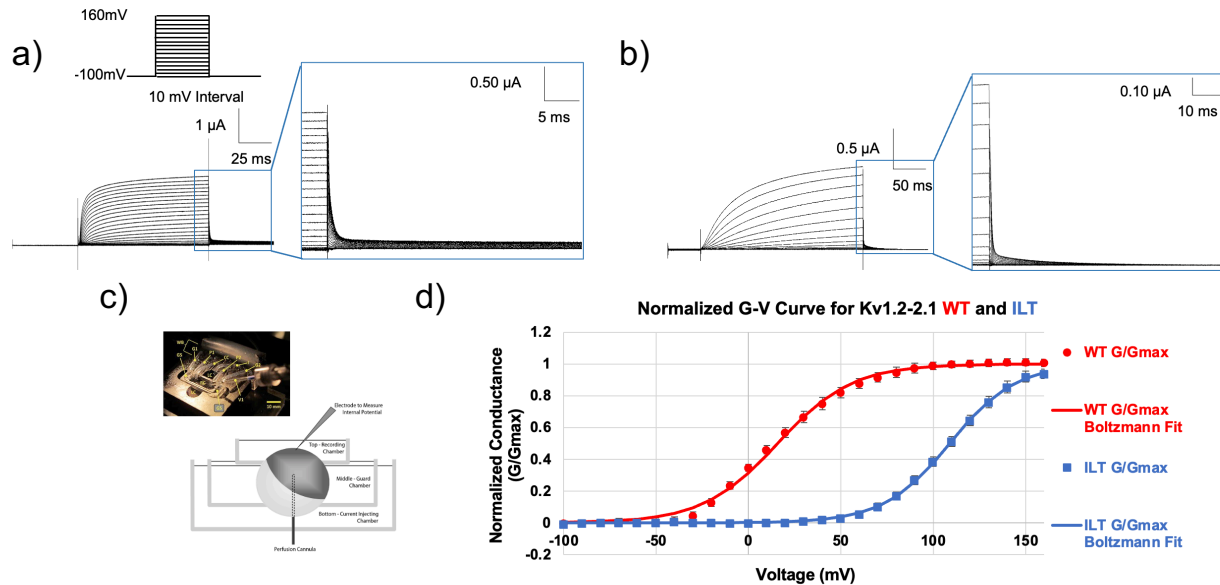


**Figure 3.2:** Kv1.2-2.1 WT vs ILT ionic current and G-V curve**.** Macroscopic ionic current of WT Kv1.2-2.1 (a) and ILT Kv1.2-2.1 (b) were recorded via cut-open voltage clamp technique (c). For both conditions, a holding potential of -80 mV was applied. A prepulse at -100 mV was followed by a variable pulse at -100 mV to +160 mV at 10 mV increments. Then the potential was returned to -40 mV to allow a positive tail current to obtain a G-V curve. For both cases, the prepulse was 50 ms and the return pulse was 100 ms. The variable pulse for WT was 150 ms while the variable pulse for ILT was 250 ms to give more time for saturation of current. d) The normalized G-V curve for WT ($V_{1/2}$ = 15.84 mV) and ILT ($V_{1/2}$ = 108.83 mV) exhibits a right-shift of ~93 mV in the ILT mutant. (n = 4 both WT and ILT)

## Expression and purification of Kv1.2-2.1 ILT in *Pichia pastoris*

The functional analysis of ILT in Kv1.2-2.1 suggests that the mutant channel would adopt a closed gate conformation at 0 mV (**Figure 3.2d**). Seeking to capture this conformation at the neutral voltage structurally, we expressed and purified the channel in *Pichia pastoris*. We received the cDNA of the rat Kv1.2-2.1 α subunit co-expressible with rat Kv β2 subunit in the pPICZ-C plasmid as a gift from R. Mackinnon (Rockefeller University). We introduced the ILT mutation on the rKv1.2-2.1 α subunit via site-directed mutation on this background. The amplified plasmid was linearized and phenol-chloroform extracted before being transformed via

65

electroporation into *Pichia pastoris* SMD1168 *his4* strain. The transformed cells were plated on YPDS plates at various zeocin concentrations for selection. Because the pPICZ-C has a zeocin resistance gene, the cells with higher copy number of the plasmid transformed would survive in the higher concentration of zeocin. The cells with the highest copy number of the pPICZ-C plasmid are also the most likely to express the most protein. Thus, the cells that survived in the highest concentration of zeocin were restreaked on 1.5 mg/ml zeocin plates and were compared for expression levels using western blot. The Kv1.2-2.1 construct has a His-tag, so we used anti-His antibodies for the western blot. The colony with the most expression was saved as a glycerol stock for large scale expression and purification. The purified proteins were then frozen on grids for cryo-EM data collection. This workflow is summarized in **Figure 2.5 from Chapter 2** and the detail of the procedure is described in the **Materials and Methods** section of this chapter.

The ILT Kv1.22.1 is well-behaved during large-scale purification in DDM/CHS. The expression/purification steps are described in detail in the **Materials and Methods** section. The size exclusion chromatography (SEC) profile reverals a sharp, gaussian peak at ~13.34 mL corresponding to the ILT Kv1.2-2.1, as verified by the SDS-PAGE (**Figure 3.3a**). The sample was concentrated to 4.5 mg/mL and was plunge-frozen in liquid ethane on Quantifoil Cu 200 1.2/1.3 grids. The dataset for this sample was collected from the Titan Krios at SLAC, where 10,134 images were collected. The micrographs display a nice distribution of single particles, and the 2D classes show a balanced mixture of top, side, and oblique views (**Figure 3.3b,c**). The data was processed in RELION 3. 7,884 images were correctly motion-corrected and used for processing. Of the 4.5M particles initially picked from RELION autopicking, ~700k particles were selected for 3D classification in C4 symmetry after three rounds of 2D classifications. The initial 3D classification was performed using the post-process 3D structure of WT Kv1.2-2.1 in high $K^+$ condition (as discussed in **Chapter 2**) as a reference. Of the four 3D classes generated from this run, the class with the best features was chosen (Class 3 in this case) as reference to

a new 3D classification using all ~700k particles. Of the four 3D classes generated from the

second round of 3D classification, a total of ~365 particles were picked from classes 2 and 3 for
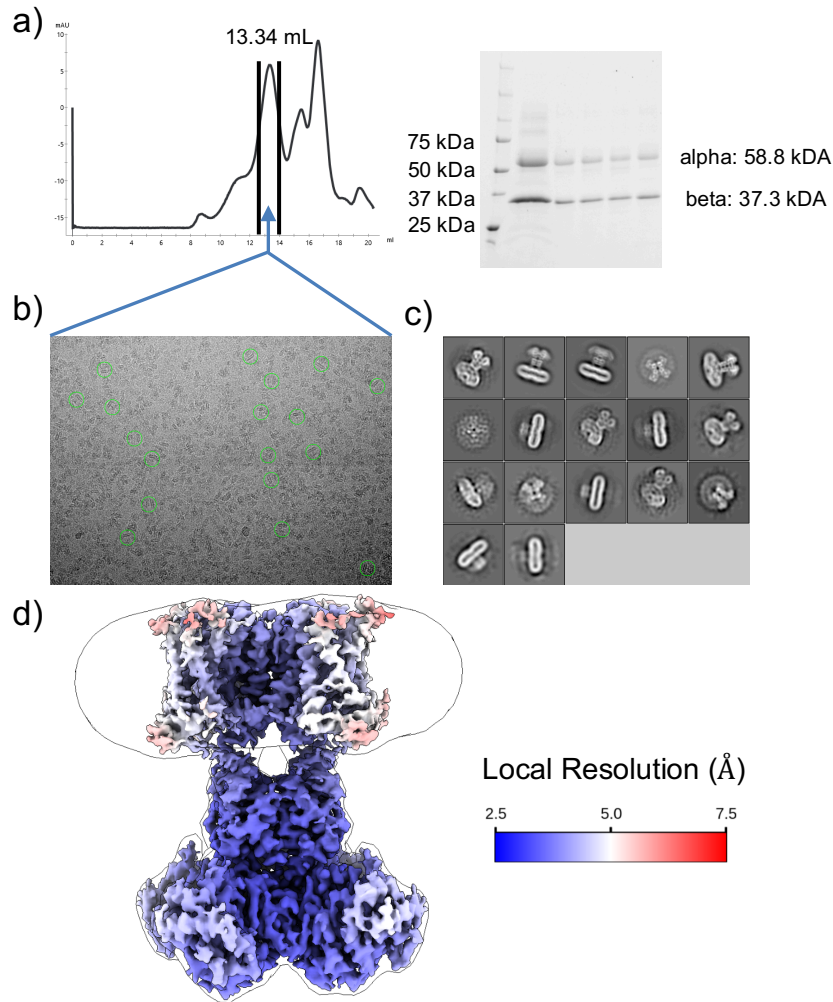


**Figure 3.3:** Cryo-EM of ILT Kv1.22.1 in DDM/CHS. a) Size exclusion chromatography (SEC) profile of ILT Kv1.2-2.1 mutant in DDM/CHS displays a narrow, gaussian peak at ~13.34 mL in Superose 6 Increase 10/300 column. SDS-PAGE of the peak fractions corresponding to the region indicated by the solid black lines shows the correct sizes indicating the presence of alpha and beta subunits. b) cryo-EM micrograph of ILT Kv1.2-2.1 mutant in DDM/CHS sample concentrated from the peak fraction in the region indicated by the solid black lines. The sample at 4.5 mg/mL concentration shows a dense distribution of single particles on the grid. c) 2D classes of ILT Kv1.2-2.1 in DDM/CHS from ~700k particles shows a balanced mixture of top, side, and oblique views. d) 3.68 Å map of entire complex filtered and colored according to local resolution fitted into a low-resolution 3D class envelope.

a third and last round of 3D classification using class 3 from the 2$^{nd}$ round as a reference. Of the

four additional classes generated from the third round of classification, classes 1,2, and 4 were

pooled for a total of 264k particles for a 3D auto-refinement. The refined structure was then

post-processed using a tight mask, yielding a 3.68 Å resolution structure, as verified by the FSC

curve using the 0.143 FSC criteria (**Figure 3.5**). The entire processing workflow is described in

**Figure 3.4**.
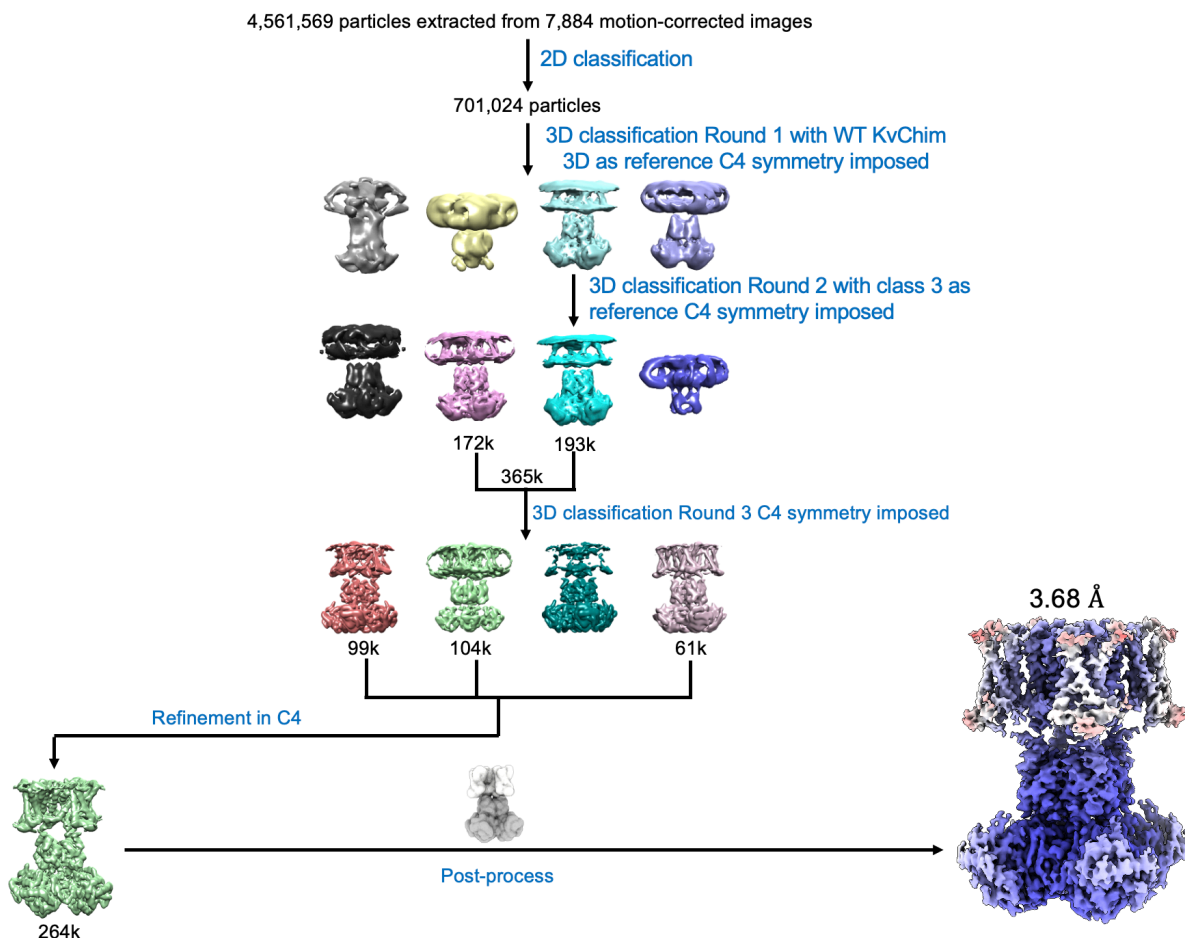


**Figure 3.4:** Cryo-EM Data Processing Workflow for Kv1.2-2.1 ILT mutant. 4,561,569 particles were extracted from 7,884 motion-corrected images using RELION's autopicking. After three rounds of 2D classifications, 701,024 particles were picked for 3D classification in C4 symmetry. The first round of 3D classification was done using the 3D structure of WT Kv1.2-2.1 in high K$^+$ condition (as discussed in Chapter 2) as a reference. Class 3 was then picked as a reference for another round of 3D classification. From the 2$^{nd}$ round of 3D classification, a total of ~365k particles were picked from class 2 (172k particles) and class 3 (193k particles) for a 3$^{rd}$ and last round of 3D classification using class 3 as a reference. Classes 1 (99k particles), 2 (104k particles), and 4 (61k particles) were chosen for refinement with a total of 264k particles. The refined structure was then post-processed using a tight mask, yielding a 3.68 Å resolution structure.

The local resolution estimation from RELION 3 was used to calculate the local resolution

of the density map. The cytosolic domain is generally higher in resolution, but the

transmembrane domain by itself is still ~4.0 Å in resolution. The resolution in the TM is higher near the selectivity filter (2.5-3.5 Å) and becomes lower in the voltage-sensing domains (3.5-4.5 Å). The cryo-EM and model building statistics are shown in **Table 3.1**.
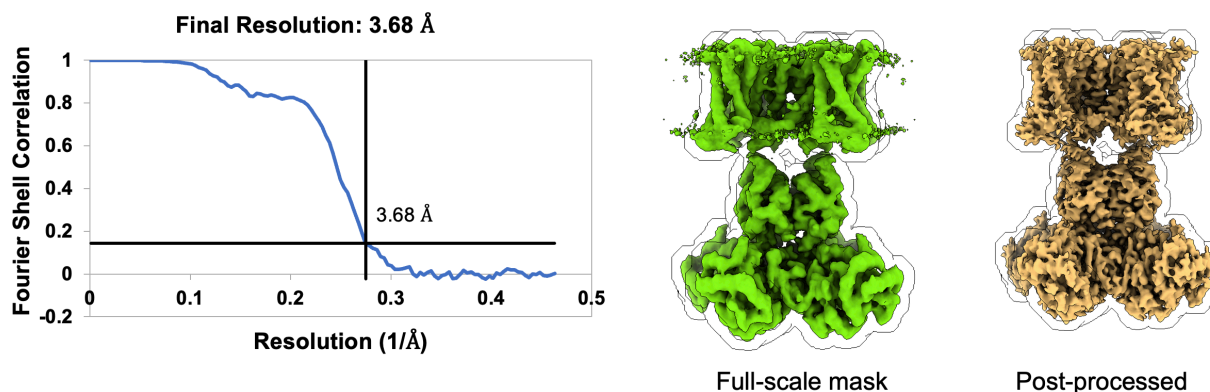


**Figure 3.5:** FSC curves of entire ILT Kv1.2-2.1 complex in DDM/CHS. FSC curve indicates the resolution of 3.68 Å according to the 0.143 FSC criteria. Mask used to calculate the FSC is shown along with the corresponding map using RELION 3's postprocessing.

When we initially tried to fit the WT Kv1.2-2.1 X-ray crystal structure (PDB ID: 2r9r) [21] into our cryo-EM density for ILT mutant, we realized that there is a slight shift/rotation of the cytosolic domain (composed of β subunit and the T1 domain from α subunit) relative to the TM domain in the density. This rotation is unsurprising as the TM and the cytosolic domains are linked by a long, flexible linker (**Figure 3.6a, 3.7a**). To resolve this issue, we built two separate models for the TM and the cytosolic domains to allow each domain to align better with the ILT density map. For the higher resolution cytosolic domain (2.8 Å), cryo-EM densities for most of the side chains were clearly visible (**Figure 3.7a**). Comparing the ILT and WT models in the cytosolic region, we noticed very little difference between the two structures. Calculation of the $C_\alpha$ RMSD between the two structures indicates that any deviation that occurs is at the periphery of the β subunit (maximum RMSD is 2.06 Å) (**Figure 3.7b**), where the β subunit expands in the ILT structure compared to the WT. This may be because the WT is a crystal structure while the ILT is a cryo-EM structure. The lack of crystal contacts in the cryo-EM single particles between

molecules may allow the particles to expand slightly at the periphery compared to molecules restricted in crystal lattice. Nonetheless, the movement in the cytosolic domain is quite small.
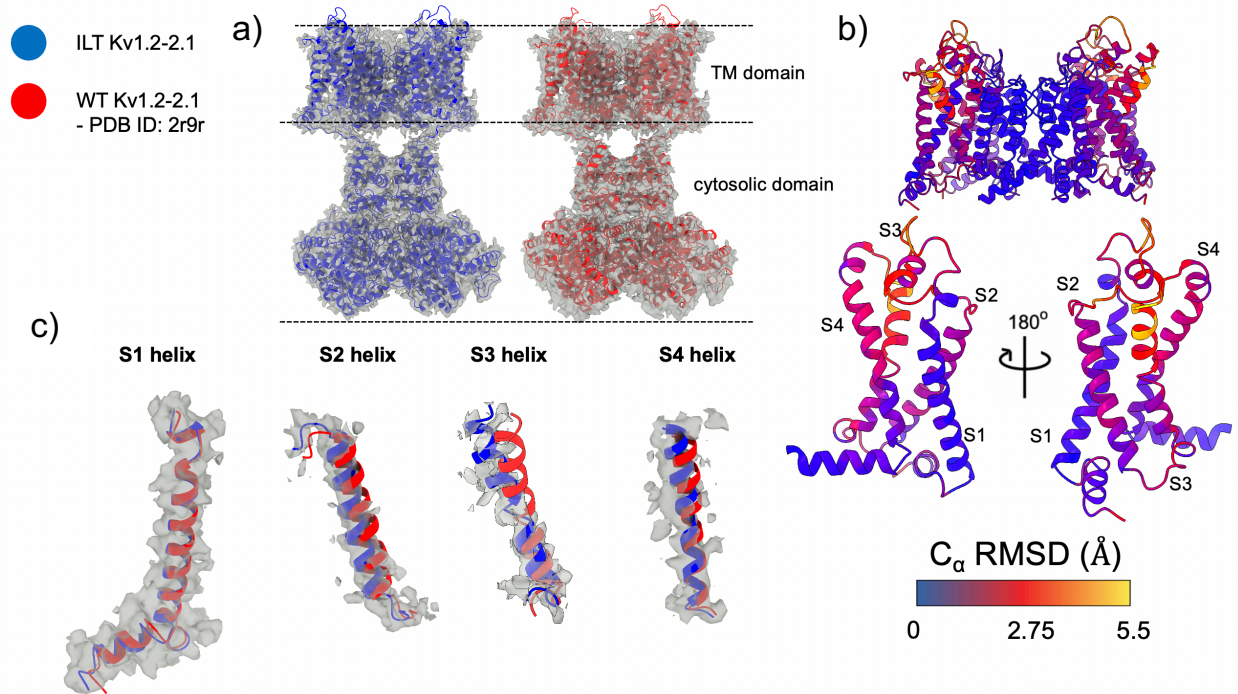


**Figure 3.6:** ILT vs WT model exhibits the most deviations in the VSD. a) Fitting of the ILT (blue) and WT (PDB ID: 2r9r) (red) cartoon models into the 3.68 Å ILT Kv1.2-2.1 density map with C4 symmetry imposed. For the ILT model, TM and cytosolic domains were generated separately because there was a shift/rotation of the cytosolic domain relative to the TM domain in the ILT density compared to the full-length WT model. Displayed is the TM and cytosolic domains separately fitted into the ILT density for both ILT and WT models to best fit the density. b) TM domain of the ILT Kv1.2-2.1 model is colored by $C_\alpha$ RMSD between WT and ILT. The largest deviations occur in the VSD (up to 5.5 Å $C_\alpha$ RMSD in the S3 helix), which is highlighted by the 180-degree rotation of the VSD from a monomer. c) S1-S4 helices in the VSD from ILT (blue) and WT (red) models are fitted into the ILT density map. The largest deviations are in the upper part of the S3 helix where the helix straights out in the ILT mutant relative to the WT. S4 helix in ILT is more elongated and slightly moves away from the pore domain. S2 helix in the ILT slightly moves away from the pore domain. There is no noticeable difference in the S1 helix.

**Table 3.1:** Cryo-EM and model building statistics for ILT Kv1.2-2.1

| Data Collection | |
|---|---|
| Protein concentration | 4.5 mg/mL |
| Sample volume for EM grid | 3.5 µL |
| Grid type | Quantifoil Cu 1.2/1.3 |
| Plunge freezer | Mark IV ThermoFisher |
| Blotting time | 3.5 s |
| Blotting temperature | 4 °C |
| Blotting chamber humidity (set/measured) | 100%/100% |
| Microscope | FEI Titan Krios |
| Voltage | 300 kV |
| Camera | Gatan K3 |
| Energy Filter | Yes |
| Cs corrector | No |
| Nominal defocus range | -1.5 to -2.5 µm |
| Physical pixel size | 1.08 Å/px |
| Super-resolution pixel size | 0.54 Å/px |
| Total dose | 50 e-/Å2 |
| Number of frames | 40 frames |
| Exposure time | 12 s |
| Number of images collected | 10,134 images |
| | |
| **Reconstruction (Relion 3)** | |
| Number of motion-corrected images used for processing | 7,884 images |
| Picked particle number | 4,561,569 particles |
| Particle number after 2D classification | 701,024 particles |
| Final particle number | 264,951 particles |
| Full molecule resolution in C4 | 3.68 Å |
| Transmembrane resolution in C4 | 4.0 Å |
| Map sharpening B-factor | -182 |
| | |
| **Model Refinement** | |
| Refinement resolution limit | 4.0 Å |
| FSC (map, model) = 0.143 FSC | 3.68 Å |
| | |
| **RMS deviations** | |
| Bond length | 0.0069 Å |
| Bond angle | 0.75° |
| | |
| **Ramachandran plot** | |
| Favored (%) | 90.51% |
| Allowed (%) | 9.49% |
| Outlier (%) | 0.00% |
| | |
| **Validation** | |
| MolProbity Score | 2.28 |
| Clash Score | 11.6 |
| EM Ringer Score | 2.69 |

The TM domain of ILT structure, on the other hand, exhibits greater and more interesting deviations from the WT structure. Calculation of the $C_\alpha$ RMSD between the two structures indicates that the largest conformational changes occur in the VSD, specifically in the S2, S3, and S4 helices, where the VSD moves away from the pore domain. (**Figure 3.6b, c**). Considering that the ILT mutation is in the S4 helix, it could be interpreted that the movement from S4 helix pushes on the S2 and S3 helices to undergo a cascade movement away from the pore. S2 helix simply translates away from the pore, while S4 helix also slightly elongates. S3 helix undergoes by far the largest rotational movement in the upper half of the helix away from the pore (**Figure 3.6c**).
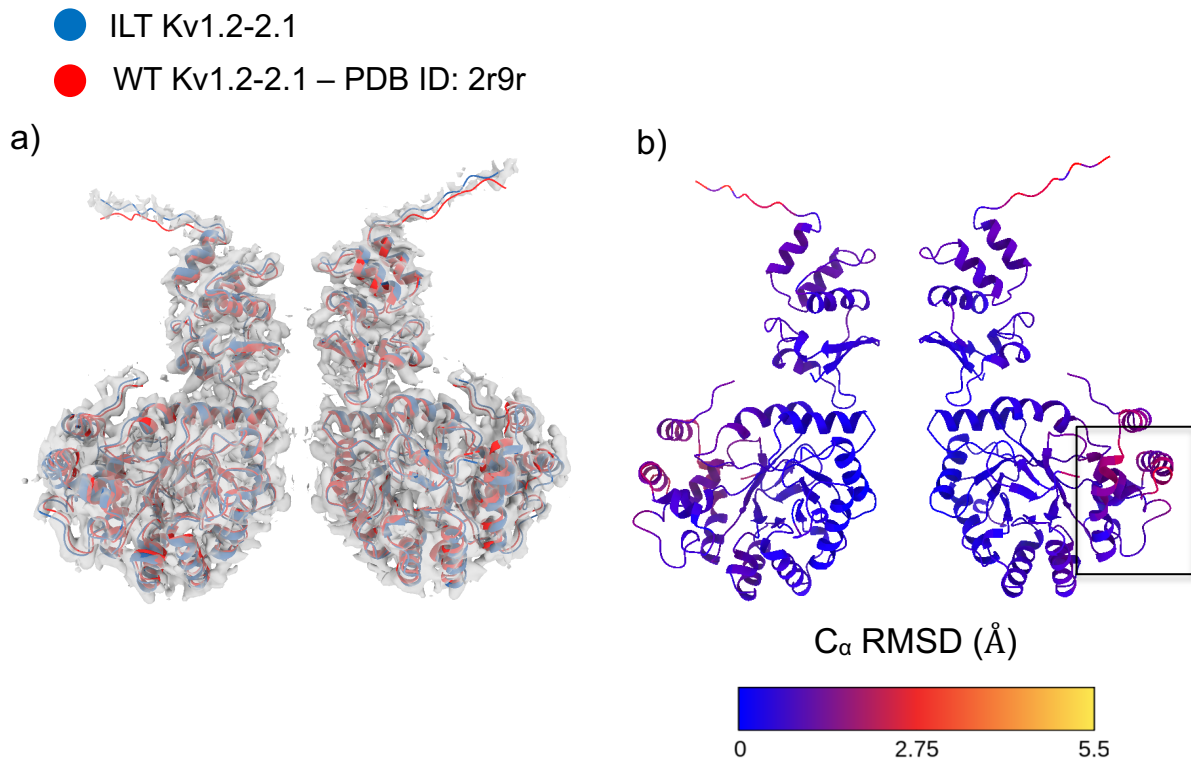


**Figure 3.7:** Comparison of the ILT and WT Kv1.2-2.1 models reveals small differences in the cytosolic domain**.** a) Overlap of the 2.8 Å ILT Kv1.2-2.1 C4 cytosolic density map with ILT (blue) and WT (red) (PDB ID: 2r9r) cartoon models. Both models fit tightly into the high-resolution map of the cytosolic domain, revealing small deviations between the two models in the cytosolic domain**.** b) Cytosolic domain of the ILT Kv1.2-2.1 model colored by $C_\alpha$ RMSD between WT and ILT. The two models exhibit very small differences in structure and the largest deviations (2.06 Å) are at the periphery of the β subunit (indicated by the square box). The ILT model is more expanded at the periphery, which may be due to the lack of crystal contacts between the molecules in cryo-EM to restrict the movement of the β subunit.

The pore domain remains mostly the same between ILT and WT structures according to the $C_\alpha$ RMSD calculation (**Figure 3.8a**). As shown in **Figure 3.8b**, both the ILT and WT models fit tightly inside the ILT density map. Therefore, like the WT, the ILT structure also exhibits an opened conformation for the intracellular gate as well as a conductive selectivity filter (**Figure 3.8c, d, e**). This was a surprising result for us. While we expected the selectivity filter conformation would be unaffected by the ILT mutation, we did expect to capture the closed gate conformation for the intracellular gate through this construct that drastically right-shifts the G-V curve (**Figure 3.2d**).
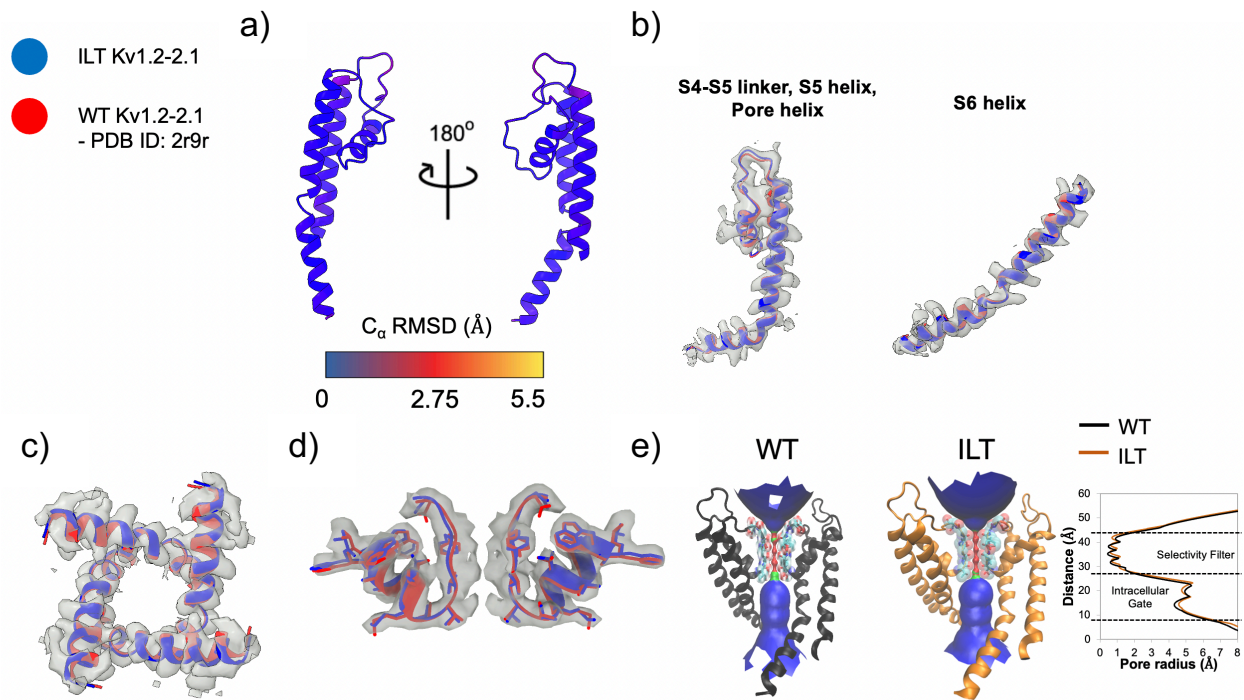


**Figure 3.8:** Pore domain of ILT displays an open gate and a conductive selectivity filter. a) Pore domain of the ILT Kv1.2-2.1 model is colored by $C_\alpha$ RMSD between WT and ILT. There are little to no deviations between the two structures in the pore domain (largest deviation is 0.67 Å). b) Overlap of the ILT density map with ILT and WT models for the S4-S5 linker, S5 helix, the pore helix, and the S6 helix that forms the intracellular gate. Both models fit tightly into the ILT density, indicating the similarity between the two structures in the pore domain. c) Overlap of the ILT density map with ILT and WT models shows an open conformation of the intracellular gate in the ILT mutant similar to the WT. d) Overlap of the ILT density map with ILT and WT models shows a conductive selectivity filter in the ILT structure similar to WT. e) Profile of the ion permeation pathway generated by HOLE [2] program shows little difference in ion permeation between ILT and WT structures through the selectivity filter and the intracellular gate, confirming the conductive SF and the open gate.

Taking a closer look at the VSD where the most conformational changes occur, we noticed that the side chains in S4 and S2 move quite dramatically (**Figure 3.9a, b**), altering some crucial interactions between the gating charges in S4 and the countercharges in S2. For example, the GLU226 (E1 counter charge) in S2 forms a strong hydrogen bond with ARG299 (R4 gating charge) in WT. This bond is disrupted or weakened in ILT due to the S2 and S4 helices moving apart from one another. Instead, GLU226 (E1) forms a stable H-bond with ARG296 (R3) (**Figure 3.9c**). Another critical interaction that is disrupted in ILT is between GLU236 (E2) and K302 (K5). These residues for a strong hydrogen bond with each other below the hydrophobic gasket in WT. In the ILT, the two residues lose their H-bond interaction as the S2 and S4 helices separate further (**Figure 3.9d**).
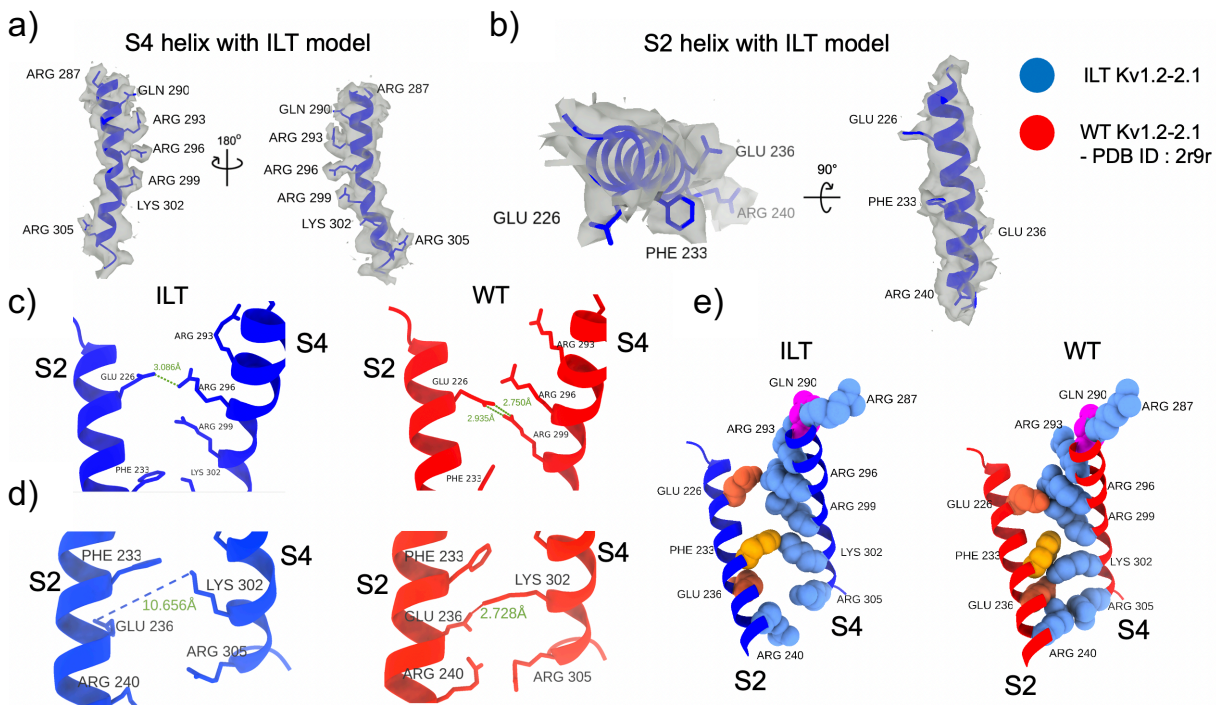


**Figure 3.9:** S2-S4 interactions are altered as a result of helical movements in S2 and S4 in ILT. a) S4 helix of the ILT Kv1.2-2.1 is shown with the ILT side-chain densities for the gating charge residues (R287 (R0), Q290, R293 (R2), R296 (R3), R299 (R4), K302 (K5), R305 (R6)). b) S2 helix of the ILT Kv1.2-2.1 is shown with the ILT side-chain densities for the countercharges (E226 (E1) and E236 (E2)) as well as the hydrophobic gasket (F233) and the lower R240. c) E226 (E1) – R299 (R4) interaction is disrupted as the S2 helix moves apart from the S4 helix in the ILT. Instead, E226 (E1) adopts a stronger H-bond with R296 (R3). d) E236 (E2) – K302 (K5) interaction is disrupted as the S2 helix moves apart from the S4 helix in the ILT. e) Overall changes in interactions between S2 and S4 helices for the ILT structure. Besides the E1-R4 contact to E1-R3 contact, the position of the K302 relative to the hydrophobic gasket residue (F233) is altered. Furthermore, R240 from S2 and R305 from S4 repel each other strongly in ILT.

Some other interactions are formed/disrupted. In the WT, K302 (K5) is below the hydrophobic gasket F233 but in the ILT K302 is moved next to F233, indicating that it may be in a transitory state to move above the hydrophobic gasket. Also, ARG240 from S2 and ARG 305 (R6) from S4 move away from each other in ILT due to the separation of S2 and S4 helices. Overall, the splaying apart of the S2 and S4 helices in the conformational changes may create more room for more water to possibly penetrate through the VSD from above and below to affect the dielectric constant through the VSD. The changes in interactions between S2 and S4 may capture the transitionary state between VSD that is fully coupled to the pore and one that is fully uncoupled (**Figure 3.9e**).
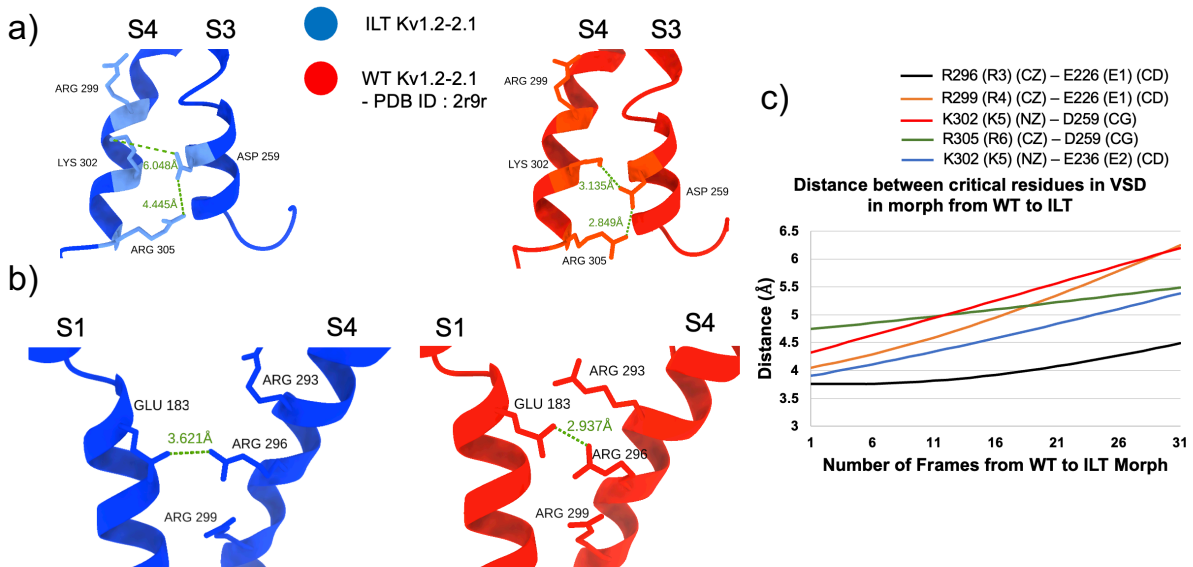


**Figure 3.10:** S4 interactions with S3 (D259) and S1 (E183) are disrupted in ILT. a) Critical S3-S4 interaction occurs between D259 in S3 with K302 (K5) and R305 (R6) in S4 helix. In the ILT structure, the hydrogen bond interaction of the gating charges with the D259 is weakened or disrupted. b) Critical S1-S4 interaction occurs between E183 (E0) in S1 with R296 (R3) in S4 helix. In the ILT structure, the hydrogen bond interaction of the R3 with E0 may be weakened. c) Graphical representation depicting the increase in distance between gating charge residues in S4 and counter-charge residues in S2 and S3 in a morph from WT to ILT VSD conformation. This increase in distance weakens, disrupts, and breaks the critical hydrogen bonds.

Other hydrogen bond interactions are weakened or disrupted in the VSD as a result of the conformational change in the ILT. In the WT, D259 in S3 helix and K302 and R305 from S4 helix coordinate via hydrogen bond below the hydrophobic gasket, F233. In the ILT mutant,

75

however, the large conformational change in the S3 helix away from the S4 disrupts the hydrogen bond interaction, allowing the K302 and R305 in S4 to adopt a conformation that no longer interacts with D259 in S3 (**Figure 3.10a**). Also, in WT, E183 in S1 helix hydrogen bonds with R296 in S4 helix. This interaction may not be destroyed but may be weakened in the ILT structure (**Figure 3.10b**). Overall, the distance between gating charges and their countercharges in the VSD increases in the ILT mutant compared to the WT, either weakening, replacing, or destroying the hydrogen bond interactions from the WT (**Figure 3.10c**).

To study the difference in water permeation through the VSD, we performed an MD simulation using a monomeric VSD in POPC membrane solvated in water and 100 mM KCl. We created four models of monomeric VSD in our simulation: WT (PDB ID: 2r9r) VSD with WT coordinates for initial state, ILT VSD with ILT coordinates for initial state, WT VSD with ILT coordinates for initial state (ILTtoWT), and ILT VSD with WT coordinates for initial state (WTtoILT). Each construction in membrane was run for 50 ns without any restraints after initial energy minimization and equilibration.

2D profile of the water penetration shows much more water molecules occupying the VSD in the ILT mutant (**Figure 3.11a, b, c, d**). While the WT only has water permeation into the VSD from the bottom generally (a, b), the ILT displays water penetration from both the top and the bottom of the VSD all the way to the hydrophobic gasket at $Z = 0$. The 1D shows the same result in graphical form with positions of critical side-chains relative along the $Z$ axis (**Figure 3.11e**). We observe that the deviations in water penetrations between WT and ILT occur where R299 (R4) and R296 (R3) are. This is where the S2 and S4 helices move apart the most, disrupting the E1-R4 interaction from WT and stabilizing the E1-R3 interaction (**Figure 3.9c**). These results overall may suggest the general weakening of the interactions between the gating charges and the countercharge E1, thus transitioning the VSD into a decoupled state.
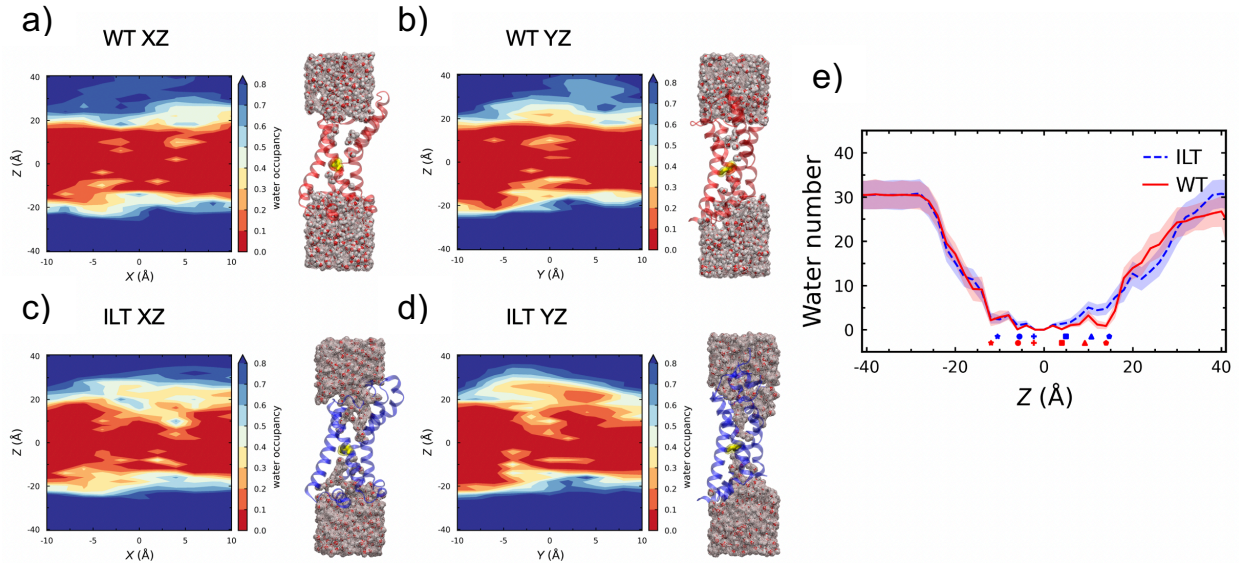
**Figure 3.11:** MD simulation reveals difference in water permeation through the VSD ILT vs WT
a, b, c, d) 2D MD simulation profile of water penetration through a monomeric VSD in the *X-Z* and *Y-Z* planes for WT and ILT mutant are shown. WT simulation in *X-Z* plane (a) and *Y-Z* plane (b) show only a slight amount of water penetrating the VSD, both from the top or the bottom. ILT simulation in *X-Z* plane (c) and *Y-Z* plane (d) show a significantly more water penetrating through the VSD from both the top and the bottom, all the way into the hydrophobic gasket residue F233 at *Z*=0.
e) 1D MD simulation of the water penetration profile along the *Z* axis displays more water being occupied above the hydrophobic gasket (for 0 < *Z* < 20). *Z* = 0 refers to the position of the hydrophobic gasket, F233. The positions of each critical residue side chains along the *Z* axis are labeled with various shapes, with blue color corresponding to the ILT residues and the red color corresponding to the WT residues. From left to right, the residues are: R305 (R6) (CZ), K302 (K5) (NZ), F233 (CA), R299 (R4) (CZ), R296 (R3) (CZ), and R293 (R2) (CZ).
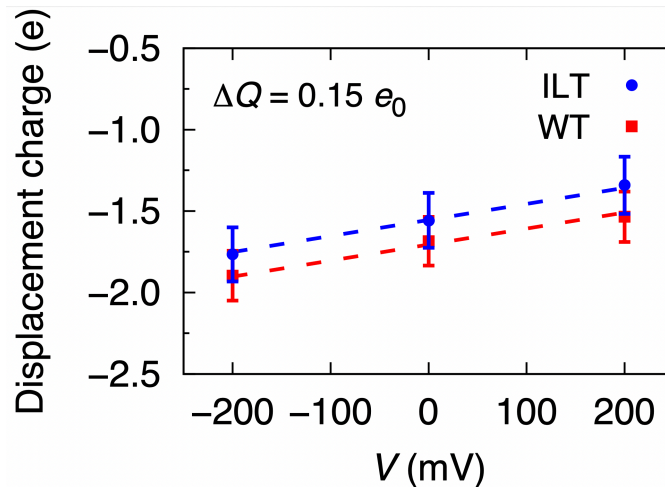


**Figure 3.12:** VSD gating charge displacement ILT vs WT. Average displacement charge was calculated using the formula using $\langle Q_d \rangle = \langle \sum_i q_i \frac{z_i}{L_z} \rangle$, where $q_i$ is the partial charge of $i^{th}$ atom, $z_i$ is its unwrapped $z$ coordinate of $i^{th}$ atom, and $L_z$ is the length of the simulation system in the $z$-direction. 20 ns simulation trajectory at -200 mV, 0 mV, and +200 mV were used to estimate the average displacement charges. Overall, there is ~0.15 $e_0$ per monomer of outward charge displacement in ILT compared to WT VSD.

We also sought to estimate the displacement of gating charge in ILT compared to WT using molecular dynamics computations [28]. For this, each of the four constructions was run for 20 ns at three points of electric field: -200 mV, 0 mV, and +200 mV (**Figure 3.12**). Overall, there is an outward gating charge displacement of ~0.15 $e_0$ in ILT relative to WT for every VSD. In total, then, there is ~0.6 $e_0$ charge displacement for each channel. While the difference is small, this disparity could explain the ILT structure as the intermediate state between the VSD coupled and decoupled to the intracellular gate.

## Discussion

In this chapter, we presented the function of structure of ILT mutant in Kv1.2-2.1 channel. The functional characterization of the mutant with Kv1.2-2.1 was important because the mutations occur in the S4 helix [1] and the S3b-S4 region is different for the chimera compared to Kv1.2 and *Shaker* [21]. As in *Shaker*, the ILT mutant in Kv1.2-2.1 right-shifts the G-V curve significantly. While the shift itself is less in Kv1.2-2.1 compared to that in *Shaker*, the WT Kv1.2-2.1 is already more right-shifted than WT *Shaker*, resulting in a comparable G-V curve of ILT between *Shaker* and Kv chimera. We wondered if the fact that the R1 gating charge from *Shaker* or Kv1.2 is neutralized in Kv1.2-2.1 (Q290 rather than an arginine) may affect the ILT mutant, but it seems that this difference doesn't affect the functional behavior of the mutant. This mutant is known to affect the coupling between voltage-gating and ionic conduction by increasing the energetic barrier for the last VSD transition in the activation pathway [1, 17, 23, 29]. This accounts for only the final 15% charge movement, which is equivalent to 1.6-1.8 $e_0$ per channel [1]. The functional behavior of the mutant would predict a structure displaying an activated VSD but a closed intracellular gate.

In contradiction with this prediction, our 3.68 Å cryo-EM ILT Kv1.2-2.1 structure revealed an opened-gate conformation with a conductive selectivity filter. Despite this, we saw conformational changes in the voltage-sensing domains (VSDs) that disrupted crucial

interactions between S2-S4 and S3-S4. S4 remained in the activated conformation but

displayed slight elongation. Still, there were no notable interactions observed with mutated

residues (I300L, S304T) with other residues. We also noticed no noticeable movement in the

S4-S5 linker. We observed the presence of more water molecules through the VSD and above

the hydrophobic gasket (F233) of the ILT mutant compared to the VSD of WT. MD computations

indicate that there is a small outward gating charge movement in the ILT compared to WT of

~0.6 $e_0$ per channel.
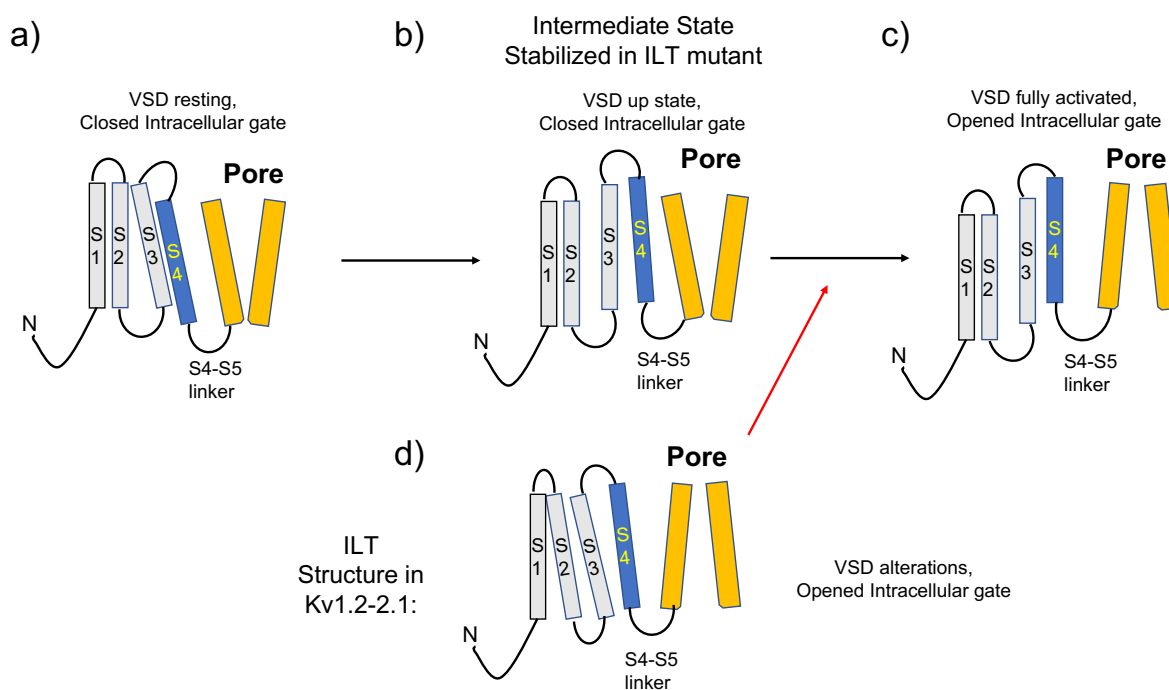


**Figure 3.13:** Structure of ILT in Kv1.2-2.1 may represent a secondary intermediate state between VSD resting, closed gate and VSD fully activated, opened gate conformations. From functional analysis of ILT, between the a) resting VSD, closed intracellular gate and c) fully activated VSD, opened gate conformation is a stabilized intermediate state where b) VSD is in the up state and the gate is closed. In the ILT Kv1.2-2.1 structure, however, we observe an altered VSD state with an opened gate. This, we suggest, is a secondary intermediate state from conformation a) and c).

According to functional analysis in *Shaker*, the ILT mutant stabilizes an intermediate

state between the VSD resting, closed intracellular gate conformation (**Figure 3.13a**) and the

VSD fully activated, opened intracellular gate conformation (**Figure 3.13c**). This intermediate

state is described by the VSD in the up-state and the intracellular gate in the closed state (**Figure 3.13b**) [1, 26, 30]. In our ILT structure of Kv1.2-2.1, we obtained an altered VSD state (with critical electrical interactions disrupted or replaced) and an opened intracellular gate (**Figure 3.13d**). Within the functional narrative, we propose that our ILT structure lies between the expected up-state VSD, closed gate conformation and the activated VSD, opened gate conformation. Perhaps we have a secondary intermediate state.

Two critical factors may explain the differences in functional analysis of ILT mutant in Kv1.2-2.1 and its structure. Firstly, the detergent environment in which the structure was determined may alter the local environment of the ILT channel, somehow destabilizing the closed-gate conformation that may be seen in a lipid-bilayer environment. Secondly, the first gating charge (R1) in *Shaker* and Kv1.2 is an uncharged asparagine (Q1) in Kv1.2-2.1. This means that there is one less gating charge that needs to cross the hydrophobic gasket for Kv1.2-2.1 compared to *Shaker* to reach the activated VSD conformation. It is unclear how this difference may affect the S4 interaction with the S4-S5 linker and subsequently the interaction with the pore domain to induce opening and closing of the intracellular gate.

## Materials and Methods:

**Materials**

*Xenopus laevis* oocytes were provided by the lab of Francisco Bezanilla. The oocytes were harvested from ovaries of the toads in accordance with the experimental protocols approved by the University of Chicago Animal Care and Use Committee. The cut-open voltage clamp rig was set up in the Bezanilla lab according to Stefani and Bezanilla, 1998 [27]. For both WT and ILT, the external solution contained 12 mM KCl, 108 mM N-methyl-D-glucamine (NMDG), 10 mM HEPES, and 2 mM $CaCl_2$ set to pH 7.5 with 2-(*N*-morpholino)ethanesulfonic acid (MES), while the internal solution contained 120 mM KCl, 10 mM HEPES, and 2 mM EGTA set to pH 7.5 with KOH.

Detergents were purchased from Anatrace, lipids from Avanti Polar Lipids, Superose 6 Increase 10/300 column from GE Healthcare, anti-His-tag antibodies from GenScript, TALON cobalt resin from Clontech, Biobeads SM-2 resin from Bio-Rad Laboratories, and Zeocin from Invitrogen Life Technologies. Other reagents were purchased from Sigma, Thermo Fisher Scientific, and GoldBio. Yeast cells were pulverized in Retsch PM 100 planetary ball mill in 125 mL grinding jars. Ultracentrifugation was performed on Beckman Coulter L-90K centrifuge using a Ti-45 rotor. Culture media for *Pichia pastoris* were prepared as described in the '*Pichia* Expression Kit' manual (Invitrogen Life Technologies). cDNA of the rat Kv1.2-2.1 chimera α subunit combined with a rat β2.1 gene (residues 36–367) in the pPICZ-C plasmid was a gift from R. MacKinnon (Rockefeller University) [21]. The ILT mutation of Kv1.2-2.1 were done on this background.

The lysis buffer consisted of 150 mM KCl, 50 mM Tris-HCl titrated to pH 7.5, 2 mM Tris(2-carboxyethyl) phosphine (TCEP) titrated to pH 7.5 with NaOH, 5 mM β-mercaptoethanol (β-ME), 0.1 mg/mL DNAseI, 0.1 mg/mL pepstatin A, 1 μg/mL aprotinin, 1 μg/mL leupeptin, 0.1 mg/mL soybean trypsin inhibitor, 1 mM benzamidine, 2 mM PMSF.

The column wash/elution buffer consisted of 150 mM KCl, 50 mM Tris-HCl titrated to pH 7.5, 2 mM TCEP, 5 mM β-ME, 5 mM dodecyl-maltoside/Cholesteryl Hemisuccinate Tris Salt (DDM/CHS), 0.025 mg/mL lipid mixture (3:1:1 ratio) of 1-palmitoyl-2-oleoyl-*sn*-glycero-3-phosphocholine (POPC), 1-palmitoyl-2-oleoyl-*sn*-glycero-3-phosphoethanolamine (POPE) and 1-palmitoyl-2-oleoyl-*sn*-glycero-3-[phospho-rac-(1-glycerol)] (POPG).

The gel-filtration buffer consisted of 150 mM KCl, 20 mM Tris-HCl, 2 mM TCEP, 2 mM DTT, 1 mM DDM/CHS and 0.025 mg/mL of the lipid mixture (3:1:1 POPC/POPE/POPG). The final buffer pH was adjusted to 7.5 using KOH.

To prepare a 10% stock solution of DDM/CHS (~200 mM), 5g of dry DDM was added to a 50 mL falcon tube containing 40 mL of 200 mM Tris pH 8.0 and was rotated until the detergent goes into the solution. Then 1g of CHS was added to the detergent solution and the resulting mixture in the falcon tube was sonicated continuously until solution became hot to the touch and translucent. Volume was brought up to 50 mL with water and the tube was rotated at RT until solution became transparent. The stock solution was stored in 4 °C.

To prepare the lipid mixture of POPC/E/G for buffer preparation, the lipids in chloroform were first mixed at the 3:1:1 ratio in a round-bottom glass flask, and then rotary evaporator or stream of nitrogen gas was used to remove chloroform. The dried lipid mixture was stored in a desiccator for at least 24 hr protected from light. Dry lipids were resuspended in 1% DDM/CHS solution and sonicated until the mixture was transparent. Then the detergent-lipid mixture was added to the buffers according to the protocol.

**Oocyte preparation for COVG**

*Xenopus laevis* oocytes were harvested via incision from the ovary of the toad anesthetized with a tricaine solution, in accordance with the experimental protocols approved by the University of Chicago Animal Care and Use Committee. Following the collagenase digestion of the follicular membrane, oocytes were stored at 18°C in standard oocyte solution (SOS)

containing 96 mM NaCl, 2 mM KCl, 1.8 mM $CaCl_2$, 1 mM $MgCl_2$, and 10 mM HEPES, pH 7.4,

with 10 µg/mL gentamicin. Oocytes were typically injected a day after digestion.

## mRNA preparation of Kv1.2-2.1 for COVG recording

To express Kv1.2-2.1 in *X. laevis*, we used the pMAX vector with a T7 promoter

containing Kv1.2, which was a gift from Anthony Lewis (University of Portsmouth). We first

created the empty pMAX vector by removing the Kv1.2 gene and then inserted the Kv1.2-2.1

alpha subunit as the coding sequence into the empty pMAX vector. Then ILT mutation was

introduced via site-directed mutagenesis. The DNA was prepared using the NucleoSpin Plasmid

kit (Macherey-Nagel) and was linearized with PmeI (New England Biolabs). Linearized cDNA

was transcribed into mRNA with mMESSAGE mMACHINE T7 kit (Life Technologies). Oocytes

were injected with 50 ng of mRNA using a Drummond nanoinjector and were incubated at 18 $^{\circ}$C

in the standard oocyte solution (SOS) with 10 µg/mL gentamicin. COVG recordings were made

24-48 hours after injection to allow for proper expression and trafficking of Kv1.2-2.1 into the

oocyte membrane. The WT Kv1.2-2.1 expressed in oocytes quickly and were therefore

recorded 24 hours after injection, while the ILT expressed slowly and were recorded 48 hours

after injection.

## Cut-open Vaseline-Gap (COVG) Voltage Clamp

The cut-open oocyte voltage clamp technique was used to allow for fast exchange of

internal ionic solutions for low $K^+$ conditions while maintaining high clamp fidelity and low noise.

All recordings were performed at ~20 °C. The SB6711 digital signal processor-based board with

an A4D4 board was controlled by Gpatch, the in-house software and GUI. Oocytes were held

under voltage clamp using the Dagan CA-1B amplifier. Current was filtered at 5 kHz.

The microelectrodes were pulled from a Flaming-Brown micropipette puller (Model P-87; Sutter Instruments) and were filled with 3M $CsCl_2$ with a resistance of ~0.4-0.6 MΩ. Low resistance access to the oocyte interior was obtained by permeabilizing the oocyte with 0.1% saponin carried by the internal solution. Recordings were taken with holding potential at -80 mV, a prepulse of -100 mV for 50 ms, variable voltages from -100 mV to +160 mV at 10 mV increments (for 150 ms for WT, 250 ms for ILT), and a return back to --40 mV for 100 ms.

## Transformation, Expression, and Purification

The pPICZ-C plasmid with both rKv1.2-2.1 and rβ2.1 was used for molecular biology and site-directed mutagenesis to create the ILT mutant. The mutant plasmid was linearized and checked for proper size using DNA gel electrophoresis. This was an important step as some site-directed mutagenesis with the pPICZ-C vector sometimes yield internal recombination that yield improper (usually much smaller than expected) plasmid sizes. Once the ILT mutant was sequence verified, it was linearized with PmeI and then purified by phenol-chloroform extraction. For the extraction, we followed the protocol from Pacific Biosciences: https://www.pacb.com/wp-content/uploads/2015/09/SharedProtocol-Extracting-DNA-usinig-Phenol-Chloroform.pdf. About 25-40 µg of the linearized-purified DNA was transformed into yeast *Pichia* pastoris SMD1168 *his4* strain via electroporation. The parameters used were 2500 V, 25 µF, and 400 Ω, with time constant ranging from 6-9 msec. After electroporation, The *P. pastoris* clones with successful cDNA integration into the yeast genome were selected on agar plates containing yeast extract, peptone, dextrose, sorbitol (YPDS) in four different Zeocin concentrations: 0.1, 0.5, 1 and 1.5 mg/mL. Selected colonies were grown in small-scale liquid culture containing 0.1 mg/mL zeocin and were screened for protein expression with anti-His-tag western blotting.

The clone of *P.* pastoris with the most expression in the small-scale was stored as a glycerol stock to be used for large-scale growth and expression. All yeast cells were grown in

baffled flasks with a 1:3 medium/air ratio in a 30 °C shaker (250 r.p.m) incubator. The selected

clone for large-scale expression was inoculated into 30 mL of buffered minimal glycerol (BMG)

media containing 0.1 mg/mL zeocin and was grown for 36 hr. The culture was diluted with 4 L of

BMG media to an optical density (OD) of ~0.2, then grown for 24 hr until OD reached 3-5. The

yeast cells were then collected by centrifugation at ~5000g for 10 min at RT, resuspended (OD

of ~1.5-2) and grown in 4 L of buffered minimal methanol (BMM) media. After 24 hr, an

additional dose of 0.5% methanol was added to the media to sustain protein induction. After

another 24 hr (for a total of 48 hr induction period), the culture was harvested by centrifugation

at 5000g for 10 min at 4 °C. Pellet was made into a thin noodle via running it through a 60 mL

syringe as it was being immediately frozen in liquid nitrogen. Then the frozen cell noodles were

crushed and stored at -80 °C.

For purification, frozen yeast cell noodles were further pulverized with a Retsch PM100

planetary ball mill in 125 mL grinding jar via 2 min of milling at 400 r.p.m. followed by 1 min of

reverse rotation repeated eight times with a 3 min of liquid-nitrogen cooling in between. The

resulting pulverized cell powder could be stored in -80 °C until further use. To further

purification, the cell powder was thawed at RT in lysis buffer (6 mL/g) for 3 hr. The pH of the

solution was checked every hour and KOH solution was added to keep the pH at ~7.5. All

subsequent steps were carried out at 4 °C for protein stability. To isolate the cell membranes

from the rest of the pulverized cell matter, the thawed cell lysate was centrifuged at 2000g for 5

min. The supernatant was carefully collected and was ultracentrifuged at 100,000g for 75 min

(Beckman, Ti 45 rotor). The pellet containing cell membranes was resuspended in lysis buffer (4

mL/g) and homogenized on ice with a Dounce tissue homogenizer. 40% of filter sterilized

glycerol was added to the membrane lysate and flash frozen in liquid nitrogen and stored in -

80°C for further use.

The homogenized membrane lysate was thawed in additional lysis buffer at 1:1 volume.

The sample was extracted in the detergent 1% DDM/CHS via stirring for 3 hr in a cold room (4

°C) and then centrifuged at 80,000 for 60 min. The supernatant was mixed with TALON cobalt resin pre-equilibrated with lysis buffer with 0.25% DDM/CHS. The mixture was allowed to rotate for 2 hr in 4 °C. The mixture was then loaded onto a column until only resin bound with protein remained. The column was washed with wash/elution buffer with 30mM imidazole (20x bed volume) and eluted with wash/elution buffer with 300mM imidazole (5x bed volume). The elution was concentrated to 0.5 mL with a Millipore Amicon Ultra 100K centrifugal filter unit and further purified on a Superose 6 Increase (10/300) size-exclusion column (SEC) pre-equilibrated with gel-filtration buffer. Gel-filtration fractions at ~10-11 mL identified to contain the tetrameric Kv1.2-2.1 complexed with the rβ2.1 were pooled and concentrated to ~4-5 mg/mL with a Millipore Amicon Ultra 100K filter unit. The concentrated sample was diluted with a buffer that had the composition of the gel-filtration buffer without the detergent or lipid and was reconcentrated to 4-5 mg/mL. The process was repeated until DDM/CHS concentration reached ~10mM while protein concentration was at 4.5 mg/mL. The sample was immediately loaded onto cryo-EM grids for freezing via vitreous ice formation. We will describe this process in more detail later below.

**Cryo-EM Sample Preparation**

Quantifoil Cu 200 and 300 R1.2/1.3 holey carbon grids (Quantifoil Micro Tools GmbH, Großlöbichau, Germany) were used for screening and data collection. The grids were plasma cleaned for 30 seconds in a Solarus Plasma Cleaner (Gatan) and were frozen in liquid ethane that was cooled with liquid nitrogen using the Vitrobot Mark IV (ThermoFisher) with the following parameters: ILT Kv1.2-2.1 sample volume of 3.5 µl, blot time of 3.5 sec, blot force of 3, temperature of 22°C, and humidity of 100%. Around 4-5 mg/mL concentration was optimal to see enough particles on micrographs without aggregation.

## Screening and Data Collection

Grids were screened on a 200 kV Talos side-entry microscope (FEI) equipped with the K2 summit direct detector (Gatan) using a Gatan 626 single-tilt holder at the University of Chicago. Replicate grids from the same preparation were shipped to Stanford-SLAC (Stanford Linear Accelerator Center) Cryo-EM Center ($S^2C^2$) for data collection. The grids were imaged on a Titan Krios microscope (FEI) at 300 kV, aligned for parallel illumination. Data collection images were acquired with a Gatan K3 Camera and a BioQuantum Energy Filter operated in super-resolution mode. Calibrated physical pixel size of 1.08 Å and a super-resolution pixel size of 0.54 Å with a defocus range between -1.5 and -2.5 µm were used to collect images with the Latitude S software (Gatan Inc., Pleasanton, CA). A dose of 1.25 $e^-/A^2$/frame per frame for 40 frames for a total of 50 $e^-/A^2$ was used. One image per hole was collected for all samples. Total exposure time was 4.0 sec, with frame duration of 0.1 sec/frame. 10,134 images were collected for the ILT Kv1.2-2.1 mutant sample. Of those, 7,884 images were properly motion-corrected for further processing.

## Data Processing

The images from the dataset were motion-corrected using MotionCor2, dose-weighted and CTF-estimated using CTFFIND4, and further processed using RELION 3 [31-35]. Selected 2D classes from WT Kv1.2-2.1 dataset (from high $K^+$ structure from Chapter 2) were used as template for RELION autopicking. Autopicking in RELION 3 using a threshold of 0.1 gave ~4.5M particles, which were subjected to 2D classification. Three rounds of 2D classification were performed to remove obvious artefacts before proceeding to the 3D construction of the density map. ~700k particles were selected from good 2D classes. 3D construction was made using the post-processed map from WT Kv1.2-2.1 in high $K^+$ as a reference. All ~700k particles were subjected to auto-refinement, yielding a 3.94 Å nominal resolution map in C4 symmetry.

Focused refinement on the entire Kv1.2-2.1 protein and subsequently only the transmembrane region gave a reconstruction with improved map quality, supporting confident building of the TM regions. Post-processing of the focused TM map was performed in RELION 3 using the 300 kV K3 detector star file and was calculated a masked nominal resolution of 3.68 Å in C4 symmetry by the 0.143 FSC criterion [36-38]. Local resolution was calculated by RELION's local-resolution, and particle orientation distribution calculated by RELION 3 [31, 35].

## Model Fitting

A tetrameric model for the Kv chimera was produced from an X-ray structure (PDB ID: 2r9r) and used for rigid body fitting in UCSF Chimera [39]. Because of the shift/rotation in the ILT density between the TM and cytosolic domains relative to the 2r9r structure, however, we first created two separate PDB files for TM and cytosolic domains. Then we fit each PDB file into the ILT density map before performing initial flexible fitting in COOT [40] by manually surveying the entire peptide chain of a single chain of the α and β subunit before applying the changes to other subunits. After a rough fit using COOT, we used cryo-fit2 [41] from Phenix [42] to fit the model into the density even better. Finally, we performed real space refinement using Phenix. Models were subjected to an all-atom structure validation using MolProbity (Table 1-1) [43].

## Model construction and molecular dynamics (MD) simulations

For model construction, we embedded a monomeric VSD (residues: 145-307) from the WT Kv1.2-2.1 chimaera channel (PDB ID: 2r9r) into a POPC membrane solvated with water and 100 mM KCl using VMD [44]. The ionization state of titratable residues was assigned to the default value of pH 7.0. The orientation and position of the VSD in the membrane was based on the prediction from the Orientations of Proteins in Membranes (OPM) database [45]. The final system

contained ~51,000 atoms and is electrically neutral. This WT VSD system was used to build the ILT mutant monomeric VSD system by replacing the coordinates of the WT VSD PDB with those of the ILT PDB file, while keeping the rest of the system unchanged. Two additional systems, WTtoILT and ILTtoWT, were generated *in silico* using VMD [44] via double-mutations I300L/S304T and L300I/T304S (I297 is unchanged as it is already an isoleucine in Kv1.2-2.1 WT) of the WT and ILT systems, respectively.

Molecular dynamics (MD) simulations were performed using Nanoscale Molecular Dynamics (NAMD) software [46]. After 5,000 steps of initial energy minimization, each of the four systems (WT VSD, ILT VSD, WTtoILT VSD, and ILTtoWT VSD) was equilibrated in the membrane for 50 ns with harmonic positional restraints on the backbone and side-chain heavy atoms being gradually decreased to 0.1 and 0 kcal/mol/$\text{Å}^2$, respectively. To study the water penetration dynamics through the VSD, the WT and ILT mutant systems were run for 50 ns without any restraints. These simulations were carried out under NPT ensemble. To study the displacement of charge across the VSD, each system was run for 20 ns at -200 mV, 0 mV, and +200 mV with the positional restraints of 0.1 kcal/mol/$\text{Å}^2$ applied to the backbone atoms. These simulations were carried out under NVT ensemble.

For all simulations, a timestep of 2 fs was used. The CHARMM36m force field was used for the protein [47], the CHARMM36 force field was used for lipids and ions [48], and the TIP3P model was used for water [49]. The temperature of 300K and pressure of 1 atm were maintained throughout the simulation using the Langevin dynamics and the Nose-Hoover Langevin piston method, respectively [50, 51]. Long-range electrostatic force was calculated using the particle mesh Ewald (PME) method with a grid density of 1/$\text{Å}^3$ [52]. The van der Waals interaction was calculated with a smoothing switch between 10 – 12 Å.

Two-dimensional water occupancy in the *X-Z* and *Y-Z* planes were calculated as the average number of water molecules within an interval of 2.0 Å in the box of -12 Å < x < 12 Å and -12 Å < y < 12 Å normalized to the maximum value of each case. The *Z* axis is chosen as the axis

through the VSD, where Z=0 corresponds to the location of the hydrophobic gasket F233. One-dimensional water number (mean and standard deviation) along the $Z$ direction was calculated by counting the number of water molecules in a slab of 2 Å and within a cylinder of radius 12 Å along the $Z$ axis. A total of 400 snapshots from the last 40 ns trajectory were used for the water penetration calculations.

The average displacement of charge, representing the coupling to the transmembrane potential, was calculated using the formula $\langle Q_d \rangle = \langle \sum_i q_i z_i / L_z \rangle$, where $q_i$ is the partial charge of the $i^{th}$ atom and $z_i$ is its z-coordinate. $L_z$ is the length of the system in the $z$-direction [28]. For each system, 2,000 snapshots from each of the 20 ns trajectory at three different electric fields (-200 mV, 0 mV, and +200 mV) were used to calculate the average displacement charges. The average displacement charges of two systems with the same construct but different conformations (WT VSD alone and ILTtoWT as one group and ILT coordinate VSD and WTtoILT as another group) were linearly fitted together. The resulting offset constant corresponds to the overall displacement in gating charge from WT to ILT.

**Figure preparation**

Structural figures were prepared with Chimera, [39] ChimeraX, [53, 54] and VMD [44].

# References:

1.  Ledwell, J.L. and R.W. Aldrich, *Mutations in the S4 region isolate the final voltage-dependent cooperative step in potassium channel activation.* J Gen Physiol, 1999. **113**(3): p. 389-414.
2.  Smart, O.S., et al., *HOLE: a program for the analysis of the pore dimensions of ion channel structural models.* J Mol Graph, 1996. **14**(6): p. 354-60, 376.
3.  Aggarwal, S.K. and R. MacKinnon, *Contribution of the S4 segment to gating charge in the Shaker K+ channel.* Neuron, 1996. **16**(6): p. 1169-77.
4.  Chanda, B., et al., *Gating charge displacement in voltage-gated ion channels involves limited transmembrane movement.* Nature, 2005. **436**(7052): p. 852-6.
5.  Seoh, S.A., et al., *Voltage-sensing residues in the S2 and S4 segments of the Shaker K+ channel.* Neuron, 1996. **16**(6): p. 1159-67.
6.  Starace, D.M., E. Stefani, and F. Bezanilla, *Voltage-dependent proton transport by the voltage sensor of the Shaker K+ channel.* Neuron, 1997. **19**(6): p. 1319-27.
7.  Armstrong, C.M. and F. Bezanilla, *Currents related to movement of the gating particles of the sodium channels.* Nature, 1973. **242**(5398): p. 459-61.
8.  Armstrong, C.M. and F. Bezanilla, *Charge movement associated with the opening and closing of the activation gates of the Na channels.* J Gen Physiol, 1974. **63**(5): p. 533-52.
9.  Keynes, R.D. and E. Rojas, *Characteristics of the sodium gating current in the squid giant axon.* J Physiol, 1973. **233**(1): p. 28P-30P.
10. Bezanilla, F., *The voltage sensor in voltage-dependent ion channels.* Physiol Rev, 2000. **80**(2): p. 555-92.
11. Ding, S. and R. Horn, *Tail end of the s6 segment: role in permeation in shaker potassium channels.* J Gen Physiol, 2002. **120**(1): p. 87-97.
12. Holmgren, M., K.S. Shin, and G. Yellen, *The activation gate of a voltage-gated K+ channel can be trapped in the open state by an intersubunit metal bridge.* Neuron, 1998. **21**(3): p. 617-21.
13. Jogini, V. and B. Roux, *Electrostatics of the intracellular vestibule of K+ channels.* J Mol Biol, 2005. **354**(2): p. 272-88.
14. Lu, Z., A.M. Klem, and Y. Ramu, *Coupling between voltage sensors and activation gate in voltage-gated K+ channels.* J Gen Physiol, 2002. **120**(5): p. 663-76.
15. Kalstrup, T. and R. Blunck, *S4-S5 linker movement during activation and inactivation in voltage-gated K(+) channels.* Proc Natl Acad Sci U S A, 2018. **115**(29): p. E6751-E6759.
16. Labro, A.J., A.L. Raes, and D.J. Snyders, *Coupling of voltage sensing to channel opening reflects intrasubunit interactions in kv channels.* J Gen Physiol, 2005. **125**(1): p. 71-80.
17. Pathak, M., et al., *The cooperative voltage sensor motion that gates a potassium channel.* J Gen Physiol, 2005. **125**(1): p. 57-69.
18. Jiang, Y., et al., *X-ray structure of a voltage-dependent K+ channel.* Nature, 2003. **423**(6935): p. 33-41.
19. Long, S.B., E.B. Campbell, and R. Mackinnon, *Crystal structure of a mammalian voltage-dependent Shaker family K+ channel.* Science, 2005. **309**(5736): p. 897-903.
20. Long, S.B., E.B. Campbell, and R. Mackinnon, *Voltage sensor of Kv1.2: structural basis of electromechanical coupling.* Science, 2005. **309**(5736): p. 903-8.
21. Long, S.B., et al., *Atomic structure of a voltage-dependent K+ channel in a lipid membrane-like environment.* Nature, 2007. **450**(7168): p. 376-82.
22. Tan, X.-F.B., Chanhyung, *Structure of the Shaker Kv channel and mechanism of slow C-type inactivation.* BioRxiv, 2021.
23. Smith-Maxwell, C.J., J.L. Ledwell, and R.W. Aldrich, *Uncharged S4 residues and cooperativity in voltage-dependent potassium channel activation.* J Gen Physiol, 1998. **111**(3): p. 421-39.
24. Gagnon, D.G. and F. Bezanilla, *A single charged voltage sensor is capable of gating the Shaker K+ channel.* J Gen Physiol, 2009. **133**(5): p. 467-83.
25. Schoppa, N.E. and F.J. Sigworth, *Activation of Shaker potassium channels. III. An activation gating model for wild-type and V2 mutant channels.* J Gen Physiol, 1998. **111**(2): p. 313-42.
26. Gagnon, D.G. and F. Bezanilla, *The contribution of individual subunits to the coupling of the voltage sensor to pore opening in Shaker K channels: effect of ILT mutations in heterotetramers.* J Gen Physiol, 2010. **136**(5): p. 555-68.

27. Stefani, E. and F. Bezanilla, *Cut-open oocyte voltage-clamp technique.* Methods Enzymol, 1998. **293**: p. 300-18.

28. Roux, B., *The Membrane Potential and its Representation by a Constant Electric Field in Computer Simulations.* Biophysical Journal, 2008. **95**(9): p. 4205-4216.

29. del Camino, D., M. Kanevsky, and G. Yellen, *Status of the intracellular gate in the activated-not-open state of shaker K+ channels.* J Gen Physiol, 2005. **126**(5): p. 419-28.

30. Carvalho-de-Souza, J.L. and F. Bezanilla, *Noncanonical mechanism of voltage sensor coupling to pore revealed by tandem dimers of Shaker.* Nat Commun, 2019. **10**(1): p. 3584.

31. Kimanius, D., et al., *Accelerated cryo-EM structure determination with parallelisation using GPUs in RELION-2.* Elife, 2016. **5**.

32. Rohou, A. and N. Grigorieff, *CTFFIND4: Fast and accurate defocus estimation from electron micrographs.* J Struct Biol, 2015. **192**(2): p. 216-21.

33. Scheres, S.H., *RELION: implementation of a Bayesian approach to cryo-EM structure determination.* J Struct Biol, 2012. **180**(3): p. 519-30.

34. Zheng, S.Q., et al., *MotionCor2: anisotropic correction of beam-induced motion for improved cryo-electron microscopy.* Nat Methods, 2017. **14**(4): p. 331-332.

35. Zivanov, J., et al., *New tools for automated high-resolution cryo-EM structure determination in RELION-3.* Elife, 2018. **7**.

36. Chen, S., et al., *High-resolution noise substitution to measure overfitting and validate resolution in 3D structure determination by single particle electron cryomicroscopy.* Ultramicroscopy, 2013. **135**: p. 24-35.

37. Rosenthal, P.B. and R. Henderson, *Optimal determination of particle orientation, absolute hand, and contrast loss in single-particle electron cryomicroscopy.* J Mol Biol, 2003. **333**(4): p. 721-45.

38. Scheres, S.H. and S. Chen, *Prevention of overfitting in cryo-EM structure determination.* Nat Methods, 2012. **9**(9): p. 853-4.

39. Pettersen, E.F., et al., *UCSF chimera - A visualization system for exploratory research and analysis.* Journal of Computational Chemistry, 2004. **25**(13): p. 1605-1612.

40. Emsley, P., et al., *Features and development of Coot.* Acta Crystallogr D Biol Crystallogr, 2010. **66**(Pt 4): p. 486-501.

41. Kim, D.N., et al., *Cryo_fit: Democratization of flexible fitting for cryo-EM.* J Struct Biol, 2019. **208**(1): p. 1-6.

42. Adams, P.D., et al., *PHENIX: a comprehensive Python-based system for macromolecular structure solution.* Acta Crystallographica Section D-Structural Biology, 2010. **66**: p. 213-221.

43. Chen, V.B., et al., *MolProbity: all-atom structure validation for macromolecular crystallography.* Acta Crystallogr D Biol Crystallogr, 2010. **66**(Pt 1): p. 12-21.

44. Humphrey, W., A. Dalke, and K. Schulten, *VMD: Visual molecular dynamics.* Journal of Molecular Graphics & Modelling, 1996. **14**(1): p. 33-38.

45. Lomize, M.A., et al., *OPM database and PPM web server: resources for positioning of proteins in membranes.* Nucleic Acids Res, 2012. **40**(Database issue): p. D370-6.

46. Phillips, J.C., et al., *Scalable molecular dynamics with NAMD.* J Comput Chem, 2005. **26**(16): p. 1781-802.

47. Huang, J., et al., *CHARMM36m: an improved force field for folded and intrinsically disordered proteins.* Nat Methods, 2017. **14**(1): p. 71-73.

48. Huang, J. and A.D. MacKerell, Jr., *CHARMM36 all-atom additive protein force field: validation based on comparison to NMR data.* J Comput Chem, 2013. **34**(25): p. 2135-45.

49. Jorgensen, W.L., et al., *Comparison of Simple Potential Functions for Simulating Liquid Water.* Journal of Chemical Physics, 1983. **79**(2): p. 926-935.

50. Feller, S.E., et al., *Constant-Pressure Molecular-Dynamics Simulation - the Langevin Piston Method.* Journal of Chemical Physics, 1995. **103**(11): p. 4613-4621.

51. Martyna, G.J., D.J. Tobias, and M.L. Klein, *Constant-Pressure Molecular-Dynamics Algorithms.* Journal of Chemical Physics, 1994. **101**(5): p. 4177-4189.

52. Essmann, U., et al., *A Smooth Particle Mesh Ewald Method.* Journal of Chemical Physics, 1995. **103**(19): p. 8577-8593.

53. Goddard, T.D., et al., *UCSF ChimeraX: Meeting modern challenges in visualization and analysis.* Protein Sci, 2018. **27**(1): p. 14-25.

54.    Pettersen, E.F., et al., *UCSF ChimeraX: Structure visualization for researchers, educators, and developers.* Protein Sci, 2021. **30**(1): p. 70-82.

# Chapter 4: Conclusion

This thesis was guided by two independent yet related questions. Firstly, what does C-type inactivation in eukaryotic voltage-gated potassium channels look like? Could the constricted conformation of the selectivity filter as seen from prokaryotic systems (KcsA) also explain the mechanism of C-type inactivation in the selectivity filter in voltage-gated channels? Secondly, how is the intracellular gate coupled to the VSD and what does it take to capture the intracellular gate in the closed state? While the first set of questions inquires about the mechanism of C-type inactivation at the selectivity filter and the second set about the coupling between the VSD movement and the closing and opening of the gate, they both seek to further explore the molecular mechanism underlying voltage-gating and conductance through $K^+$ channels. This thesis tries to answer these questions through functional and structural techniques using Kv1.2-2.1 as the model protein.

In chapter 2, we described the structure and function of Kv1.2-2.1 in low $K^+$ conditions using $NH_4^+$ and $Na^+$ as the replacement ion and compared it with the high $K^+$ conditions where we expected the channel to be conductive. This idea originated from KcsA, where low $K^+$ condition induced the C-type inactivated selectivity filter [1]. The functional studies displayed a drastic difference in Kv1.2-2.1 conduction between high $K^+$ and low $K^+$ conditions. Consistently, the cryo-EM maps of Kv1.2-2.1 also displayed a drastic difference in ion occupancy between the ionic conditions as well. However, there were very subtle changes in the structure of the selectivity filter across the three ionic conditions studied. This may be due to a relatively low resolution in the selectivity filter in our structures to capture the dominant conformation for the selectivity filter, or it could perhaps explain the subtle nature of the C-type inactivated state in eukaryotic voltage-gated potassium channels. Our MDFF simulations of each of the filter structures revealed some interesting differences between high and low $K^+$ conditions, specifically in the G374 residue, that were not readily observed in our models built from the

density maps. The HOLE analysis of the pore also revealed differences in the selectivity filter as well as the intracellular gate between high K$^+$ and low K$^+$ structures. All of these subtle yet clear differences may reveal the pathway towards fully C-type inactivated state in Kv1.2-2.1.

In chapter 3, we characterized the structure and function of the ILT mutant in Kv1.2-2.1. As was the case in *Shaker* channel [2], the ILT mutant significantly right shifts the G-V curve in Kv1.2-2.1 as well. This means that the intracellular gate is supposedly closed at 0 mV where our structural conformation is studied. However, contrary to our expectation, the ILT mutant had an opened intracellular gate. We did, however, observe some interesting differences in the VSD. Some crucial interactions between gating charges and countercharges were altered or disrupted between S2, S3, and S4 helices, which in turn affected the water permeation through the VSD and the amount of gating charge displacement in the VSD (albeit small). While we couldn't capture the closed state of the intracellular gate through the ILT mutant, we observed a glimpse of the intermediate state where the VSD decouples from the pore domain.

Overall, we highlight my efforts to answer the questions of gating and regulation of conductance in eukaryotic voltage-gated potassium channels. Contrary to recent C-type inactivated states presented in recent literature, we suggest more subtle changes in the selectivity filter that is responsible for regulating conduction. The asymmetric widening at the outer mouth (G374) and constriction at the center (G372) of the selectivity filter may be responsible for the C-type inactivated state in Kv1.2-2.1 chimera. Based on the wide C-type inactivation dynamics across various potassium channels, there may be different C-type inactivated states for each channel. Therefore, we are careful to expand our model to eukaryotic voltage-gated channels as a whole. We also report what we believe to be a stable intermediate state between the closed and the opened intracellular gate where the VSD undergoes a conformational change that affects the coupling with the intracellular gate.

As aside, although it was not explicitly mentioned in the thesis itself, I was also involved in other projects. Firstly, I participated in the structural characterization of E71V mutation of the

KcsA through X-ray crystallography, which became the impetus for the paper by Rohaim et al. [3]. In KcsA, E71 is critical for hydrogen bonding network with water molecules behind the selectivity filter that are in turn critical for stabilizing the C-type inactivated pinched selectivity filter [1, 4-7]. Mutating this glutamic acid to a valine, which is the residue in that position in eukaryotic voltage-gated potassium channels such as *Shaker* or Kv1.2, we hypothesized that we may be able to alter the crucial interactions made by E71 in KcsA and as a result capture a conformation of the filter that is representative of the C-type inactivated state in eukaryotic channels through this strategy. However, the initial resolution of the structure was too low to characterize the E71V conformational changes in KcsA while I was working on it for over two years. Once I focused my attention on Kv1.2-2.1 I had left this project, but it was also a large part of my graduate school career that was spent on the project.

Some other projects I participated during my Ph.D include: Folding and misfolding of potassium channel monomers during assembly and tetramerization [8]. Engineering of a synthetic antibody fragment for structural and functional studies of K$^+$ channels [9]. These works are already published with my participation noted in the paper.

## References:

1.    Zhou, Y., et al., *Chemistry of ion coordination and hydration revealed by a K+ channel-Fab complex at 2.0 A resolution.* Nature, 2001. **414**(6859): p. 43-8.
2.    Ledwell, J.L. and R.W. Aldrich, *Mutations in the S4 region isolate the final voltage-dependent cooperative step in potassium channel activation.* J Gen Physiol, 1999. **113**(3): p. 389-414.
3.    Rohaim, A., et al., *A distinct mechanism of C-type inactivation in the Kv-like KcsA mutant E71V.* Nat Commun, 2022. **13**(1): p. 1574.
4.    Chakrapani, S., et al., *On the structural basis of modal gating behavior in K(+) channels.* Nat Struct Mol Biol, 2011. **18**(1): p. 67-74.
5.    Cordero-Morales, J.F., et al., *A Multipoint Hydrogen-Bond Network Underlying KcsA C-Type Inactivation.* Biophysical Journal, 2011. **100**(10): p. 2387-2393.
6.    Cuello, L.G., et al., *Structural mechanism of C-type inactivation in K(+) channels.* Nature, 2010. **466**(7303): p. 203-8.
7.    Ostmeyer, J., et al., *Recovery from slow inactivation in K+ channels is controlled by water molecules.* Nature, 2013. **501**(7465): p. 121-4.
8.    Song, K.C., et al., *Folding and misfolding of potassium channel monomers during assembly and tetramerization.* Proc Natl Acad Sci U S A, 2021. **118**(34).
9.    Rohaim, A., et al., *Engineering of a synthetic antibody fragment for structural and functional studies of K+ channels.* J Gen Physiol, 2022. **154**(4).